Clemson University
TigerPrints

All Dissertations | Dissertations

May 2021

Diverse Mass Spectrometric Couplings and Applications of the Liquid Sampling–Atmospheric Pressure Glow Discharge as a Combined Atomic and Molecular Ionization Source

Tyler J. Williams
Clemson University, tw3@g.clemson.edu

Follow this and additional works at: https://tigerprints.clemson.edu/all_dissertations

Recommended Citation

Williams, Tyler J., "Diverse Mass Spectrometric Couplings and Applications of the Liquid Sampling–Atmospheric Pressure Glow Discharge as a Combined Atomic and Molecular Ionization Source" (2021). *All Dissertations*. 2792.
https://tigerprints.clemson.edu/all_dissertations/2792

This Dissertation is brought to you for free and open access by the Dissertations at TigerPrints. It has been accepted for inclusion in All Dissertations by an authorized administrator of TigerPrints. For more information, please contact kokeefe@clemson.edu.

DIVERSE MASS SPECTROMETRIC COUPLINGS AND APPLICATIONS OF THE LIQUID SAMPLING - ATMOSPHERIC PRESSURE GLOW DISCHARGE AS A COMBINED ATOMIC AND MOLECULAR IONIZATION SOURCE

A Dissertation
Presented to
the Graduate School of
Clemson University

In Partial Fulfillment
of the Requirements for the Degree
Doctor of Philosophy
Chemistry

---

by
Tyler Joseph Williams
May 2021

Accepted by:
R. Kenneth Marcus, Committee Chair
George Chumanov
Carlos Garcia
Brian Powell

ABSTRACT

Mass spectrometry has remained an important tool for chemical analysis, acting as perhaps the most information dense technique in the scientists' toolkit. Mass spectrometry however is divided into atomic and molecular subdisciplines due to specific and distinct challenges associated with ionizing each sample type. Furthermore, molecular mass spectrometry has seen rapid developments in miniaturization leading to reduced format platforms with lower operational overhead and improved ease of use. To be clear, there are no mass spectrometry systems capable of analyzing both atomic and molecular samples, and little effort has been put forth towards developing miniaturized atomic mass spectrometry instrumentation. A bourgeoning solution to this lack of instrumentation is in the development of the liquid sampling – atmospheric pressure glow discharge (LS-APGD).

The LS-APGD was initially developed for solution-based trace metal analysis and paired with optical detection systems, but has since been interfaced with a variety of mass spectrometers. Operating at atmospheric pressure, the LS-APGD has the ability to couple with any mass spectrometer having an atmospheric pressure interface, which is common for molecular mass spectrometers. As a result, the aforementioned advancements in molecular mass spectrometry are opened to atomic analysis. Furthermore, the LS-APGD demonstrated the ability to operate as a combined atomic and molecular (CAM) ionization source, the first of its kind. The LS-APGD operates using < 100 µL min^{-1} liquid flow and < 1 L min^{-1} He sheath gas, allowing for reduced operational overhead relative to many other ionization sources. Even with these unique merits behind it, there are still a variety

of instrument platforms and sampling methodologies that require further development with the LS-APGD. Presented in this dissertation are efforts in coupling the LS-APGD with a diverse array of mass spectrometers, including triple quadrupole and a compact mass spectrometers, to perform CAM analyses. On these platforms, optimization is performed and analytical figures of merit are established, in addition to demonstrations of the instrument pairing capabilities. On Orbitrap mass spectrometers, the LS-APGD is used to demonstrate sampling capabilities on low polarity compounds typically exclusive to ionization sources such as atmospheric pressure photoionization (APPI). Previous efforts in U isotope ratio analysis are also investigated in an effort to further understand the effects of instrument operation on measurement variation and sources of bias.

DEDICATION

This dissertation is dedicated to my family and friends who have believed in me and supported me through the years. In particular, to my parents, Ken and Lisa, for being the best parents I could ask for, always loving and supporting me and helping me become the person I am today. To my sister Jessica, for always supporting and challenging me. To the rest of my family, aunts, uncles, grandparents, cousins, etc., for being the best family I could ever ask for.

This dissertation is also dedicated to my partner Paige, for supporting and believing in me, even when I didn't believe in myself. To all of my friends from grade school through college, you've help me grow through the years and enjoy life. And to the friends I've made at Clemson, your support and friendship through the years has made life here that much better.

ACKNOWLEDGMENTS

I first would like the thank Dr. Marcus for his support and guidance throughout my career at Clemson University. You have continually challenged and pushed me to become a better scientist and 'tinkerer.' I am also endlessly grateful for the opportunities you have given to me to participate in research collaborations all over, as well as the many conferences I've been able to attend. I cannot thank you enough for your mentorship over the years.

I would also like to thank Dr. Jackson, my undergraduate research advisor, who first introduced me to research. The experiences I had in the group, both in the lab and at conferences, cemented my decision to go to graduate school and created a lifelong interest in mass spectrometry.

I want to thank all of the members of the Marcus group I have worked with over the years. You all have made the lab such a fun place to work and supported and challenged me to be a better person and scientist. I couldn't ask for a better group of people to have worked with. In particular, I want to say a special thanks to Dr. Edward Hoegg, my in-group mentor, for dealing me when I first joined the group, and continually being a mentor and friend through the years.

Lastly, I would like to thank my graduate committee Dr. George Chumanov, Dr. Brian Powell, and Dr. Carlos Garcia.

TABLE OF CONTENTS

Page

Table of Contents (Continued) Page

Table of Contents (Continued) Page

LIST OF TABLES

LIST OF FIGURES

List of Figures (Continued)

Figure Page

List of Figures (Continued)

Figure Page

List of Figures (Continued)

Figure Page

List of Figures (Continued)

Figure Page

CHAPTER I

INTRODUCTION

1.1 Introduction to Mass Spectrometry

As the scientific community continues to explore natural and manmade materials and compounds, chemical analysis remains an incredibly vital component. For more than 100 years, mass spectrometry in particular has offered arguably the most information dense platform in the scientists' toolkit. This analytical technique can provide information including elemental composition/structural details, quantitative determinations, reaction physics and kinetics, and isotopic measurements, to name a few. This information is obtained by introducing samples into an ionization source, which vaporizes and ionizes the sample, and measures the mass-to-charge ratio under vacuum conditions. As a result, mass spectrometry has found applications across diverse fields including environmental science, nuclear science, physics, geology, chemistry, and more.[1-3]

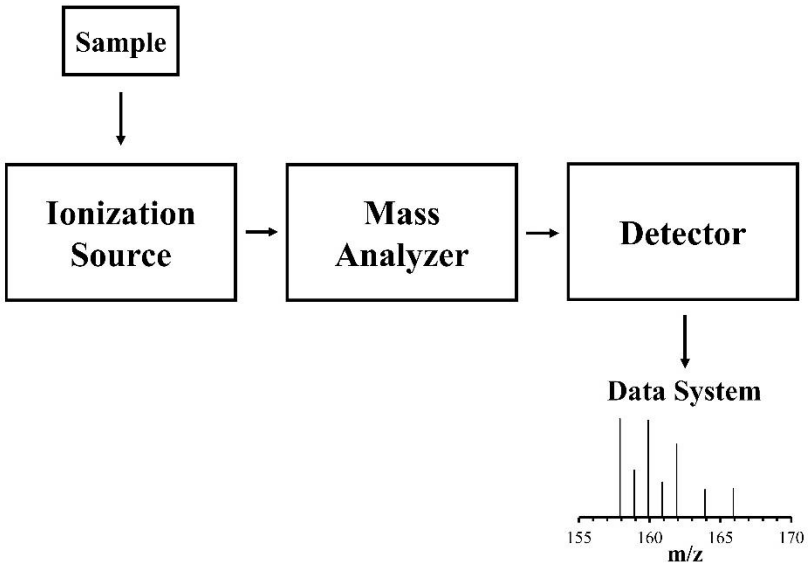

Figure 1.1: A basic box diagram of a mass spectrometer highlighting the major components of the system

A simplistic view of a mass spectrometer is given in Figure 1.1, where the major modules include the ionization source, mass analyzer, and detector. Analytes are converted to gas-phase ions in the ionization sources and are then separated based on mass-to-charge ratio in the mass analyzer, before finally being detected. Dependent on the application at hand, the specific components used in each of these modules may vary. In particular, most mass analyzers are applicable to, or of interest in some manner to all fields. The selection of the proper mass analyzer depends on characteristics such as the mass range, scan rate, resolving power, sensitivity, etc. For example, the analysis of single nanoparticles for elemental analysis and particle number concentration requires the use of extremely high scan speeds (<2 ms).[4, 5] As such, quadrupole/triple quadrupole,[6, 7] time-of-flight (TOF)[8], or sector field[9] mass analyzers offer the scan speeds required to observe individual particles and would be employed. Other analyzers, such as the Fourier transform – ion cyclotron

resonance (FT-ICR)[10] or the Orbitrap[11], have far slower scan speeds but can achieve resolutions (defined as $m/\Delta m$) $\geq$ 1,000,000 enabling further analysis of structural complexities and separating isobaric interferences. As such, these systems are common in the fields of proteomics and metabolomics, where the high resolution is a necessity due to the complex nature of samples.

While the mass analyzer selection is important for analysis, perhaps the most important component is the ionization source. The composition of the sample to be analyzed greatly influences the selection of an ionization source where physical state, sample matrix, or concentration, to name a few, must be considered. The choice of the ionization source can also affect the subsequent mass spectrum, where some source can lead to increased degrees of fragmentation, potentially giving structural information, while those with less fragmentation preserve the determination of the molecular composition. One of the greatest distinctions between ionization sources is the ability to perform atomic ionization or molecular ionization. Simply, the ionization sources used in atomic ionization input excess heat or energy leading to high degrees of dissociation from molecular samples, while those used in molecular ionization lack the energy to ionize elemental samples. As a result, mass spectrometry is largely split into two categories with their own collection of instrument components.[1]

1.1.1 Atomic Mass Spectrometry

The field of atomic mass spectrometry focuses largely on identification, quantification, speciation, and isotopic analysis of elemental samples, typically at trace levels (<1 $\mu g\ mL^{-1}$).[12, 13] Atomic mass spectrometry is largely dominated by two

techniques, inductively coupled plasma – mass spectrometer (ICP-MS)[14] and thermal ionization mass spectrometer (TIMS).[15, 16] TIMS instrumentation is among the earliest mass spectrometers developed, though ICP-MS instruments in recent years have become attractive as a result of coupling with liquid chromatography (LC) systems for speciation or laser ablation systems for solids sampling as well as high throughput capabilities.[17] As ubiquitous to atomic mass spectrometry as these techniques have become, there are not without their own issues.

Introduced in the mid-1900's, TIMS is an important tool in the measurement of isotopic abundances and has come to be considered the gold standard in this area.[15, 16, 18] TIMS operates by depositing samples onto a metallic filament which is loaded into the instruments' ion source housing. The housing and the rest of the mass spectrometer system are then brought under high vacuum conditions for analysis. At this stage, the metallic filament is heated to a sufficient temperature (up to 2500 °C) to ionize the sample, which is dependent upon its ionization potential.[19, 20] In modern TIMS instruments, the ions are then transported and focused through ion optics into the mass analyzer, which is most commonly a magnetic sector. A multi-collector detection system is then utilized to simultaneously measure multiple isotopes.[21] Because the entirety of TIMS analysis takes place under high vacuum, the stability of the measurement environment allows for high precision isotopic abundances to be measured. This capability has led to applications in fields such as geochronology[16] and nuclear sciences[15, 18], where high precision isotope ratio (IR) measurements are a necessity. Although TIMS is well established in the IR community, the technique is not without its drawbacks. In terms of sample introduction,

TIMS requires samples to be chemically pure, typically requiring complex sample preparation, and achieves ionization efficiencies of <1% in most cases.[1, 2] From the instrumentation standpoint, these instruments are large and complex, and the need for the entire system to be under high vacuum conditions requires lengthy timeframes between sample preparation and analysis. These drawbacks do present limitations for the applications of TIMS, and more recent developments in atomic mass spectrometry have begun to challenge its pertinence.

A more recent technique to atomic mass spectrometry is ICP-MS, which has been established as the workhorse instrument of the field.[5, 14] Unlike TIMS, an ICP operates at atmospheric pressure, negating the need to evacuate the ion source to high vacuum conditions. The ICP typically utilizes Ar gas to generate a plasma containing ions and electrons at extremely high temperatures, which can atomize and ionize introduced aqueous samples. The ICP is generated inside a quartz torch through which both the Ar gas and aqueous sample are introduced. Surrounding the end of the torch is a copper load coil connected to an RF generator creating oscillating electromagnetic fields. An ignition source is used to ionize some of the Ar gas, which is then accelerated in the electromagnetic field from the load coil. These ions, often referred to as seed ions undergo collisional processes with more Ar gas, creating a cascade of ionization reactions and thus generating a plasma.[14] Aqueous samples are first passed through a nebulizer which acts to aerosolize the sample and may be of a variety of designs, which may provide enhancements to some types of analyses. From the nebulizer, the sample is introduced into the center of the ICP to undergo ionization. ICP-MS instruments were first introduced in the 1980's and gained

rapid acceptance due to their unparalleled sensitivity, robustness, and ease of performing multi-element analysis, which, in particular, is a significant advantage over TIMS. These systems commonly employ quadrupole or magnetic sector mass analyzers for elemental or isotopic analyses.[7, 14, 22, 23] ICP - magnetic sector instruments have, in fact, begun to rival TIMS instruments in terms of isotope ratio precision with easier sample prep and more rapid analysis times.[15, 24, 25] One of the more prevalent issues with ICP however is the occurrence of isobaric interferences stemming from Ar related species, other elements, matrix constituents, etc. Efforts to overcome interferents have led to the introduction of powerful techniques, including collision-reaction cells and cool plasma conditions.[26-30] Of course, these additions further increase the user knowledge required for operation. Furthermore, instrument costs, both upfront and upkeep, can be astronomical as ICP requires Ar flow rates of 15-20 L min^{-1} and sample introduction rates of ~0.4 mL min^{-1}, leading to large sample volume requirements.[14] As powerful of a technique as it is, these limitations can confine the scenarios in which ICP-MS instruments can be implemented to well-equipped and well-funded laboratories.

1.1.2 Molecular Mass Spectrometry

Although the first applications of molecular mass spectrometry came later than those in atomic mass spectrometry, the development of technologies in this area has been far more rapid as a result of the sample complexity, both in terms of analyte and matrix. Samples analyzed in molecular mass spectrometry may range from small (<1 kDa) molecules that vary from non-polar to polar, to large polymers or biomolecules (>10 kDa).[1-3] The sample types vary as well, as samples exist as solids, liquids, or gases. As a

result, there are many ionization sources and techniques commercially available in addition to those being continually developed in research environments. One of the more notable aspects of these molecular sources is their operation at atmospheric pressure, similar to the ICP source, which improves ease of use and analysis times. Different from atomic mass spectrometry, the mass analyzers employed in molecular mass spectrometry are less correlated with ionization sources and are far more dependent on the analysis requirements. Quadrupole, triple quadrupole, and quadrupole ion traps are among the more common sources, owing to less demanding vacuum requirements. These can allow for tandem MS to be employed for the structural characterization required in many applications, however, these systems typically have relatively low resolution. FT-ICR instruments were the most common high-resolution instruments until the recent introduction of Orbitrap mass spectrometers, which have brought resolving powers of > 1 million to benchtop platforms, as well as the high mass accuracy required for complex samples.[10, 11, 31] While there are many molecular ionization sources, the most prevalent sources used on all of these systems are atmospheric pressure chemical ionization (APCI) and electrospray ionization (ESI), which are considered to be 'soft-ionization' sources, generating ions as $[M+H]^+$ or $[M-H]^-$ with little to no fragmentation.[1-3]

First introduced in the 1970's, APCI has evolved to be one of the most common molecular ionization sources, with the capability to analyze polar and low polarity compounds having masses below 1500 Da. In APCI, the liquid sample is introduced through a fused-silica capillary which is recessed within a nebulizer probe through which a N_2 sheath gas is introduced coaxially. The probe is typically heated, and the liquid sample

being introduced to the heat and flowing sheath gas is aerosolized and vaporized.[1, 2] The gaseous stream of N_2, solvent, and analyte molecules then interact with a corona discharge electrode, typically operated at a few μA, to undergo ionization. Typically, the corona discharge forms ions from the N_2 gas stream or atmospheric species, such as O_2 or H_2O, by corona induced electron ionization. Interactions between these ions and solvent molecules form secondary ions which finally interact with analyte molecules to ionize them via proton transfer. Operating at atmospheric pressure, the mean free path of ions is low, and the number of ion-molecule interactions is high, resulting in high ionization efficiency. Between its high ionization efficiency and tolerance of liquid flow rates of up to 2 mL min^{-1}, APCI is often interfaced with LC systems.[32-34] APCI however, requires that the analyte be both thermally stable and volatile due to the heated vaporization step and gas phase ionization process.[35] This limits the breadth of analytes that may be sampled, in particular leaving out high molecular weight analytes such as biomolecules, which have become commonplace in molecular mass spectrometry.[36, 37]

As strong of a technique as APCI is, ESI has become, perhaps, the most successful ionization source in molecular mass spectrometry. The success of ESI came as a result of its ability to produce ions where APCI fails, nonvolatile and thermally labile compounds. [32-35, 38, 39] Sample is introduced to the ESI via a stainless-steel capillary which is held at a potential between 2-5 kV relative to a counter electrode. The introduced sample, which must be electrically conductive, is influenced by the applied potential forming a Taylor cone from which fine droplets are produced. Assisted by a drying/sheath gas which may be heated, these droplets undergo continuous desolvation which increases the charge

density until the Rayleigh limit is reached and a "Coulomb explosion" occurs, further reducing droplet size and eventually leaving just ions.[38, 39] This process, when applied to large molecules which are typically nonvolatile, essentially aerosolizes the molecules and the process of electrospray acts to remove any solvent from the molecule. Because the droplets in electrospray are highly charged, these large molecules can carry multiple charges as long as multiple ionization sites are available, leading to m/z values far lower than the nominal mass of the compound. The most notable application of this is for the analysis of biomolecules such as proteins, enabling the intact measurement and identification on mass spectrometers whose mass range would typically be ill-suited for high mass applications.[38] Like the other sources described, ESI has a number of challenges that may limit its applicability, the most common of which is intolerance towards high salt samples. ESI sources can typically only tolerate salt concentrations of <10 mM, which proves challenging for the many biological applications which require its use.[2, 40] Furthermore, electrochemical processes can occur as a result of the electrospray process, stemming from changes in concentration, solvent, etc., which may limit sensitivity.[41, 42] As a result, careful considerations must be made for sample preparation and analysis to ensure a successful measurement may be carried out.

1.2 Miniaturization in Mass Spectrometry

The capabilities of mass spectrometry as well as the diversity of analyses has made it a target in the push to miniaturize analytical instrumentation. Miniaturization efforts typically focus on the reduction of instrument footprint, sample volumes, and operational overhead.[43-45] Although advancements in computing technologies have vastly reduced the

mass spectrometer footprint and ease of use, many of these instruments remain limited to within the analytical laboratory due to their large footprint and high consumable use. In particular, the necessity to obtain high vacuum in the mass analyzer region requires multi-stage pumping, adding considerable size. Additionally, as the capabilities of these instruments have increased towards ultra-high resolutions and tandem MS, vacuum requirements have increased. As a result, a sizeable contribution towards efforts in miniaturizing mass spectrometers has been in applying simple mass analyzers of small format in a low volume vacuum chamber which can be maintained with minimal pumping. In fact, many of the mass analyzers common to molecular mass spectrometry, such as quadrupoles or quadrupole ion traps, already require less stringent vacuum conditions. Newer mass analyzers have brought advancements here as well, including the rectilinear ion trap which has been employed in a few different miniaturized systems. Through the development of these miniaturized systems, it is acknowledged that by compromising on the analyzer components and the vacuum systems the performance relative to laboratory scale instruments will be minimized. Miniaturized mass spectrometers should retain *adequate* performance which is often defined as unit mass resolution and be sensitive enough for the intended application. Although compromises to the mass analyzers are often made, there is room for tuning the system towards a specific application by focusing on the ionization source.[46, 47]

Many miniaturized MS systems operate using external atmospheric pressure ionization sources and as such, continue to utilize primarily ESI sources. Of course, other aspects of miniaturization, reducing sample volumes and operational overhead, can be

achieved with alternative ionization sources. Developments in this area have led to a variety of ionization sources which may reduce consumable usage/sample volumes as well as simplify sample introduction for work outside the laboratory. An interesting modification of ESI is desorption ESI (DESI), which acts to desorb a sample off of a surface using the spray from ESI for rapid sample introduction. This source, however, still has the same gas flow and solvent requirements which may be ill suited towards the small vacuum systems of miniaturized systems.[48] A more common ionization technique employed in miniaturized systems is paper spray ionization, which requires minimal sample volumes and no gas flow. In this source, the sample and solvent are placed onto a piece of paper that has been cut to a point, and a high voltage is applied relative to the MS inlet. The generated electric field causes charge to accumulate at the tip of the paper where droplets are ejected. Similar to ESI, the droplets undergo desolvation and "Coulomb explosions" to generate ions. While simplistic in operation, a new paper triangle must be used for each sample to be analyzed.[49]

What might become clear at this point, is that the majority of these advancements in miniaturized mass spectrometers are only applicable to molecular applications. There has been far less effort made to miniaturize atomic mass spectrometry instrumentation, in large part due to the more complicated nature of the ionization sources and ionization itself. Sources such as the ICP use large volumes of Ar gas to maintain a plasma leading to stringent differential pumping requirements unsuitable to miniaturized platforms. In terms of ionization, these molecular ionization sources lack the energy to efficiently ionize elemental samples. As such, an ionization source which can perform elemental analysis on

a reduced format platform would need to maintain high energies at smaller footprints and with lower consumable usage.

1.3 Atmospheric Pressure Glow Discharges

The field of atomic mass spectrometry has recently seen the development of atmospheric pressure glow discharge (APGD) devices as a new ionization source for elemental analysis. APGD devices are adapted from GD ionization sources, which have a legacy in the sampling of solid materials for elemental analysis by both optical emission spectroscopy and mass spectrometry. In general, APGD devices are attractive due to their small format, simplicity, and reduced consumable use relative to traditional atomic ionization sources. This class of devices was first introduced by Cserfalvi *et al.* as the electrolyte cathode glow discharge (ELCAD)[50] and further adapted by Hieftje *et al.* into the solution cathode glow discharge (SCGD).[51] These devices employed a grounded tungsten or titanium anode and an overflowing electrolytic solution (cathode) between which a plasma is generated. These devices are effective tools for trace metal analysis, however similarly to an ICP, high sample flow rates necessitate large sample volumes and subsequent waste collection.

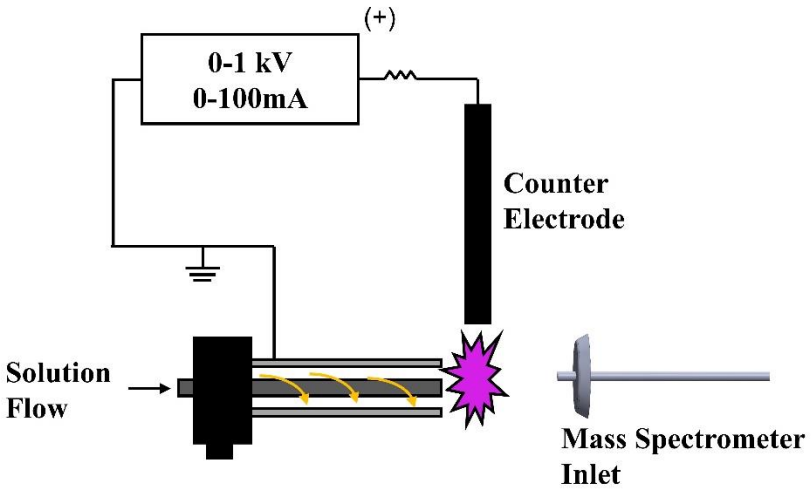

Figure 1.2: Diagrammatic representation of the liquid sampling – atmospheric pressure ionization source

Developed by Marcus and Davis, the liquid sampling – atmospheric pressure glow discharge (LS-APGD) was introduced as an atomic spectroscopy source as an alternative APGD device and is depicted in Fig. 1.2.[52] Principally, the LS-APGD operates using liquid flow rates of <100 µL min^{-1}, He sheath gas flow rates of <1 L min^{-1} and a power consumption of <50 W, while maintaining a high power density (~10 W mm^{-3}).[53] Like the ELCAD and SCGD, the LS-APGD was initially developed as an excitation source for optical emission spectroscopy.[52, 54-56] Initial demonstrations of the LS-APGD for mass spectrometry were performed by Quarles *et al.*, representing the first use of an APGD source for mass spectrometry.[57, 58] An important characteristic of this pairing was the ability of this source to couple with any mass spectrometer having an atmospheric pressure interface. As such, the advancements in molecular mass spectrometry, namely ultra-high resolution and miniaturized instrumentation, became available for elemental analysis. Further studies looked to optimize the analytical performance of the LS-APGD on a ThermoFisher LCQ Advantage Max based on multi-element response. This works looked

at source parameters and sampling conditions to maximize the analyte responses, eventually obtaining detection limits in the ppb range which is far higher than those achieved by traditional atomic mass spectrometry techniques, however, the sample volume used resulted in only ng levels of material used.[59] More recently, the LS-APGD has found perhaps its most promising application, in the high precision and high accuracy measurement of isotope ratios. Preliminary work by Hoegg *et al.* utilized the high-resolution instrumentation available to molecular mass spectrometry by interfacing the LS-APGD with an Orbitrap mass spectrometer.[60] Ion source operating parameters and instrument operation were investigated to obtain high fidelity isotope ratio measurements, ultimately demonstrating %RSD values of typically <1% for various elemental samples. This work and those that followed adopted a particular focus on the measurement of U isotope ratio for application in nuclear forensics. Additional work from Hoegg *et al.* explored the effects of concomitant ions on isotope ratio measurements and investigated the sensitivity of this coupling, further improving measurement precision and obtaining 30 pg mL^{-1} detection limits for U.[61-63] A culmination of this work is shown in a collaboration with Los Alamos National Laboratory where the LS-APGD/Orbitrap coupling was benchmarked against traditional IR techniques including ICP-MS and TIMS. Ultimately, the precision values (0.076%) and detection limits achieved in this coupling begin to rival traditional ICP-MS instrumentation.[64]

A particularly unique aspect of the LS-APGD is its ability to operate as a combined atomic and molecular (CAM) ionization source. In this aspect, the LS-APGD became, to our knowledge, the first ionization source capable of doing so. Work by Zhang *et al.* first

described this phenomenon looking at the speciation of uranyl complexes and further developed the application observing a variety of polar molecular drug targets.[65, 66] This change in ionization is seen by changing the solvent composition from 2% HNO_3 to a MeOH:H_2O mixture. Furthermore, studies demonstrating the ability to analyze molecular samples through ambient desorption of a solid sample introduce capabilities desired within the field of miniaturization.[67] Recently, the LS-APGD has demonstrated the ability to simultaneously ionize atomic and molecular species, connected to a laser ablation system, for comprehensive imaging.[68] It may seem apparent that this source could ionize molecular species in a similar manner to APCI, where ion-molecule interactions caused interactions within the plasma lead to ionizing analyte species. However, work by Zhang *et al.* has demonstrated the ability to ionize biomolecules such as proteins, by the addition of multiple protons in a similar manner to ESI.[66] This capability adds considerable applicability to the LS-APGD where it is not only applicable to elemental and small molecular samples, but can extend into the range of ESI, providing exceptional analytical diversity.

1.4 Summary of Chapters

At the time this research began, the LS-APGD had been interfaced with only the quadrupole ion trap and Orbitrap instruments. The capabilities in analyzing atomic species on platforms built with the advantages seen in molecular mass spectrometry instrumentation had yet to be exploited. Chapter II focuses on the interfacing of the LS-APGD with a commercial triple quadrupole mass spectrometer designed for molecular mass spectrometry. Here, source and instrument parameters were optimized for analytical performance, though limitations of the coupling designate its use primarily for qualitative

investigations. Chapter III investigates a new configuration of the LS-APGD termed the single-electrode LS-APGD. This configuration is optimized and compared to the traditional configuration, and a brief investigation into operating differences and their significances is discussed. Chapter IV sees the LS-APGD interfaced with a mass spectrometer of a reduced format platform, taking advantage of the miniaturization efforts seen in molecular mass spectrometry. Here, the LS-APGD and the instrument ion optics system are optimized and capabilities in CAM mass spectrometry are demonstrated. Chapter V demonstrates the ability of the LS-APGD to ionize non-polar polyaromatic hydrocarbons which are typically reserved for analysis by APCI or atmospheric pressure photoionization (APPI). Chapter VI investigates the Orbitrap platform's collisional dissociation methods and ion transmission characteristics in an effort to elucidate sources of variation and error in IR measurements, ultimately demonstrating increased performance.

1.5 List of Publications

The work presented in this dissertation is based on the work published in the following journal articles:

Chapter II – "Coupling of the liquid sampling – atmospheric pressure glow discharge (LS-APGD) ionization source with a commercial triple-quadrupole mass spectrometer," Tyler J. Williams and R. Kenneth Marcus, J. Anal. At. Spectrom., 2019, 34, 1468-1477.

Chapter III – "Development of an integrated, single electrode liquid sampling – atmospheric pressure glow discharge microplasma ionization source," Tyler J. Williams and R. Kenneth Marcus, Spectrochim. Acta Part B, 2020, 105994.

Chapter IV – "Coupling the liquid sampling – atmospheric pressure glow discharge, a combined atomic and molecular (CAM) ionization source, to a reduced-format mass spectrometer for the analysis of diverse species," Tyler J. Williams and R. Kenneth Marcus, J. Anal. At. Spectrom., 2020, 35, 1921-1921.

Chapter V – "Mass spectrometric characteristics and preliminary figures of merit for polyaromatic hydrocarbons via the liquid sampling – atmospheric pressure glow discharge microplasma," Tyler J. Williams, Jacob R. Bills, and R. Kenneth Marcus, J. Anal. At. Spectrom., 2020, 35, 2475-2478.

Chapter VI – "Roles of collisional dissociation modalities on spectral composition and isotope ratio measurement performance of the liquid sampling – atmospheric pressure glow discharge / orbitrap mass spectrometer coupling," Tyler J. Williams, Edward D. Hoegg, Jacob R. Bills, and R. Kenneth Marcus, Int. J. Mass. Spectrom., 2021, Accepted.

1.6 References

1. C. Dass, *Fundamentals of Contemporary Mass Spectrometry*, John Wiley & Sons, Inc., Hoboken, NJ, 2007.
2. E. d. Hoffman and V. Stroobant, *Mass Spectrometry: Principles and Applications*, John Wiley & Sons, Ltd, West Sussex, England, Third edn., 2007.
3. J. T. Watson and O. D. Sparkman, *Introduction to Mass Spectrometry: Instrumentation, Applications, and Strategies for Data Interpretation*, John Wiley & Sons, Ltd, West Sussex, England, Fourth edn., 2007.
4. A. Hineman and C. Stephan, *J. Anal. At. Spectrom*, 2014, **29**, 1252-1257.
5. B. Meermann and V. Nischwitz, *J. Anal. At. Spectrom*, 2018, **33**, 1432-1468.
6. R. Peters, Z. Herrera-Rivera, A. Undas, M. van der Lee, H. Marvin, H. Bouwmeester and S. Weigel, *J. Anal. At. Spectrom*, 2015, **30**, 1274-1285.
7. S. Candás-Zapico, D. J. Kutscher, M. Montes-Bayón and J. Bettmer, *Talanta*, 2018, **180**, 309-315.
8. L. Hendriks, A. Gundlach-Graham, B. Hattendorf and D. Günther, *J. Anal. At. Spectrom*, 2017, **32**, 548-561.
9. T. Prohaska, J. Irrgeher, A. Zitek and N. Jakubowski, *Sector Field Mass Spectrometry for Elemental and Isotopic Analysis*, The Royal Society of Chemistry, 2014.
10. D. F. Smith, D. C. Podgorski, R. P. Rodgers, G. T. Blakney and C. L. Hendrickson, *Anal. Chem.*, 2018, **90**, 2041-2047.
11. E. Denisov, E. Damoc, O. Lange and A. Makarov, *Int. J. Mass Spectrom.*, 2012, **325-327**, 80-85.
12. N. H. Bings, A. Bogaerts and J. A. C. Broekaert, *Anal. Chem.*, 2013, **85**, 670-704.
13. D. W. Koppenaal, *Anal. Chem.*, 1992, **64**, 320-342.
14. R. Thomas, *Practical Guide to ICP-MS: A Tutorial for Beginners*, CRC Press, Boca Raton, FL, Third edn., 2013.
15. S. K. Aggarwal, *Anal. Methods*, 2016, **8**, 942-957.
16. C. Pomiès, A. Cocherie, C. Guerrot, E. Marcoux and J. Lancelot, *Chem. Geol.*, 1998, **144**, 137-149.
17. D. P. Bishop, D. J. Hare, D. Clases and P. A. Doble, *TrAC, Trends Anal. Chem.*, 2018, **104**, 11-21.
18. X. Hou, W. Chen, Y. He and B. T. Jones, *Appl. Spectrosc. Rev.*, 2005, **40**, 245-267.
19. M. G. Inghram and W. A. Chupka, *Rev. Sci. Instrum.*, 1953, **24**, 518-520.
20. A. L. Yergey, B. L. Bentz and P. Jane Gale, in *The Encyclopedia of Mass Spectrometry*, eds. M. L. Gross and R. M. Caprioli, Elsevier, Boston, 2016.
21. L. Ball, K. W. W. Sims and J. Schwieters, *J. Anal. At. Spectrom*, 2008, **23**, 173-180.
22. D. Pröfrock and A. Prange, *Appl. Spectrosc.*, 2012, **66**, 843-868.
23. H. E. Taylor, *Inductively Coupled Plasma-Mass Spectrometry: Practices and Techniques*, Academic Press, San Diego, CA, 2001.
24. L. Yang, *Mass Spectrom. Rev.*, 2009, **28**, 990-1011.

25. A. D. Pollington, W. S. Kinman, S. K. Hanson and R. E. Steiner, *J. Radioanal. Nucl. Chem.*, 2016, **307**, 2109-2115.
26. S. Diez-Fernández, H. Isnard, A. Nonell, C. Bresson and F. Chartier, *J. Anal. At. Spectrom*, 2020, **35**, 2793-2819.
27. S. D. Tanner, V. I. Baranov and D. R. Bandura, *Spectrochim. Acta, Part B*, 2002, **57**, 1361-1452.
28. T.-S. Lum and K. Sze-Yin Leung, *J. Anal. At. Spectrom*, 2016, **31**, 1078-1088.
29. E. Bolea-Fernandez, L. Balcaen, M. Resano and F. Vanhaecke, *J. Anal. At. Spectrom*, 2017, **32**, 1660-1679.
30. D. Wollenweber, S. Straßburg and G. Wünsch, *Fresenius' J. Anal. Chem.*, 1999, **364**, 433-437.
31. S. Eliuk and A. Makarov, *Annu. Rev. Anal. Chem.*, 2015, **8**, 61-80.
32. H. Awad, M. M. Khamis and A. El-Aneed, *Appl. Spectrosc. Rev.*, 2015, **50**, 158-175.
33. M.-Z. Huang, C.-H. Yuan, S.-C. Cheng, Y.-T. Cho and J. Shiea, *Annu. Rev. Anal. Chem.*, 2010, **3**, 43-65.
34. C. Zwiener and F. H. Frimmel, *Anal. Bioanal. Chem.*, 2004, **378**, 851-861.
35. M. Herderich, E. Richling, R. Roscher, C. Schneider, W. Schwab, H. U. Humpf and P. Schreier, *Chromatographia*, 1997, **45**, 127-132.
36. J. S. Becker and N. Jakubowski, *Chem. Soc. Rev.*, 2009, **38**, 1969-1983.
37. C. Uetrecht and A. J. R. Heck, *Angew. Chem., Int. Ed.*, 2011, **50**, 8248-8262.
38. J. Fenn, M. Mann, C. Meng, S. Wong and C. Whitehouse, *Science*, 1989, **246**, 64-71.
39. M. Wilm, *Mol. Cell. Proteomics*, 2011, **10**, M111.009407.
40. H. Metwally, R. G. McAllister and L. Konermann, *Anal. Chem.*, 2015, **87**, 2434-2442.
41. G. R. Agnes and G. Horlick, *Appl. Spectrosc.*, 1995, **49**, 324-334.
42. L. W. McDonald, J. A. Campbell and S. B. Clark, *Anal. Chem.*, 2014, **86**, 1023-1029.
43. L. J. Kricka, *Clin. Chem.*, 1998, **44**, 2008-2014.
44. K. B. Lynch, A. Chen and S. Liu, *Talanta*, 2018, **177**, 94-103.
45. G. McMahon, *Analytical Instrumentation: A Guide to Laboratory, Portable and Miniaturized Instruments*, John Wiley & Sons, Ltd, West Sussex, England, 2007.
46. Z. Ouyang and R. G. Cooks, *Annu. Rev. Anal. Chem.*, 2009, **2**, 187-214.
47. D. T. Snyder, C. J. Pulliam, Z. Ouyang and R. G. Cooks, *Anal. Chem.*, 2016, **88**, 2-29.
48. Z. Takáts, J. M. Wiseman, B. Gologan and R. G. Cooks, *Science*, 2004, **306**, 471-473.
49. J. Liu, H. Wang, N. E. Manicke, J.-M. Lin, R. G. Cooks and Z. Ouyang, *Anal. Chem.*, 2010, **82**, 2463-2471.
50. T. Cserfalvi and P. Mezei, *J. Anal. At. Spectrom*, 1994, **9**, 345-349.
51. M. R. Webb, F. J. Andrade, G. Gamez, R. McCrindle and G. M. Hieftje, *J. Anal. At. Spectrom*, 2005, **20**, 1218-1225.
52. R. K. Marcus and W. C. Davis, *Anal. Chem.*, 2001, **73**, 2903-2910.

53. R. K. Marcus, B. T. Manard and C. D. Quarles, *J. Anal. At. Spectrom*, 2017, **32**, 704-716.
54. K. A. Hall and R. K. Marcus, *J. Anal. At. Spectrom*, 2019, **34**, 2428-2439.
55. K. A. Hall, H. W. Paing, M. R. Webb and R. K. Marcus, *Spectrochim. Acta, Part B*, 2019, **154**, 33-42.
56. H. W. Paing, K. A. Hall and R. K. Marcus, *Spectrochim. Acta, Part B*, 2019, **155**, 99-106.
57. C. D. Quarles, A. J. Carado, C. J. Barinaga, D. W. Koppenaal and R. K. Marcus, *Anal. Bioanal. Chem.*, 2012, **402**, 261-268.
58. R. K. Marcus, C. D. Quarles, C. J. Barinaga, A. J. Carado and D. W. Koppenaal, *Anal. Chem.*, 2011, **83**, 2425-2429.
59. L. X. Zhang, B. T. Manard, S. K. Kappel and R. K. Marcus, *Anal. Bioanal. Chem.*, 2014, **406**, 7497-7509.
60. E. D. Hoegg, C. J. Barinaga, G. J. Hager, G. L. Hart, D. W. Koppenaal and R. K. Marcus, *J. Am. Soc. Mass Spectrom.*, 2016, **27**, 1393-1403.
61. E. D. Hoegg, C. J. Barinaga, G. J. Hager, G. L. Hart, D. W. Koppenaal and R. K. Marcus, *J. Anal. At. Spectrom*, 2016, **31**, 2355-2362.
62. E. D. Hoegg, R. K. Marcus, G. J. Hager, G. L. Hart and D. W. Koppenaal, *J. Anal. At. Spectrom*, 2018, **33**, 251-259.
63. E. D. Hoegg, R. K. Marcus, D. W. Koppenaal, J. Irvahn, G. J. Hager and G. L. Hart, *Rapid Commun. Mass Spectrom.*, 2017, **31**, 1534-1540.
64. E. D. Hoegg, B. T. Manard, E. M. Wylie, K. J. Mathew, C. F. Ottenfeld and R. K. Marcus, *J. Am. Soc. Mass Spectrom.*, 2019, **30**, 278-288.
65. L. X. Zhang, B. T. Manard, B. A. Powell and R. K. Marcus, *Anal. Chem.*, 2015, **87**, 7218-7225.
66. L. X. Zhang and R. K. Marcus, *J. Anal. At. Spectrom*, 2016, **31**, 145-151.
67. R. K. Marcus, C. Q. Burdette, B. T. Manard and L. X. Zhang, *Anal. Bioanal. Chem.*, 2013, **405**, 8171-8184.
68. H. W. Paing, T. J. Bryant, C. D. Quarles and R. K. Marcus, *Anal. Chem.*, 2020, **92**, 12622-12629.

CHAPTER II

COUPLING OF THE LIQUID SAMPLING – ATMOSPHERIC PRESSURE GLOW DISCHARGE (LS-APGD) IONIZATION SOURCE WITH A COMMERCIAL TRIPLE QUADRUPOLE MASS SPECTROMETER

2.1 Introduction

Inductively-coupled plasma mass spectrometry (ICP-MS) is a widely used method and arguably among the most powerful methods for elemental analysis. Introduced commercially in 1983, ICP-MS gained quick acceptance due to its incredible sensitivity, robustness, and ability to determine elements in various matrices.[1, 2] While having numerous benefits, ICP-MS suffers from relatively high instrument cost and high consumable use. Spectral interferences had been among the notable drawbacks of this method, leading to a variety of methodologies being developed, including cool plasma conditions and high-resolution sector-field ICP-MS to overcome this issue.[3-5] The most prominent developments for overcoming spectral interferences was the introduction of collision-reaction cells (CRC) used in conjunction with quadrupole mass analyzers to alleviate spectral interferences through chemical reactions to "shift" their masses or through charge neutralization to eliminate the interfering ions.[6-11]

The first commercial iteration of these systems introduced a collision-reaction cell (CRC) followed by the mass-resolving quadrupole mass filter, as first suggested by Rowan and Houk.[12] This cell allows for many spectral interferences to be circumvented through the control of the gas phase reactions taking place. It is important to note that such reactions were thermodynamically driven and not due to kinematics, as is common in

organic/molecular mass spectrometry/mass spectrometry (MS/MS).[13, 14] Unfortunately, with no mass-resolving quadrupole located before the CRC, there is no control over the identity of the reactants entering the cells, leading to progeny ions that potentially formed new spectral interferences.[11] After nearly 20 years of prominence, the CRC-quadrupole arrangement is challenged with the introduction of the ICP triple quadrupole mass spectrometer (QqQ), containing a mass-selective quadrupole mass filter prior to the CRC.[11, 15-17] This allows a specific mass (or range) of ions to be introduced to the CRC, providing increased control over the reactions and collisions that occur. Some of the major interferents this has helped overcome include both argide and doubly charged species. Argide species such as Ar_2^+ are interferents for Se, but by use of a reaction cell with O_2 as the reagent, Se can be measured as SeO^+ with no interferences. Additionally, the formation of doubly charged analyte ions such as Yb^{++} can be interferents for other analytes such as Sr, which can again be overcome using an O_2 reaction gas to measure SrO^+.[11] This configuration has been largely successful in the task of further reducing spectral interferences that plague ICP-MS.

While the ICP-QqQ instruments are effective for reducing interferences, the cost associated with their operation is still appreciable. Beyond initial capital costs, ICP-MS instruments (in general) require 15-20 L min^{-1} of Ar gas to maintain the plasma, plus additional specialty gases for the CRC. In addition to large gas flow rates and high power requirements, solution sample introduction rates up to 0.4 mL min^{-1} make large sample volumes (and coincident waste management) a necessity.[18] These requirements result in ICP-MS instruments which are unsuitable for applications such as field deployment or

industrial situations such as at-line biopharmaceutical production environments where size, operational overhead, and simplicity are at a premium. To this end, miniaturized instrumentation (ionization sources and mass analyzers) have been of continued interest.[19]

An important current focus in atomic spectrometry is the development of miniaturized plasmas having low power consumption, low capital cost, and potentially lower consumable use. Numerous reviews detail the promising results of these devices as they apply to optical emission spectroscopy (OES).[20-22] One particular family of devices was first introduced by Cserfalvi et al. as the electrolyte cathode discharge (ELCAD), developed towards the elemental analysis of water and waste water samples.[23-25] These designs utilize a flowing electrolytic solution to which a plasma is generated. Since this introduction, a number of other studies have improved upon this design, notably the solution cathode glow discharge developed by Hieftje et al.[26] The liquid sampling – atmospheric pressure glow discharge (LS-APGD) developed by Marcus et al., is another source of related design and has been found to have many attractive features.[27] Originally implemented as an OES source,[28] MS sampling has borne out a number of positive attributes towards applications in elemental, isotopic, and molecular species analysis.[29-33] Of particular relevance regarding reduced-overhead elemental MS, the LS-APGD has been shown to run in a total sample consumption mode, with solution and He gas flow rates of <40 µL min^{-1} and <1 L min^{-1}, respectively. Operation with d.c. powers of less than 50 W versus the 1 – 2 kW of rf power for the ICP is a substantial difference as well. The significantly lower operation and consumable costs, and lower power for the LS-APGD

make it a promising candidate for those situations not conducive to the use of ICP-MS instruments.

To date, the LS-APGD has been almost exclusively coupled to trapping-type mass spectrometers.[30, 33-37] These couplings have shown promising results in elemental and isotope ratio analysis with LODs in the low ng mL^{-1} to pg mL^{-1} range and providing uranium isotope ratios that meet all applicable IAEA international target values.[33, 35, 36] However, the use of these trapping-type instruments is atypical for elemental analysis, which rely on quadrupole or sector field instruments. Very recently, this laboratory has described initial efforts in coupling the microplasma to a reduced-format single-quadrupole instrument.[38] While the array of MS platforms has been diverse, many fundamental questions exist as to the chemical species which exist in the plasma. For this reason, a commercial 'organic' triple quadrupole mass spectrometer is utilized here as a means of affecting many diverse MS modalities. While not pertinent in terms of cost or complexity issues regarding miniaturization, the numerous scan modes available to triple-quadrupole instruments as applied in liquid chromatography detection could provide deeper insights into what types of species are being formed within the plasma. Additionally, diverse methods for the reduction of spectral interferences can be investigated to perhaps yield improved analytical figures of merit.

Presented here is the coupling of the LS-APGD with a standard ThermoScientific TSQ Quantum Access MAX triple-quadrupole mass spectrometer. This instrument typically employs electrospray (ESI) or atmospheric pressure chemical ionization (APCI) sources coupled with liquid chromatography for separation and analysis of organic species

such as proteins or environmental species. To be clear, the driving force for this particular coupling is the development of a highly versatile tool to study plasma fundamentals. A thorough multi-analyte, parametric evaluation was performed employing a design of experiment (DoE) approach to optimize both signal intensity and signal-to-background ratios (S/B). The included plasma/sampling parameters were discharge current, liquid (sample) flow rate, sheath gas flow rate, distance between the sampling cone and the plasma, and interelectrode gap. Since the LS-APGD has been found to produce oxides, hydroxides, and water clusters, the various MS/MS modes; precursor ion, product ion, and neutral loss scans, were investigated. At the optimized source conditions, the influence of in-source collision-induced dissociation (CID) voltage, Q2 gas pressure (Ar), and CID energy were evaluated for the purpose of reducing the prevalence of these species and improving S/B ratios. Additionally, LODs were determined simultaneously for a Rb, Ag, Tl, and U multi-element solution. It is believed that while this pairing does not yet yield the same levels of sensitivity seen in couplings with Orbitrap mass spectrometers, it will yield a wealth of qualitative information relevant to improved LS-APGD operation in the future.

2.2 Experimental

2.2.1 Source Design

The design of the LS-APGD for interfacing with a mass spectrometer has been previously described.[37] As depicted in Fig. 2.1, the cathode consists of a fused silica capillary (280 µm i.d., 580 µm o.d., Restek Corporation, Bellefonte, PA) through which an electrolytic solution (sample) is introduced to the plasma (10-80 µL min^{-1}) via a syringe

pump (Chemyx Fusion 100, Chemyx, Stafford, TX). The fused silica capillary is housed within an electrically grounded stainless-steel capillary (316 SS, 0.8 mm i.d., 1.6 mm o.d., IDEX Health and Science, Oak Harbor, WA) through which a He sheath gas flows (0.2-0.3 L min^{-1}). The anode is composed of a solid metal electrode (SS, weldable feedthrough; MDC vacuum products, LLC, Hayward, CA, USA) which has a positive potential applied via a Spellman SP60 power supply (0-60 mA, 0-1 kV; Spellman, Hauppauge, NY). The solution cathode is placed in line with the sampling cone (0.5 - 4 mm separation) of the mass spectrometer with the anode being displaced perpendicularly (0.5 – 2 mm), forming the discharge between them.

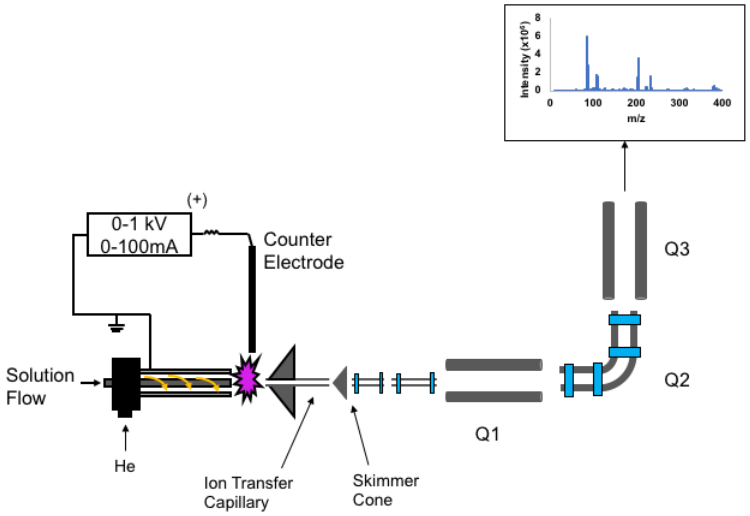

Figure 2.1: Diagrammatic representation of the system components of the LS-APGD coupled with the TSQ Quantum Access MAX mass spectrometer.

2.2.2 Mass Spectrometer System

In this work, the LS-APGD was interfaced with a ThermoScientific (San Jose, CA) TSQ Quantum Access MAX triple-quadrupole mass spectrometer requiring no modification to the instrument other than removing the equipped ESI source and mounting

the LS-APGD platform. As depicted in Fig. 2.1, the TSQ system is comprised of the ion sampling capillary and ion optics, the triple quadrupole analyzer, and an electron multiplier detector with a conversion dynode. Different from ICP-QqQ platforms, the second quadrupole in this system is a bent quadrupole into which a collision gas (Ar) can be introduced to affect collisional dissociation (CID). This allows for the ability to perform many different MS/MS operations including parent ion scans, product ion scans, and neutral loss scans.[14] In addition, loosely bound species (usually solvated ions) can be dissociated using the in-source collision induced dissociation by applying a voltage (CID = 0 – 200 V) between the end of the ion transfer capillary and the skimmer cone. These system parameters are controlled utilizing the Thermo Xcalibur and TSQ Tune Master software systems. Data collected in a full scan mode, or in MS/MS experiments were obtained using a scan rate of 0.5 s across the mass range. In addition, these spectra were collected using the Tune Master software spectrum averaging function, which averages a user-defined number of scans, in this case 10, so that each resulting data point/spectrum is an average of 10 scans. For data collected in the selected ion monitoring (SIM) mode, a scan rate of 0.1 seconds per peak was used as well as the spectrum averaging of 10 scans. In the cases involving ion source optimization and quantitative analysis, Q1 was employed as the mass analyzer while Q2 and Q3 were operated in rf-only modes, serving simply as ion guides.

2.2.3 Design of Experiment

The evaluation of the LS-APGD operating parameters was accomplished by designing an experimental plan using JMP software (SAS Institute Inc., Cary, NC). An

initial screening study was carried out in order to rule out non-viable conditions, followed by a custom design experiment was selected and set to find points at which the signal (S) and signal-to-background ratio (S/B) were maximized. Three replicates per condition were randomly placed, resulting in a total of 36 sets of parameters. A 10 µg mL^{-1} multi-element solution was injected (50 µL) at each set of conditions and the analyte ions were determined using selected ion monitoring (SIM). The analyte peak area for each injection was measured, and the S/B was determined using the analyte peak area and the time-equivalent peak area present directly prior to the injection.

This type of parameterization methodology allows for a thorough evaluation without overlooking inter-parametric effects. The resulting plots from these experiments are shown as bar graphs where the vertical line represents the level of significance. Bars that extend beyond this line indicate a significant influence on the responses, while those that do not, represent an insignificant effect on the targeted responses (S or S/B).[39]

2.2.4 Sample Preparation

A stock multi-element solution covering a broad mass range and different analyte chemistries was prepared from elemental standards (Rb, Ag, and U; High Purity Standards, Charleston, SC) or nitrate salts (Tl; Beantown Chemical, Hudson, NH). The nitrate salts were dissolved using 2% HNO_3 to prepare a 1000 µg mL^{-1} standard solution. The stock multi-element solution was prepared by diluting the standards in 2% HNO_3 to prepare a 10 µg mL^{-1} solution. The test solutions for the calibration curve were made through serial dilution of the stock solution

2.3 Results and Discussion

2.3.1 Parametric Evaluation and Coupling Characteristics of the LS-APGD

Prior to this work, the LS-APGD had been coupled almost exclusively to trapping-type mass spectrometers.[30, 33, 35, 36] Previous couplings to the LCQ and Orbitrap instruments explored the dependencies of the signal intensity, S/B ratio, and isotope ratio accuracy on plasma operation parameters. Relevant conditions include discharge current, solution flow rate, sheath gas flow rate, interelectrode gap, and distance from the ion sampling cone. In addition, MS sampling parameters including in-source CID voltage and higher energy collisional dissociation (HCD) were evaluated.[30, 35] In none of the previous efforts was a DoE approach employed.

Through the variety of MS studies using the LS-APGD, the conditions used have seen significant variation between the different couplings. Initial MS studies by Marcus et al. showed that the ideal conditions included low discharge currents (5-10 mA) and low liquid flow rates (<10 µL min^{-1}). In addition, the sheath gas flow rate was optimized to 0.9 L min^{-1} with a ~1 cm sampling distance.[30, 37] More recent studies using the Exactive Orbitrap platform showed that higher liquid flow rates and discharge currents, and lower sheath gas flow rates gave optimal response relative to the formation of the analyte dioxide cation of uranium (UO_2^+).[35] Due to differences in the ion sampling apparatus from the other instruments, a new source optimization was undertaken.

The parameters discussed above were evaluated via the DoE approach with the test matrix generated using the JMP software. A DoE approach models the response of one or more dependent variables based on changing a number of independent variables. In this

case, the independent variables were those listed in Table 2.1, while the dependent variables monitored were the analyte intensity and signal-to-background ratio (S/B). With a software-designed set of parameters probed, the effects of each parameter, as well as inter-parametric effects can be monitored, and their significance determined. Due to the wide range of parameters that have been investigated in previous work, an initial screening study was performed to remove any outlying conditions relative to TSQ sampling. This initial study was used to rule out parameters which provided poor results or were unable to sustain a plasma. Most significantly, the initial study found that the TSQ instrument is unable to handle He sheath gas flow rates above 0.2 L min^{-1} due to increased pressures that trip a vacuum override, disabling high voltage boards in the instrument. This led to significant narrowing of many of the parameters as the lower gas flow rates resulted in an inability to sustain a plasma at conditions of higher currents (>40 mA) wherein capillaries melt and lower currents (<30 mA) being unable to maintain a plasma at any reasonable solution flow rate. The ultimate parametric test values are detailed in Table 2.1.

Table 2.1: Ranges of DoE-evaluated LS-APGD operating conditions and their optimized values.

Parameter	*Conditions Tested*	*Optimized Conditions*
Discharge Current	30 - 40 mA	30 mA
Liquid Flow	5 - 30 µL min^{-1}	25 µL min^{-1}
Electrode Gap	0.5 - 2 mm	1 mm
Distance from Sampling Cone	1 - 4 mm	1.5 mm
Gas flow	-	0.2 L min^{-1}

The parametric evaluation was designed using analyte signal and analyte S/B ratios of Rb, Ag, Tl, and U as target responses with the goal of maximizing both. These analytes were used as they cover a range of ionization potentials and chemistries for masses across the periodic table. Figures 2.2a and b depict the significance of each parameter on the analyte signal (S) response and S/B, respectively. The dashed vertical line in each graph represents the point at which a parameter has a statistically significant effect. In addition, the inter-parametric effects were evaluated and are denoted with a "*" between the two parameters in the legend. Based on Fig. 2.2a, a number of parameters are shown to have effects on the analyte intensities, three of which are statistically significant. Most significant overall was the effect of the cathode distance from the sampling cone, which resulted in a dramatic decrease in analyte intensity at sampling distances greater than 2 mm. This contradicts previous work on the Thermo LCQ which showed an increase in all analyte signal intensity with an increase in the sampling distance.[30] Apart from the sampling distance, a number of inter-parametric effects were observed, the most significant being the cross between the interelectrode gap and discharge current. At 30 mA, the electrode gap has a slightly negative effect on the analyte intensity which is enhanced by the increasing of the current. Different from the other mass analyzers, the TSQ has limited pumping capacity towards helium, limiting the range of sheath gas flow rates. A reduced cooling efficiency at higher currents lead to increased desolvation within the solution capillary and less analyte entering the plasma. While the distance from the sampling cone itself plays a dominant role, its effect is intertwined with both the current and liquid flow rates. It is likely however, that due to the dominating effect the distance from the sampling

cone has on the signal intensity, that these inter-parametric effects are influenced very little by the current and liquid flow rates.

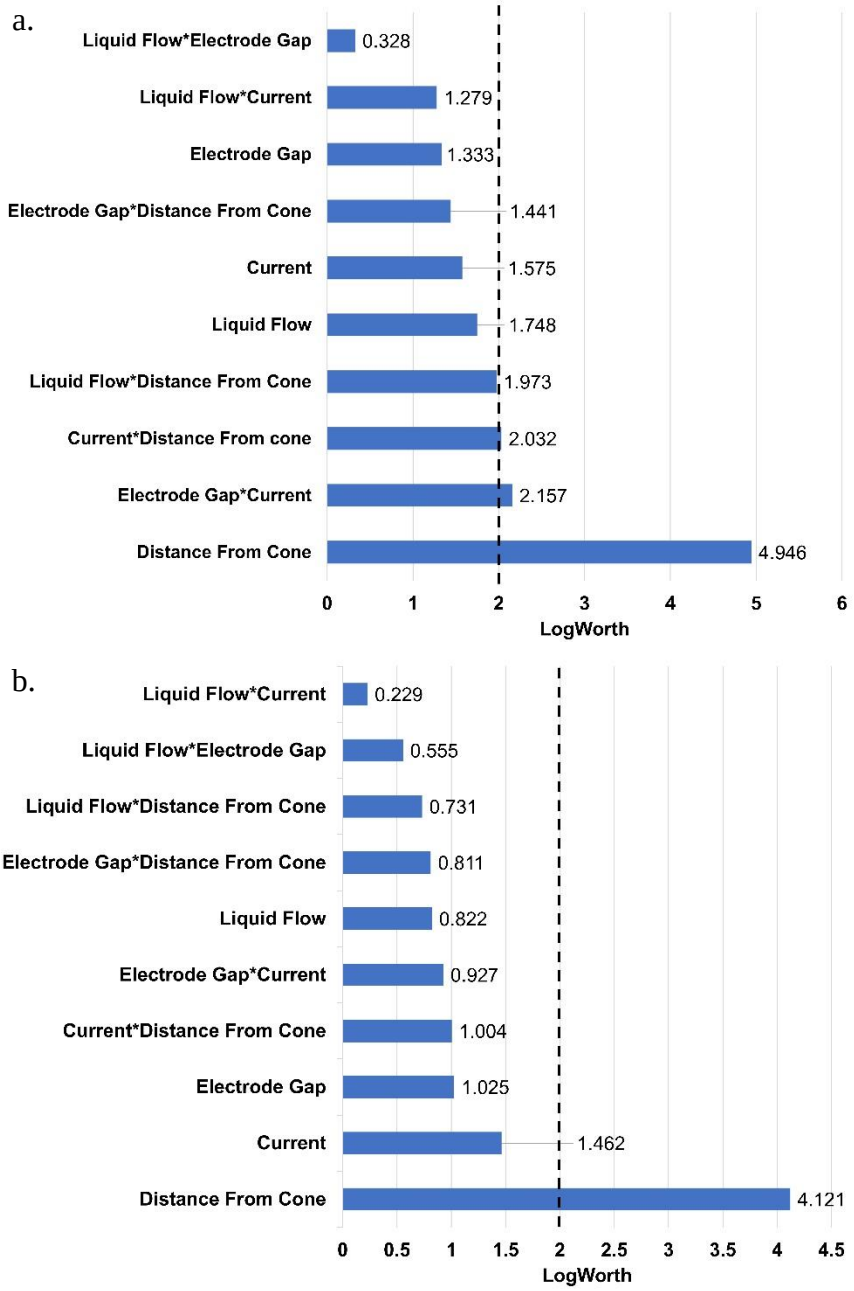

Figure 2.2: Bar graphs reflecting the combined significance of each operating parameter (and cross effects) on the a) analyte signal intensities (S) and b) analyte signal-to-background ratios (S/B). Analyte concentrations = 10 µg mL^{-1} (each), target analyte isotopes: ^{85}Rb, ^{107}Ag, ^{205}Tl, and $^{238}U^{16}O_2$.

Figure 2.2b, details the potential influences of the parameters on the S/B ratios, again revealing that the distance from the sampling cone to have the largest influence. In this case, it is the only parameter with a statistically significant effect, showing a decrease in the S/B ratio for all elements as the displacement increased. While this is seen to have a large effect on the signal intensity, with the S/B decreasing with distance it appears to have a less significant effect on the background component. From Fig. 2.2b, some dependence on the current is also seen, although it is not statistically significant. As seen with previous work, higher currents do lead to increased background species lowering the S/B.[30] Overall, the dependences (or the lack thereof) of the S/B on the various parameters simply reflect the fact that the sources of both S and B are the same. The final optimized conditions for each parameter were determined and are shown in Table 2.1.

2.3.2 Optimization of In-Source CID Energy and Q2 Gas Pressure

In previous MS couplings of the LS-APGD, the instrument was optimized to reduce interfering ions using in-source CID and the higher-energy collisional dissociation (HCD) cell on Exactive instruments[30, 35] and the CID functionality within the Paul trap of the LCQ.[30] The TSQ, as well, employs a method for in-source CID by applying a potential difference between the ion transfer capillary and the skimmer cone. While no HCD cell is present in this instrument, the argon gas supplied to the Q2 collision cell affects the same processes. To optimize these aspects, 50 µL injections of the 10 µg mL^{-1} multi-element solution were performed, with the resulting S/B ratio for each analyte computed and used as the test metric. Triplicate injections were performed while varying the in-source CID 0

– 200 V in 25 V increments (with no CID occurring in Q2). After optimization, the same was done for the Q2 gas, varying the pressure from 0 – 5 mTorr at 0.5 mTorr increments.

Previous efforts have shown that in-source CID has a major effect on the levels of background ions related to the aqueous solvent; i.e., ions of the form $M(H_2O)_n^+$ and $(H_2O)_nH^+$. The former species dilute target analyte intensities, while the latter add to spectral background. In principle, increases in energy should better affect dissociation, though the total ion throughput suffers as well with increasing energy. Figure A.1 (in Supplementary Information) shows the resulting data from the in-source CID evaluation, suggesting that ~175 V provides the best compromise in S/B for the target analytes. In the case of Rb, Ag, and Tl the loss of background ions generally dominates as the voltage is increased to that point, beyond which the overall transmission begins to suffer. A more interesting scenario is realized in the case of the desired UO_2^+ (m/z = 270 Da) target. The tri-hydrated nitrate form of that ion, $UO_2(NO_3)(H_2O)_3^+$ (m/z = 386 Da) is readily dissociated to the target at very low (<30 eV) potentials, yielding the desired dioxide species. Indeed, the hydrated ion is reduced to near-background levels above 50 eV. The combination of these effects leads to the pronounced improvement in S/B for UO_2^+ at an ITC potential of 175 eV. Overall, operation at that voltage provides levels of background species reductions as seen on previous platforms.

In addition to in-source CID, this instrument offers the ability to induce dissociative collisions in Q2. This involves pressurizing Q2 and applying a potential offset across the quadrupole relative to the exit of Q1. Unfortunately, due to software limitations, the potential can only be changed during MS/MS scans. Changing this potential would increase

the velocity at which the collisions would occur, increasing dissociation. Without this potential, the argon gas pressure in Q2 will still induce dissociation, but to a lesser degree. The effect of the Q2 argon pressure was observed by setting the in-source CID to its optimal point, 175 V, and varying the gas pressure. Since the in-source CID fully dissociates the hydrated uranium species at 386 m/z (Fig. A.1), it was not monitored in this figure. As in the case of the in-source CID, and seen in Fig. A.2, there are counteracting effects in setting the gas pressure. At low pressures, the extent of CID increases with pressure, while at higher values the overall throughput of Q2 decreases. In general, the desired analyte ions are far less affected by the increases in gas pressure than the corresponding signals of the background, with those species dropping more precipitously at 1.5 mTorr. This is observed to have a large effect on S/B for all analytes, although they do not all have a maximum at 1.5 mTorr. This is due to the larger collisional cross section of the background molecular species.[40] The 1.5 mTorr value was ultimately chosen as most acceptable based on the spectral quality observed for injections at low concentrations (250 ng mL^{-1}), where higher pressures yielded poor S/B characteristics.

2.3.3 Application of Different MS/MS Scan Modes

With the LS-APGD sampling by the TSQ optimized, the full benefits of a triple quadrupole instrument, the variety of MS/MS scan modes, were investigated to survey the types of fundamental information available to improve understanding of the processing occurring in the microplasma. Here again, this instrument differs substantially from those used in ICP-QqQ-MS where Q1 sets the entry masses into Q2 which is operated as a CRC, alleviating the presence of undesired secondary reaction products; the goal being better

analytical accuracy. Here we wish to identify specific ion species and relate them to fundamental plasma processes. As a starting point for this set of illustrations, Fig. 2.3 shows a full scan from m/z = 10 to 400 Da of the 25 µg mL^{-1} multi-element (Rb, Ag, Tl, U) solution. From this spectrum, numerous species other than the main analyte signals are observed. While the analyte signals are more intense, there is a variety of background ions which can be generally attributed to water-related species. In addition, a number of the analytes also form oxides, hydrated species, salts and clusters. The value of having the full MS/MS experimental arsenal allows assignment of species, such as that labeled Ag_2X. In that case, it is easy to visually assign the identity as a Ag-dimer, but MS/MS is needed for correct identification. The various MS/MS modalities are demonstrated below for this primary test solution.

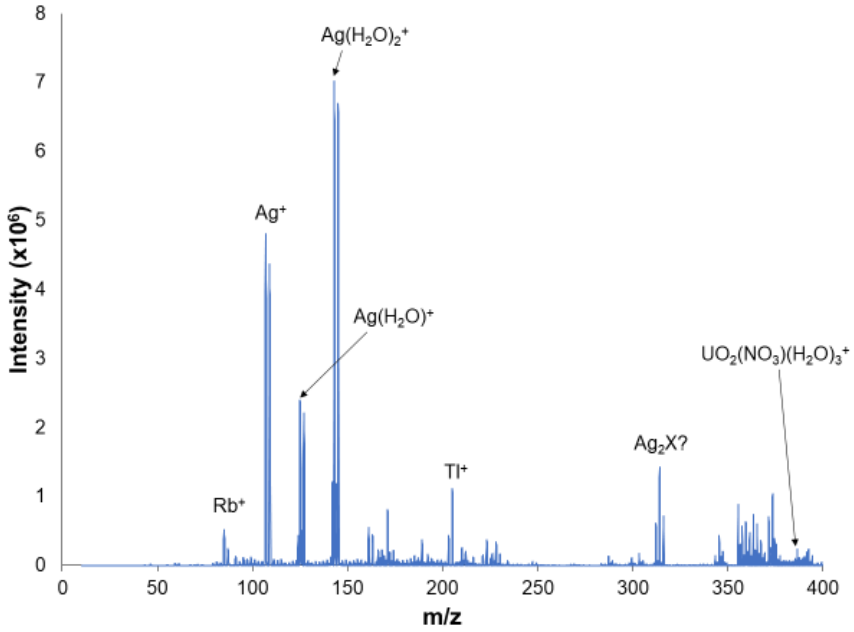

Figure 2.3: LS-APGD mass spectrum for a 25 µg mL^{-1} solution containing Rb, Ag, Tl, and U. The spectrum shown employs no collisional dissociation methods, representing the native population of ions sampled into the mass spectrometer. Discharge conditions were those presented in Table 2.1.

To investigate what the various molecular species might be, parent ion, neutral loss, and product ion scanning modes were utilized. The main concepts of each scan are illustrated in Fig. 2.4. A quick parametric optimization was undertaken regarding the Q2 gas pressure and collisional energy for each of these scan types. In the first case, parent ion scans, the principle idea is to identify which of the ions produced in the plasma can be dissociated to the target analyte ions. In this mode, Q1 is scanned to successively higher masses, those ions are subjected to CID in Q2, and Q3 is held constant at the target ion m/z. Figure 2.5 is a comprehensive set of parent ion scans for the various analyte ions in the test mixture, reflecting the molecular ions that fragment to yield the identified analyte species. The spectral information can be quite enlightening.

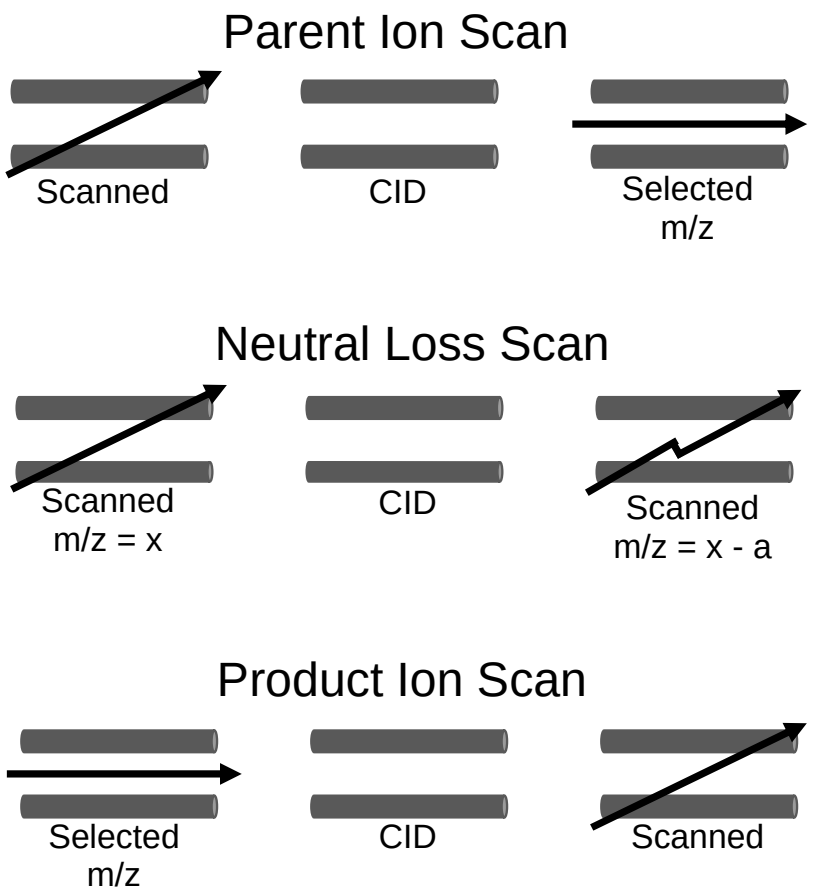

Figure 2.4: Diagrammatic representation of the operating principles for the various MS/MS modes available in the LS-APGD/TSQ pairing. In each scan mode, Q2 is used for collisional dissociation, pressurizing the cell with Ar and applying an offset potential. Q1 is used to control what enters into Q2, while Q3 determines which masses reach the detector.

As a simple example, for the case of ^{205}Tl, the green-colored spectrum identifies the fact that Tl^+ is the primary ion entering Q1, while $Tl(H_2O)^+$ (m/z = 223 Da) makes up ~20% of Tl species, and $Tl(NOH)^+$ (m/z = 246 Da) is ~3% of the total thallium ion signal. While the monoatomic Tl^+ is the primary species for that element, the case is completely different for UO_2^+ where there is a plethora of higher mass species that dissociate to that ion.

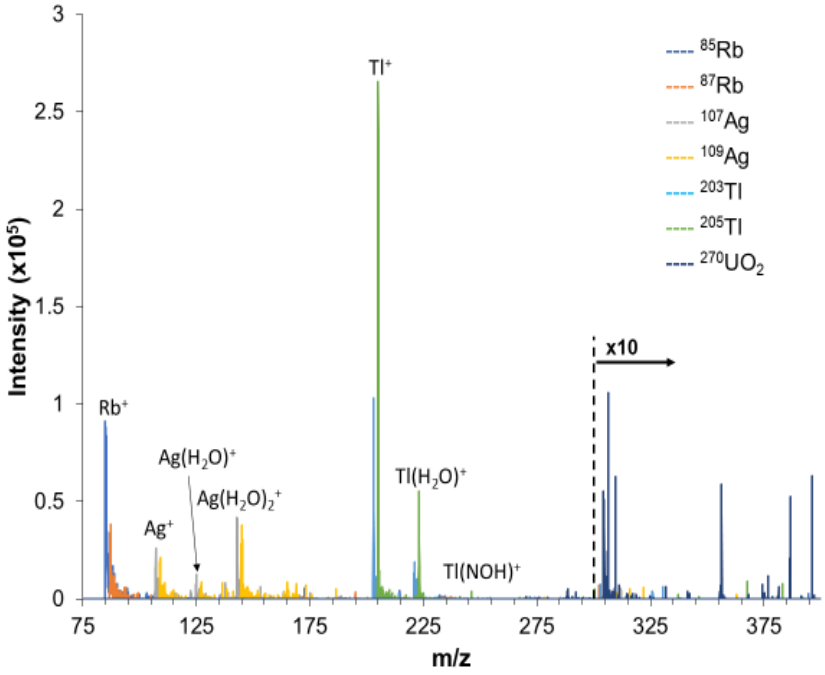

Figure 2.5: Parent ion scan performed for a 25 µg mL^{-1} solution containing Rb, Ag, Tl, and U. The entire mass range was allowed into Q2 for dissociation, while Q3 isolated each analyte isotope. All responses above m/z = 300 Da have been multiplied 10x. Discharge conditions were those presented in Table 2.1.

The evaluation of roles of the pole bias and target gas pressure was completed in the parent ion scan mode as a means of eventually generating the largest analyte ion signals (bare metal ions and UO_2^+). The extracted ion chromatograms (i.e., the integrated responses) for all species of the selected masses in Q3 of each analyte isotope, were monitored under each set of CID conditions. The maximum values in the chromatograms are expected to be the point in which optimum fragmentation occurs to yield the analyte species. Seen in Fig. A.3a, a maximum yield with respect to the collision energy is found at 25 V for each of the analyte species. The response reflects greater levels of efficiency with increasing voltage, followed by ion losses (scattering) due to excess kinetic energies. In Fig. A.3b, there is no clear, universal optimum in the Q2 gas pressure. Detailed

interrogation across the individual spectra suggested that the greatest spectral clarity relative to the background water-related ions was obtained at a Q2 cell pressure of 1.5 mTorr Ar. Thus, a Q2 bias of 25 V and pressure of 1.5 mTorr Ar was used through the remainder of the studies.

The neutral loss scan mode was utilized to identify the variety of water-related species formed within the plasma. This scan looks for any peaks that lose a mass of a specified value (e.g., 18 Da for H_2O) when collisional dissociation is applied, both Q1 and Q3 are set to scan ranges of the same width though they are offset by the user defined mass. For example, when identifying species that lose H_2O, Q1 may be set to scan from 50-200 m/z whereas Q3 is scanning from 32-182 m/z. Shown in Fig. 2.6, much of the spectra (from diverse neutral losses) are primarily made up of clusters of two or fewer water molecules. This mode was optimized in the same manner as the parent ion scan, monitoring the extracted ion chromatograms, with the optimum Q2 values yielding losses of those species being a pole bias of 25 V and a target gas pressure or 0.5 mTorr Ar determined (shown in Figs. A.4 and A.5). The preponderance of water related species is expected as the LS-APGD is a water-based plasma. It is important to note that when looking at the water species in Fig. 2.6, that the species present have considerably lower intensities than the analyte species seen in Fig. 2.3 (though the spectra are taken with the same plasma conditions). Of course, the ions detected are charged species, with the vast majority carrying the charge of a single proton (H^+). Based on the scan format, Fig. 2.6 shows that the vast majority of species that lose water-related ions are themselves protonated water clusters. Indeed, the spectra suggest the presence of clusters that can lose up to 8 water

molecules. Thus, very large water clusters are present. It should be noted that the same sort of scan would identify clusters containing remnants of the HNO_3 electrolyte in solution.

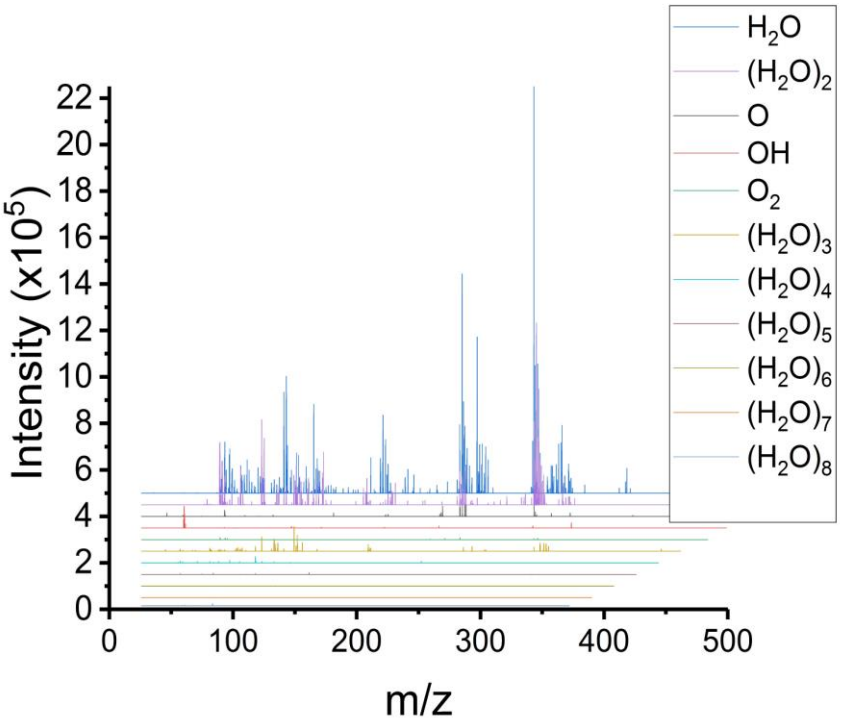

Figure 2.6: Neutral loss spectra performed for a 25 μg mL^{-1} solution containing Rb, Ag, Tl, and U. The mass offset between Q1 and Q3 was to monitor the loss of oxide, hydroxide, and various water-cluster species. Discharge conditions were those presented in Table 2.1.

In addition to parent ion and neutral loss scans, product ion scans were also investigated. In this scan mode, Q1 is set to allow only a selected mass through, Q2 is used for fragmentation of the selected ion, and Q3 is set to scan over a defined range to identify the product fragment ions. This is the more-or-less classic MS/MS mode used to identify organic species as a specific peak can be isolated and fragmented in order to determine its identity. As an example of the investigatory power of MS/MS for plasma diagnostics, Fig. 2.7 shows a product scan isolating masses 312, 314, and 316 which are identified in Fig. 2.3 as being related to a dimer of Ag. By fragmenting these peaks at the set conditions, the

identity of parent ion can be inferred, with sufficient fragmentation to elucidate the complex' identity. The parent peak species are entirely fragmented by CID, with the loss of one water (loss of 18 from the parents) and two water molecules being the prominent products. Very little of the bare Ag metal ions are present under these CID conditions, which is not a surprise as the Ag-Ag bond energy is ~7 eV.[41] The low intensity products, though, confirm the existence of the dimer in the parent. Selective dissociation of the 312 Da parent yields entirely ^{107}Ag isotope signals, dissociation of 314 Da yields both ^{107}Ag and ^{109}Ag isotopes, and the 316 Da parent is composed entirely of the ^{109}Ag isotope; confirming that this is indeed a Ag dimer. With Ag_2 being the base unit and the isotope cluster centered at 276 Da representing the loss of two water molecules, means that the remaining mass difference can be attributed to a NO_3 unit, and so the complex can be identified as $Ag_2(NO_3)(H_2O)_2$. As shown here, this type of scan scenario can be extremely beneficial when trying to determine the identity of unknown species.

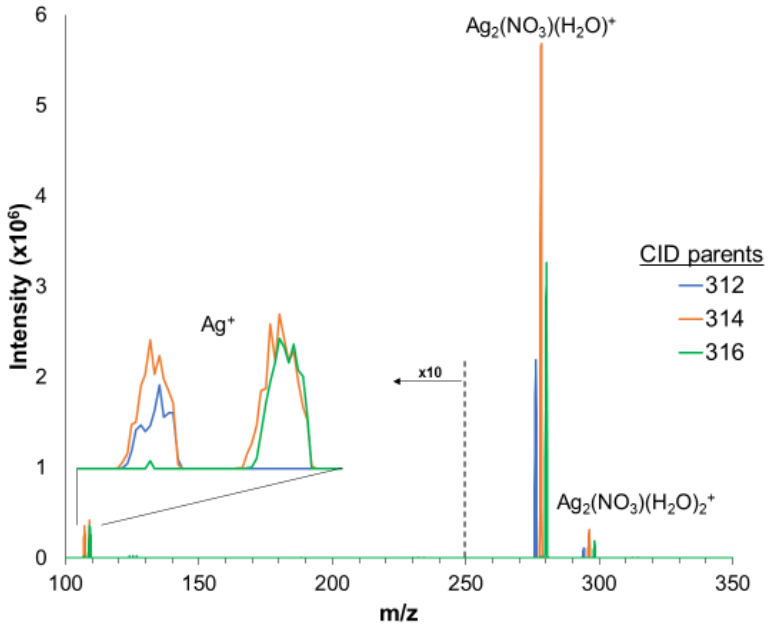

Figure 2.7: Product ion scan for the isotopes of the Ag dimer molecular species at m/z = 312, 314, and 316 Da obtained from a 25 µg mL^{-1} solution. Masses below 250 are multiplied 10x. Discharge conditions were those optimized in Table 2.1.

In addition to these directed-scan methods, the use of the collisional cell (Q2) for the generic removal of unwanted molecular species was investigated. CID was performed operating Q1 in an rf-only (band pass) mode, pressurizing the Q2 cell with argon and applying an offset potential in Q2, and operating Q3 in a mass-resolving mode. In this mode, the larger molecular ions will be expected to undergo an increased number of collisions, reducing the intensity through scattering and dissociation, while leaving the atomic species largely unchanged. To illustrate this simple strategy, a 25 µg mL^{-1} Pb solution was utilized as it forms a number of molecular species in the plasma. No in-source CID is applied in this instance so as to illustrate worst-case spectral features. By increasing the potential difference between Q1 and Q2 (i.e., the energy available for CID), an effective decrease in molecular species could be seen without affecting the intensity of the atomic

Pb. In Fig. 2.8, the molecular Pb species, PbOH, $PbNO_3$, and $Pb(NO_3)(H_2O)$ can be seen as the most abundant species with no difference (0 V) between Q1 and Q2. As the potential difference is increased, up to a value of 29 V (the point at which spectral resolution began to be sacrificed), an almost complete reduction the molecular Pb species is seen, illustrating avenues for better-controlled background reductions than the in-source collisional method typically used.

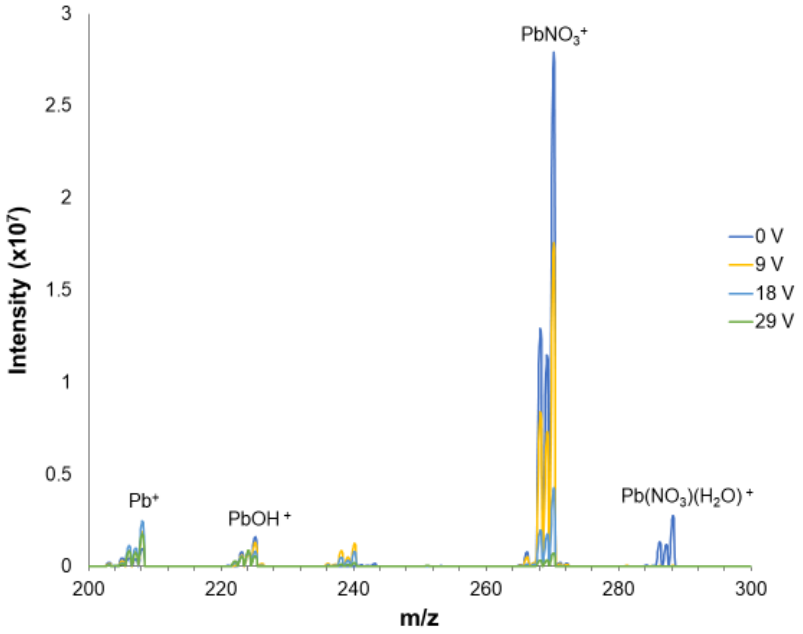

Figure 2.8: Effect of collisional induced dissociation in Q2 on the mass spectra from a 25 µg mL^{-1} Pb solution. Discharge conditions were those presented in Table 2.1.

The CID method of molecular species reduction is not implemented in commercial ICP-MS instruments, focusing instead on using reaction gases to chemically-separate interfering species or to permit the use of kinetic energy discrimination (KED).[42] Unfortunately, one limitation of the present triple-quadrupole platform is that there is not

sufficient pumping capacity to allow Q2 pressurization with helium gas (as used in ICP-MS) nor can the relative Q2/Q3 offset potentials be varied under the system software.

Ultimately the breadth of information that can be obtained can be of great use. As shown above, the elemental species here form a variety of solvent related species. When introducing new species to the plasma, a parent ion scan simplifies the determination of what form the species is taking. Furthermore, this scan may prove useful for speciation studies. The neutral loss scan details a huge number of species formed from solvent adducts. Past works have detailed the formation and reduction of these solvent adducts based on plasma operating conditions, but this system could provide a much more powerful tool in determining the effects of plasma parameters. Lastly, the parent ion scan demonstrates an important capability in the determination of unknown species forming within the plasma. While all of these methods have great benefits for elemental species, they will surely have enormous benefits when combined with the molecular sampling capabilities of the LS-APGD.

2.3.4 Preliminary Limits of Detection and Matrix Effects

Typically, ICP-OES/MS calibration curves are created using multi-element standards, taking advantage of the capabilities of the devices. In an effort to assess the baseline sensitivity of the LS-APGD/TSQ coupling, the MS was operated at the optimized discharge conditions listed in Table 2.1 in a single quadrupole mode, where Q1 was the mass analyzer, utilizing Q2 and Q3 simply as ion guides. In-source CID and Q2 gas pressure were operated to 175 V and 1.5 mTorr, respectively. Triplicate 50 µL injections of the multi-element solution used previously (250 ng mL^{-1} - 250 µg mL^{-1}) were performed

monitoring the analyte responses at the most intense isotope for each. As the concentration exceeded 10 μg mL^{-1}, deviations from linearity occurred. As examples, Fig. 2.9 depicts the isotopic responses as a function of concentration. It can be seen that at 25 μg mL^{-1} of U as $^{238}UO_2^+$ (total metal concentration of 100 μg mL^{-1}), the response of U reaches a maximum and begins to decrease. Rb on the other hand appears to be preferentially ionized over U with a sharp increase intensity beginning at 25 μg mL^{-1}. A similar trend in signal suppression occurs with Ag and Tl although at higher concentrations (50 μg mL^{-1} of Ag and Tl each, with a total metal concentration of 200 μg mL^{-1}). As evidence of potential overloading of the plasma, a single-element U calibration curve was linear (R^2 = 0.9941) from 0.25 – 250 μg mL^{-1}, with severe suppression in response beyond that point. This general set of signal suggests an overloading of the plasma, resulting in inefficient ionization of the higher ionization potential species; clearly a matrix effect that must be considered. That said, total solution concentrations of >100 μg mL^{-1} are above the typical concentration realm of plasma source MS. Certainly, sample dilution under such situations is feasible.

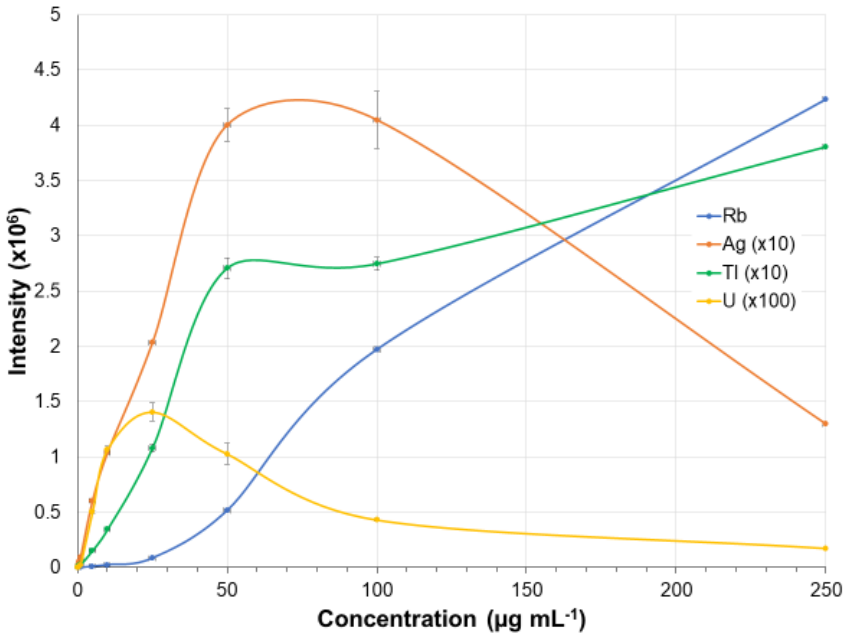

Figure 2.9: Effect of increasing total metal concentrations on analyte response for the multi-element test solution. Discharge conditions were those presented in Table 2.1.

Due to the plasma mass overload effects, calibration curves for the multi-element solution, Table 2.2, were restricted to less than 10 µg mL^{-1} for each of the four elements; a total loading of 40 µg mL^{-1}. Limits of detection were calculated using the following equation

$$LOD = \frac{3\sigma_B}{m}$$

where σ_B is the standard deviation of the blank and m is the slope of the calibration curve and 3 equals a 99% confidence interval. Presented in Table 2.2, the resulting LODs range from 0.99 to 38 ng mL^{-1} which are on par with those previously obtained on the ThermoFisher LCQ Advantage.[30] More importantly for the cases of sample-limited or chromatographic analyses, these concentrations correspond to analyte mass values of 50 – 250 pg. Given the fact that the primary purpose of the interfacing of the LS-APGD

microplasma to this triple-quadrupole is for fundamental plasma diagnostics, it is felt that this level of sensitivity is more than sufficient for that effort.

Table 2.2: Calculated LODs for Rb, Ag, Tl, and U from calibration curves. Concentrations ranging from 250 ng mL^{-1} to 10 µg mL^{-1} were used.

Element	R^2	*LOD (concentration)*	*LOD (absolute mass)*
Rb	0.9939	0.99 ng mL^{-1}	50 pg
Ag	0.9936	4.9 ng mL^{-1}	250 pg
Tl	0.9963	38 ng mL^{-1}	2 ng
U	0.9954	3.5 ng mL^{-1}	180 pg

2.4 Conclusion

The LS-APGD microplasma has been interfaced to a triple-quadrupole platform (ThermoScientific TSQ) providing the capabilities to affect a comprehensive suite of MS/MS modalities. The primary objective was to yield an instrument that provides great flexibility to identify diverse plasma species and provide insights into fundamental processes. A simple multi-element test solution (Rb, Ag, Tl, and U) provided a diversity of analyte-related molecular species. A thorough multi-parametric evaluation of the LS-APGD source operation conditions was performed in this first coupling to a triple quadrupole mass spectrometer. Beyond this, the in-source CID and Q2 gas pressures were optimized to reduce background species leading to significantly improved S/B ratios. In this new instrument coupling, multiple MS/MS scan modes have been explored, illustrating the diversity of information that can be obtained. Parent ion scanning has been utilized to identify the various molecular species which might include the target analyte ions. In

addition, neutral loss scanning was used to identify the presence of oxide, hydroxide, and water cluster species that make up the background spectra. Many of these species are formed via the clustering of water molecules or their addition to analyte ions. Some of these water-related species would have been unidentifiable in previous studies using trapping type instruments due to the limitations of MS/MS modalities. Finally, product ion scanning was employed to illustrate the ability to generically reduce molecular species relative to the target analyte ions. The sensitivity of the instrument was evaluated in a single-quadrupole mode, revealing a clear case of plasma overload above total analyte concentrations of ~100 mg mL^{-1} for 50 µL injections. LODs on the level of sub-to-single ng analyte mass are deemed sufficient for continued fundamental efforts.

Future work in this coupling will look into how plasma conditions, such as electrolyte compositions, affect the different analyte molecular species formed. A more in-depth analysis of the formation of background species will be performed as well. Ultimately, use of a comprehensive triple-quadrupole will permit the expansion of efforts in the use of the LS-APGD microplasma in the realms of organic[32] and organometallic[31] molecular mass spectrometry where MS/MS is essential in structural elucidation.

2.5 Acknowledgements

Reproduced from "Coupling of the liquid sampling – atmospheric pressure glow discharge (LS-APGD) ionization source with a commercial triple quadrupole mass spectrometer," Tyler J. Williams, and R. Kenneth Marcus, 2019 with permission from the Royal Society of Chemistry. This work was supported by the Defense Threat Reduction Agency, Basic Research Award #HDTRA1-14-1-0010, to Clemson University.

2.6 References

1. R. S. Houk, V. A. Fassel, G. D. Flesch, H. J. Svec, A. L. Gray and C. E. Taylor, *Anal. Chem.*, 1980, **52**, 2283-2289.
2. R. S. Houk, *Anal. Chem.*, 1986, **58**, 97A-105A.
3. S. D. Tanner, M. Paul, S. A. Beres and E. R. Denoyer, *At. Spectrosc.*, 1995, **16**, 16-18.
4. N. Jakubowski, L. Moens and F. Vanhaecke, *Spectrochim. Acta, Part B*, 1998, **53**, 1739-1763.
5. D. C. Baxter, I. Rodushkin and E. Engstrom, *J. Anal. At. Spectrom.*, 2012, **27**, 1355-1381.
6. D. W. Koppenaal, C. J. Barinaga and M. R. Smith, *J. Anal. At. Spectrom.*, 1994, **9**, 1053-1058.
7. M. Iglesias, N. Gilon, E. Poussel and J. M. Mermet, *J. Anal. At. Spectrom.*, 2002, **17**, 1240-1247.
8. D. W. Koppenaal, G. C. Eiden and C. J. Barinaga, *J. Anal. At. Spectrom.*, 2004, **19**, 561-570.
9. J. W. Olesik and D. R. Jones, *J. Anal. At. Spectrom.*, 2006, **21**, 141-159.
10. N. Sugiyama and Y. Shikamori, *J. Anal. At. Spectrom.*, 2015, **30**, 2481-2487.
11. E. Bolea-Fernandez, L. Balcaen, M. Resano and F. Vanhaecke, *J. Anal. At. Spectrom*, 2017, **32**, 1660-1679.
12. J. T. Rowan and R. S. Houk, *Appl. Spectrosc.*, 1989, **43**, 976-980.
13. K. L. Busch, G. L. Glish and S. A. McLuckey, *Mass Spectrometry/Mass Spectrometry: Techniques and Applicaitons of Tandem Mass Spectrometry*, VCH, New York, 1988.
14. S. A. McLuckey, *J. Am. Soc. Mass. Spectrom.*, 1992, **3**, 599-614.
15. R. C. A. Machado, C. D. B.; Schiavo, D.; Nobrega, J. A.; Nogueira, A. A., *Microchem. J.*, 2017, **130**, 271-275.
16. J. A. V. A. Barros, A. Virgilio, D. Schiavo and J. A. Nobrega, *Microchem. J.*, 2017, **133**, 567-571.
17. L. Fu, S. Y. Shi and X. Q. Chen, *Spectrochim. Acta, Part B*, 2017, **133**, 34-39.
18. R. Thomas, *Practical Guide to ICP-MS*, CRC Press, Boca Raton, Fl, 2013.
19. E. D. Hoegg, B. A. Patel, D. D. Richardson and R. K. Marcus, *J. Anal. At. Spectrom.*, 2018, **33**, 2015-2020.
20. P. Mezei and T. Cserfalvi, *Appl. Spectrosc. Rev.* , 2007, **42**, 573-604.
21. Z. Z. Q. He and S. Hu, *Appl. Spectrosc. Rev.*, 2013, **49**, 249-269.
22. P. Jamroz, K. Greda and P. Pohl, *TrAC- Tr. Anal. Chem.*, 2012, **41**, 105-121.
23. T. Cserfalvi and P. Mezei, *Fresenius' J. Anal. Chem.*, 1996, **355**, 813-819.
24. T. Cserfalvi and P. Mezei, *J. Anal. At. Spectrom.*, 1994, **9**, 345-349.
25. T. Cserfalvi, P. Mezei and P. Apai, *J. Phys. D. Appl. Phys.*, 1993, **26**, 2184-2188.
26. M. R. Webb, G. C. Y. Chan, F. J. Andrade, G. Gamez and G. M. Hieftje, *J. Anal. At. Spectrom.*, 2006, **21**, 525-530.
27. R. K. Marcus, B. T. Manard and C. D. Quarles, *J. Anal. At. Spectrom.*, 2017, **32**, 704-716.

28. W. C. Davis and R. K. Marcus, *J. Anal. At. Spectrom.*, 2001, **16**, 931-937.
29. R. K. Marcus, C. D. Quarles, C. J. Barinaga, A. J. Carado and D. W. Koppenaal, *Anal. Chem.*, 2011, **83**, 2425-2429.
30. L. X. Zhang, B. T. Manard, S. Konegger-Kappel and R. K. Marcus, *Anal. Bioanal. Chem.*, 2014, **406**, 7741-7741.
31. L. X. Zhang, B. T. Manard, B. A. Powell and R. K. Marcus, *Anal. Chem.*, 2015, **87**, 7218-7225.
32. L. X. Zhang and R. K. Marcus, *J. Anal. At. Spectrom.*, 2016, **31**, 145-151.
33. E. D. Hoegg, R. K. Marcus, D. W. Koppenaal, J. Irvahn, G. J. Hager and G. L. Hart, *Rapid Commun Mass Sp*, 2017, **31**, 1534-1540.
34. E. D. M. Hoegg, R. K.; Hager, G. J.; Hart, G. L.; Koppenaal, D. W., *J. Anal. At. Spectrom.*, 2018.
35. E. D. Hoegg, C. J. Barinaga, G. J. Hager, G. L. Hart, D. W. Koppenaal and R. K. Marcus, *J. Am. Soc. Mass. Spectrom.*, 2016, **27**, 1393-1403.
36. E. D. Hoegg, C. J. Barinaga, G. J. Hager, G. L. Hart, D. W. Koppenaal and R. K. Marcus, *J. Anal. At. Spectrom.*, 2016, **31**, 2355-2362.
37. C. D. Quarles, A. J. Carado, C. J. Barinaga, D. W. Koppenaal and R. K. Marcus, *Anal Bioanal Chem*, 2012, **402**, 261-268.
38. E. D. Hoegg, B. A. Patel, W. N. Napoli, D. D. Richardson and R. K. Marcus, *J. Anal. At. Spectrom.*, 2018, **33**, 2015-2020.
39. M. C. A. Bevilacqua, and M. Sinigaglia, *Microbiology Book Series*, Formatex Research Center, 2010.
40. N. I. Rousis, L. N. Pasias and N. S. Thomaidis, *Anal. Methods*, 2014, **6**, 5899-5908.
41. Q. S. Ran, R. W. Schmude, K. A. Gingerich, D. W. Wilhite and J. E. Kingcade, *J. Phys. Chem.*, 1993, **97**, 8535-8540.
42. N. Yamada, *Spectrochim. Acta, Part B*, 2015, **110**, 31-44.

CHAPTER III

COUPLING THE LIQUID SAMPLING – ATMOSPHERIC PRESSURE GLOW DISCHARGE, A COMBINED ATOMIC AND MOLECULAR (CAM) IONIZATION SOURCE, TO A REDUCED-FORMAT MASS SPECTROMETER FOR ANALYSIS OF DIVERSE SPECIES

3.1 Introduction

The field of analytical atomic spectrometry commonly employs inductively coupled plasma (ICP) spectrochemical sources due to their unrivaled sensitivity, robustness, and tolerance to various matrices. ICP-MS in particular, provides detection limits approaching fg mL^{-1} for many elements as well readily-interpreted mass spectra.[1-3] Although the present benefits of this method are immense, a major challenge had been the presence of spectral interferents preventing the analysis of certain ions. For example, argide species such as Ar_2^+ interfere with the measurement of ^{80}Se or ArH^+ interferes with the measurement of ^{41}K.[4] A variety of methodologies have been developed to overcome these issues, including cool plasma conditions, high resolution instrumentation, and most notably collision-reaction cells.[4-9] The result is an instrument portfolio with a vast number of methodologies capable of determining nearly every element. Commercial ICP-MS instruments have become more widely available and developments in their technologies have improved their ease of use and sample throughput.[1] Despite these improvements, ICP-MS suffers from high capital costs and high consumable use, leading to appreciable overhead costs. Beyond the high-power requirements of these instruments, they generally require 15 – 20 L min^{-1} of Ar gas to maintain the plasma as well as any specialty gases that may be required for now-common collision/reaction cells. Beyond these requirements,

appreciable sample volumes are required as a result of the ~0.4 mL min^{-1} sample introduction rates.[1] This combination of factors limits the potential scenarios in which current commercial ICP-MS instruments can be implemented to well controlled analytical laboratories.

Miniaturization of analytical instrumentation has evolved over the past few decades with specific focus on the reduction of sample volumes, operational overhead, and instrument footprint.[10-12] Mass spectrometry has been of particular interest regarding miniaturized instrumentation, due to its capabilities in high sensitivity and high selectivity analysis. Ouyang, Cooks, and co-workers have presented comprehensive reviews on the topic.[13, 14] Advances in mass analyzer technologies have led to a dramatic reduction in their size, lowering the volume of the vacuum chamber and the total vacuum pumping requirements, allowing a large reduction in instrument size. These improvements, however, are not without their drawbacks, as these instruments tend to come with compromises in both sensitivity and resolution. It has been stated that the most important requirement for a miniaturized mass spectrometer is *adequate performance*, meaning it should maintain at least unit mass resolution and sensitivity that is relevant to the application at hand.[13, 14] Another, perhaps more subtle, aspect in the format downsizing is reduced pumping capacities and the requisite limitation as to the types of ion sources that can be effectively sampled. Up to this point, miniaturized instruments typically rely on trap-based mass analyzers, including rectilinear ion traps or 3D ion traps, though miniaturized quadrupoles are long-known. Based on the lower sampling overhead requirements and primary need for determinations of "molecular" species in field-based and "point-of" analysis applications,

the vast majority of such systems have employed sources such as direct analysis in real time (DART) and paper spray ionization as well as the continued use of electrospray ionization (ESI) under ambient condition and electron ionization (EI) of gases *in vacuo*. To date, no systems have been demonstrated towards what would be termed elemental or atomic mass spectrometry.

To be clear, there is a great expanse in the need and requirements for reduced-format MS systems and miniaturized ones designed for field-deployment or point-of-care situations. Systems of smaller footprint, low operational overhead, and perhaps greater analytical flexibility could have impact in diverse arenas including within-in the chemistry or biochemistry laboratory, at-reactor process monitoring, and indeed situations where transportable or remotely-fixed sampling/monitoring is required. Here again, current instruments applicable in these sorts of application environments generally fall into the realm of organic/molecular mass spectrometry. While the footprint of today's quadrupole-based ICP-MS systems is much reduced in comparison to first-generation instruments,[3, 15, 16] the plasma operating at 1-2 kW of power, at temperatures of perhaps 10,000 K, and gas flow rates upwards of 15 L min^{-1} of argon are simply prohibitive towards that middle-ground of implementation. To this end, miniaturized plasmas, potentially compatible with reduced-format mass analyzers, are of interest.

A recent focus in the atomic spectroscopy field has been the development of atmospheric pressure glow discharge (APGD) ionization sources due to their reduced format, low power, and low consumable use. First introduced as excitation sources for optical emission spectroscopy (OES), numerous reviews have detailed the potential of

these devices.[17-19] One family of devices, first introduced by Cserfalvi et al., was termed the electrolyte cathode glow discharge (ELCAD).[20-22] This design was further improved upon by Hieftje et al. as the solution cathode glow discharge (SCGD), which has been applied in OES and MS modalities.[23, 24] Of a different design, the liquid sampling-atmospheric pressure glow discharge (LS-APGD) is a microplasma ionization source developed by Marcus et al. that has been found to have a number of desirable features relative to other miniaturized plasma sources.[25] The LS-APGD operates in a total consumption mode with solution flow rates of less than 50 µL min^{-1}, powers of <50 W, and a 0.5 L min^{-1} He flow rate. Developed initially as an OES source, MS sampling has demonstrated applicability in elemental,[26, 27] isotopic,[28-30] and molecular species analysis.[31-33] This diversity in information provided and modalities of operation is referred to as combined atomic and molecular (CAM) ionization. Fortuitously, the microplasma can be mated directly with any instrument having the atmospheric pressure interfaces typical of ESI and other ambient sampling mass spectrometers common to organic MS. All of these features bode well for potential implementation on mass analyzers of reduced-format, while also providing a diversity in the types of analyses that can be affected; elemental/isotopic/molecular.

To this point the LS-APGD has been coupled with a large variety of mass spectrometers including orbitraps,[26, 33, 34] Paul traps,[27] and triple quadrupoles.[35] More recently the LS-APGD has been coupled to a reduced-format mass spectrometer, the Waters QDa, to analyze trace metals in Chinese hamster ovary (CHO) cell media.[36] This interfacing was explicitly directed at affecting at-bioreactor elemental determinations on a

platform amenable for the production environment. This was the first example of a miniaturized system capable of analyzing elemental samples, as the microplasma was used in place of the normal ESI source without any other modifications, though this pairing was not without its operational challenges.[36]

Continued interest in a reduced-format mass analyzer with a CAM ionization source has led to the investigation of alternatives. Presented here is the coupling of the LS-APGD with an Advion (Ithaca, NY) Expression^{L} Compact Mass Spectrometer (CMS). As in the previous instruments used, this instrument comes standard with ESI and APCI sources. This system however was designed with a reduced-format platform, ideal for space- and utility-limited locations. Pairing the LS-APGD with this instrument, presents a truly reduced-format atomic mass spectrometer; weighing just 32 kg and having a footprint of 66 x 28 x 56 cm. Additionally, the CMS has been previously travel hardened in accordance with MIL-STD-810. A top-to-bottom design approach was undertaken to mount the microplasma source and its utility inputs within the standard source housing of the CMS instrument. Additionally, an integrated utility housing and control box was designed and implemented, with all operations set and monitored through a touch-pad screen. In order to optimize the pairing between the two, the ion optic variables were evaluated in order to maximize ion throughput. As done with previous works, a thorough multi-parametric evaluation of the plasma was completed to optimize both the signal intensity and the signal-to-background ratios for Na, Rb, Cs, and Tl. With optimized plasma parameters, a variety of analytes were evaluated looking at their analytical performance. To complement the optimization relative to elemental MS, a preliminary

evaluation of this pairing's suitability towards molecular analyte species was performed for a variety of common drugs. Ultimately, this combination suggests capabilities as a reduced-format, CAM system capable of diverse sample analyses that is suitable for implementation in diverse areas of application.

3.2 Experimental

3.2.1 Source Design

The components of the LS-APGD, as are relevant to mass spectrometry, have been described previously and can be seen in Fig. 3.1a along with the basic components of the Advion CMS mass spectrometer system.[26, 27, 34] The inner capillary has been changed from a stainless-steel form with a deactivated silica stationary phase, to a fused silica capillary (280 µm i.d., 580 µm o.d.). The electrolytic solution (sample) is introduced through the inner capillary (20-60 µL min^{-1}; Molex; Lisle, IL) which is housed within a grounded stainless-steel outer capillary (316 SS, 0.8 mm i.d., 1.6 mm o.d.; McMaster-Carr; Elmhurst, IL) through which a cooling He sheath gas (0.4-1 L min^{-1}) is introduced. The anode is a solid metal electrode (SS weldable feedthrough; MDC Vacuum Products, LLC; Hayward, CA) which has a positive potential applied via a high voltage power supply. The components of the ion source integrated into an Advion source housing are shown in the picture of Fig. 3.1b. The liquid flow, gas flow, and discharge current are maintained and controlled through a custom designed control box (GAA Custom Electronics; Kennewick, WA). Outputs of the control box are carried to the source housing within a single umbilical cord assembly. The source was mounted inside a standard Advion ion source housing to interface to the instrument. The LS-APGD directly replaces the ESI source, with the only

modification to the system being the implementation of a turbomolecular pump (Edwards; Burgess Hill, England) optimized for the pumping of the He sheath gas load. The complete pairing of the LS-APGD and CMS can be seen in Fig. 3.1c. Additional photographs of the source housing, the electrode assembly, and the controller system can be seen in Electronic Supplementary Information.

a.

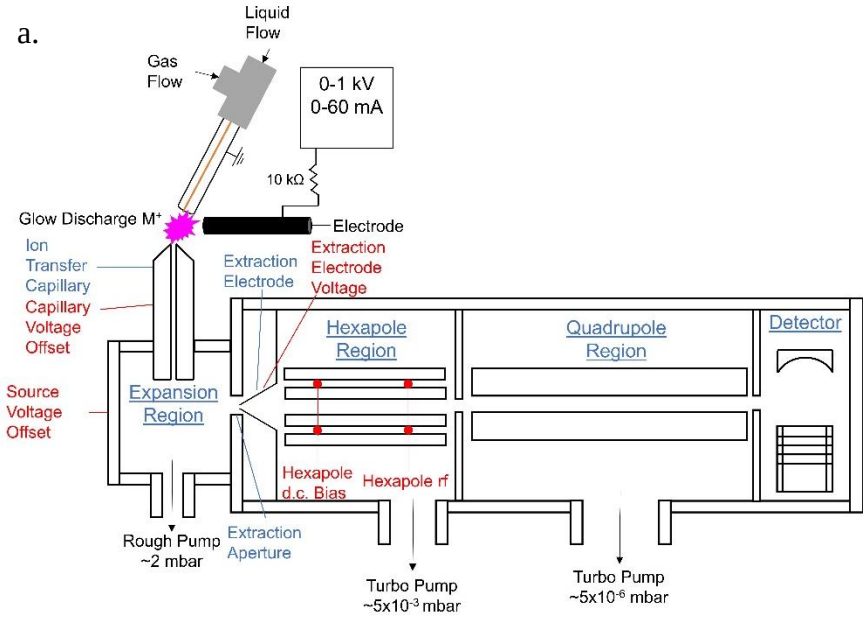

b.

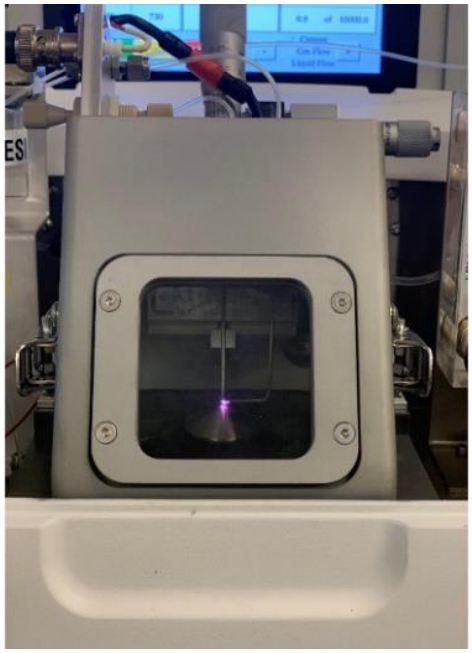

c.

Figure 3.1: Diagrammatic representation of the a) the LS-APGD ionization source interfaced with the Advion Expression^{L} CMS, b) a picture of the LS-APGD interfaced within the Advion source housing and c) a picture of the entire LS-APGD system interfaced with the CMS.

3.2.2 Mass Spectrometer System

In this work, the LS-APGD was interfaced to a standard Advion (Ithaca, NY) Expression^{L} Compact Mass Spectrometer. As depicted in Fig. 3.1a, the major components of the CMS system consist of an ion transfer capillary, ion optics, quadrupole mass analyzer and an electron multiplier detector with a conversion dynode. Different from many systems, after exiting the ion transfer capillary, ions and neutrals enter an expansion region where the ions are repelled (nominally 90º) towards the mass analyzer by a potential (source voltage offset) while neutrals, unaffected by the potential, continue towards the entrance of the first-stage roughing pump. In addition to directing the ion population, this potential also serves to accelerate ions, somewhat affecting ion collisions with background gases in this intermediate pressure region. The extraction electrode, placed in the interface

between the expansion region and the hexapole region, acts to transport ions between the two areas. A positive potential (extraction electrode voltage) is applied to the extraction electrode which acts to slow the ion population as it approaches the interface, where it is then pulled into the hexapole region due to the pressure differential. The potential placed on the extraction electrode, slowing the ion population, is set more negative relative to the source voltage to help direct the ion population into the hexapole region. A hexapole assembly is employed to facilitate collisional cooling and focusing prior to entering the quadrupole. Acting in an rf-only mode, a hexapole d.c. bias is applied to enable transport of the ions, with the hexapole rf offset and scan value applied to determine which ions may be passed. As heavier ions require a larger rf value for transmission, the hexapole rf is ramped as a function of mass. In the cases of ion optic optimization, data was obtained using a full scan mode at a scan rate of 500 ms for a mass range of 10-250 m/z, while the data for source optimization and quantitative analysis was collected using selected ion monitoring (SIM) with a mass window of 0.3 Da about the target mass and a dwell time of 50 ms.

3.2.3 Sample Preparation

Three different stock solutions (two elemental and one of organics) were used in this work, one for the optimization of the ion optics and a second for the optimization of the source parameters and mass calibration of the instrument. The first solution, used for ion optic optimization, was prepared by diluting Rb and Ag elemental standards (High Purity Standards; Charleston, SC) and dissolving a Tl nitrate salt (Beantown Chemical; Hudson, NH) in 2% HNO_3 to prepare a 10 μg mL^{-1} solution. The second solution, used for

the source optimization, included Na, Rb, Cs, and Tl at 10 µg mL^{-1}, (Na, SPEX CertiPrep, Metuchen, NJ; Cs; Ricca Chemical Company; Arlington, TX) to cover a broader mass range and to mass-calibrate the instrument, and was prepared in the same manner. Response curve solutions were prepared through the serial dilution of the second solution. For the third solution, caffeine, acetaminophen, caffeine, sulfadimethoxine, terfenadine, and reserpine were obtained from Sigma Aldrich (St. Louis MO) and Δ^9-Tetrahydrocannabidiol (Δ^9-THC) was obtained from Cayman Chemical Company (Ann Arbor, MI). Samples were dissolved in 70:30 methanol (Fisher Scientific; Waltham, MA):water at 10 µg mL^{-1}, each. Calibration standards were prepared by serial dilution of the stock solution.

3.3 Results and Discussion

3.3.1 Optimization of Ion Throughput

In prior couplings of the LS-APGD with various mass spectrometers,[26, 27, 35] no appreciable changes to the ion optic settings were required from those used for the standard ESI sources to obtain a response from the microplasma source. Upon initial coupling to the CMS, at the standard ESI ion optic settings, no analyte signal was observed. The lack of analyte signal can be largely attributed to the way the instrument is designed to sample ions generated in the ion source, the components of which are shown in Fig. 3.1a. Sheath gas and ions generated in the source are transported from atmospheric pressure into the first low pressure (~200 Pa) region of the mass spectrometer through an ion transfer capillary (ITC). Upon exiting the ITC, gases and ions enter into an expansion zone and continue their expansion until they reach a turbulent (Mach disk) region. In this region, the gas

velocity, and subsequently the ion velocity is reduced, and it is at this point that an extraction electrode is placed. An electrostatic field is established across the pathway of the mixture of sheath gas and ions, between the source housing and the extraction electrode to draw ions towards the extraction electrode where they are pulled into the next vacuum stage.[37] Through this process, there are three potentials which can be altered by the user: the capillary voltage, an accelerating potential placed on the ITC; the source voltage, applied on the housing of the transfer region, driving ions towards the extraction electrode; and the extraction electrode voltage, set relative to the source voltage to assist in pulling ions out of the gas stream and pulling them towards the next vacuum region. These potentials largely influenced the efficient transport of ions from the LS-APGD to the MS, with the difference in gas identity between the ESI and microplasma sources (N_2 vs He) driving the discrepancies between ion optic settings. While the gas and ion mixture that exits the ITC is at supersonic speed regardless of the gas identity, work by Anderson and Fenn suggests that the identity of gas exiting a nozzle may influence the distribution of analyte across the gas expansion region.[38, 39] In fact, when a higher fraction of a lighter molecular weight gas is utilized, the degree of distribution increased. Because the LS-APGD utilizes He, a larger ion distribution, or change in the location of the turbulent region, influences the optimal transmission of ions into the hexapole region. Shown in Fig 3.2, analyte signal intensity increases as a function of capillary voltage, which acts as an accelerating potential, to a maximum of value 180 V, the maximum allowed by the instrument. The capillary voltage appears to be acting in a compensatory manner, further moving ions into a region where they can be more effectively extracted into the hexapole

region. In comparison, the standard ESI setting for the capillary voltage is only 120 V, reflective of the heavier gas matrix.

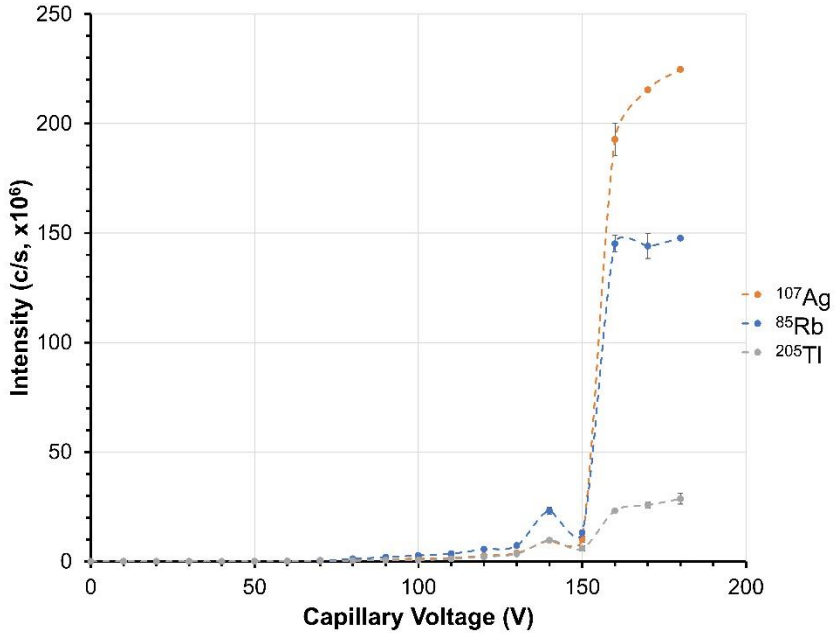

Figure 3.2: Effect of capillary voltage on the analyte signal response. This voltage acts as an accelerating potential for ions entering the mass spectrometer. Analyte concentration was 10 µg mL^{-1} of each element.

As gas and ions enter the expansion region, an electrostatic field is generated between the source housing of the expansion region and the extraction electrode to assist in drawing ions towards the hexapole region. The influence of the voltage placed on the source housing (the source voltage) and on the extraction electrode were evaluated. The source voltage effectively pushes ions towards the extraction electrode, as such too low of a voltage results in a poor analyte response due to ineffective deflection of ions towards the extraction electrode. Too high of a potential, however, may result in ions making the turn too early, or result in collisional scattering, both leading to inefficient transmission. As seen in Fig. 3.3, an optimum voltage for the analyte transmission was observed at ~40

V. This value is similar to what is typically used for an ESI source, though in that case an increasing voltage ramp (up to ~70 V) is employed as the mass of the analyte ions increases. In the cases where analysis of lower-mass elemental species is of interest, it was determined that a voltage ramp was unnecessary.

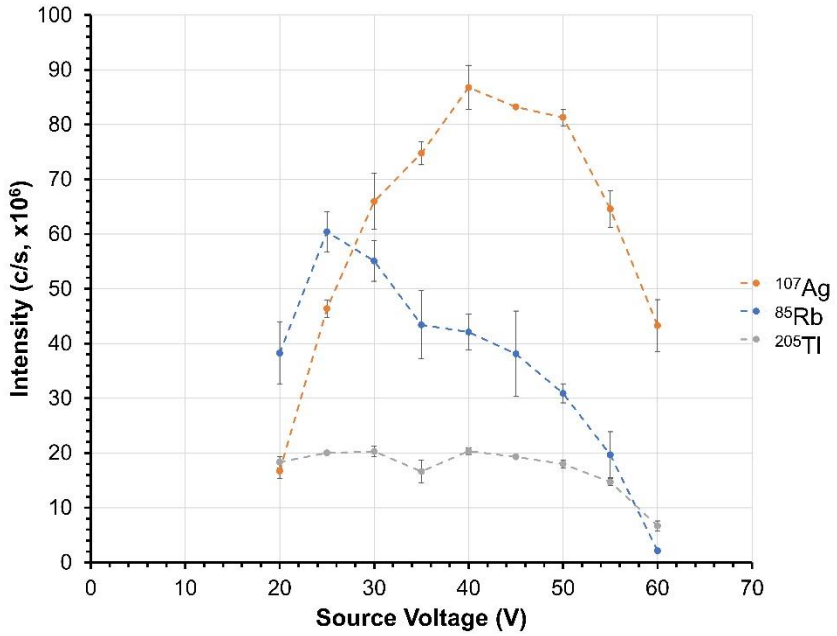

Figure 3.3: Effect of source voltage on analyte signal response. This voltage affects both ion transmission and collisional dissociation. Analyte concentration was 10 µg mL^{-1} of each element.

The extraction electrode voltage complements that of the source housing, so that ions are directed towards the extraction electrode. As such, a more negative potential is applied to that element, though with a small potential difference so as to not introduce ions into the hexapole region with too-high of kinetic energy. In general, the analytes show fairly uniform response as a function of potential, with a slight optimum at ~8V. Here again, the potential employed here is similar to that used for ESI. Ultimately, this potential serves little more than to establish a field gradient between the source housing and the

extraction electrode, the latter of which clearly has a larger influence on ion throughput. In whole, the greatest difference ion optics potential between the standard ESI/APCI sources and the CAM microplasma are in the capillary voltage stage, where the differences are readily attributed to the sheath gases used in the source types.

The last two ion optic parameters that were evaluated were the hexapole d.c. bias and the hexapole rf offset, Figs. 3.4a and b. The hexapole in this instrument is acting merely as an ion guide and is therefore running in an rf only mode. The hexapole d.c. bias is a static potential applied to the hexapole in order to transport ions through it. As seen in Fig 3.4a, the analyte response reached a maximum at a hexapole bias of about 6.5 V. Although a maximum for Tl was observed at 5.2 V, its signal to background ratio was 2x greater at 6.5 V, and this coupled with the higher Ag response warranted the choice of the higher potential. In fact, the response is very similar to that of the ion extraction lens in terms of the extent of the effects and the absolute potentials, which is not surprising as the kinetic energy of the ions must be matched throughout the hexapole transport.

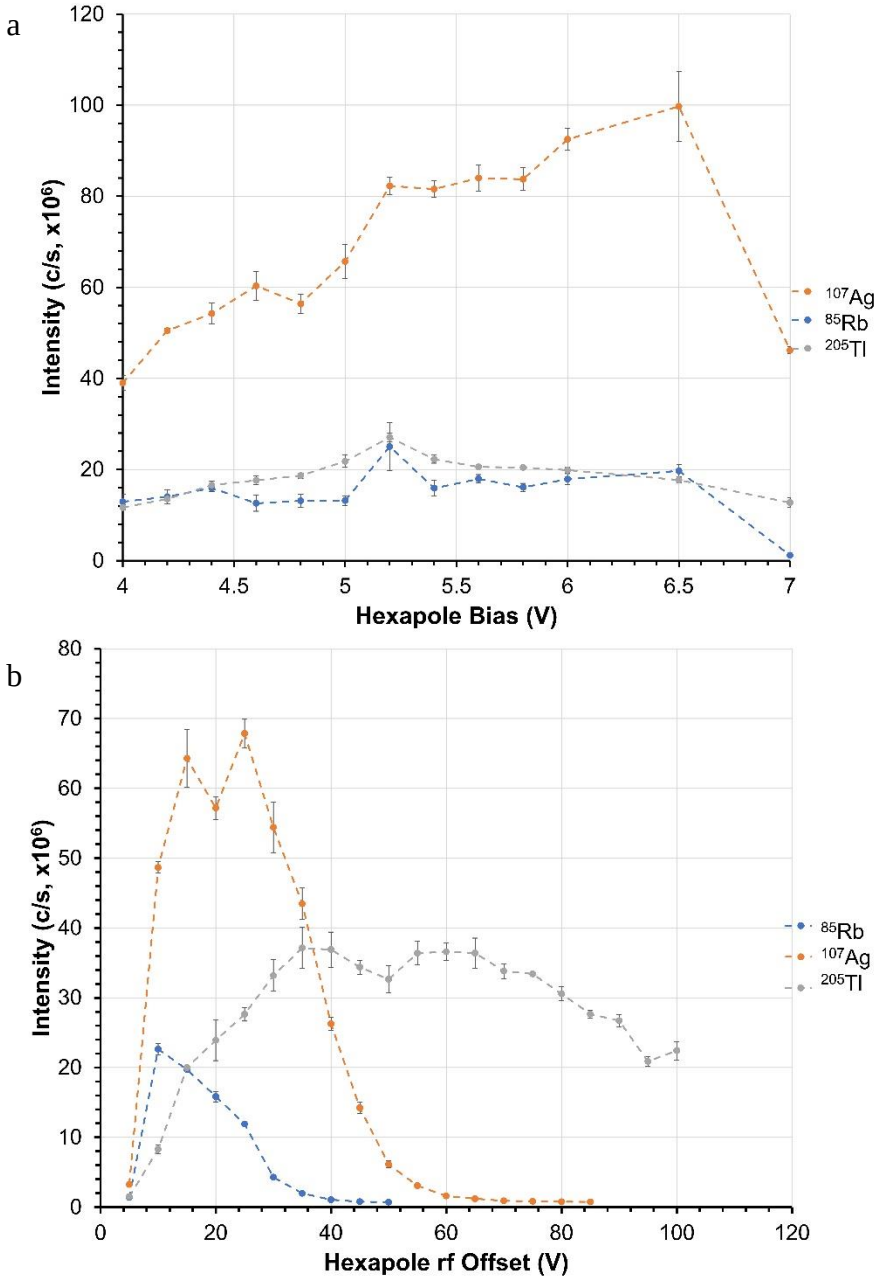

Figure 3.4: Effect of a) hexapole d.c. bias and b) hexapole rf offset setting on analyte intensity. Different set points facilitated the transmission of different ions and an rf scan value was used to compensate for this effect. Analyte concentration was 10 µg mL^{-1} of each element.

Of more significance to optimize sampling, were the hexapole rf offset and ramp values. Ions are only transmitted through the hexapole if the applied rf potential is sufficient

to allow their transmission. Because the required rf value is proportional to mass, an rf ramp is employed to ensure ions of all masses are effectively transmitted. The setting of the ramp value is where the instrument will set the max rf value to at the high mass of the instrument (2000 Da). For example, if the rf value is 0 V and the ramp value is 250 V, then the rf value at the lowest mass, 10 Da, will be 0 V and it will ramp up to 250 V at 2000 Da, regardless of what the mass range is set to. This, provides a challenge for lower mass species which require lower rf values, as seen in Fig. 3.4b. Not only do these analytes require a relatively low rf value for efficient transmission, but they have different optimum points, so that an rf volt ramp is required. Unfortunately, the maximum ramp value that can be used is 250 V, which means the hexapole rf value across this mass range varies from only 0 – 25 V; too low for optimum transmission across this entire mass range.

3.3.2 Parametric Evaluation and Coupling Characteristics of the LS-APGD

With the transmission of ions from the source and through the instrument evaluated, the influence of source parameters was explored. Previous couplings with the Paul trap, Orbitrap, and triple quadrupole instruments have explored the dependencies of the signal intensity, S/B ratio, and isotope ratio precision and accuracy on the ion source parameters. The operating parameters investigated have included the discharge current, solution flow rate, sheath gas flow rate, sampling distance, and the interelectrode distance.[27, 34, 35] While many parameterizations have been completed on the LS-APGD, there are a number of differences with regards to the CMS interfacing that warrant re-evaluation. The most significant difference is the angle at which the microplasma is mounted relative to MS entrance aperture. In all other works, the solution electrode of the LS-APGD was placed

in-line with the mass spectrometer inlet,[27, 35, 36, 40] whereas in this interface an approximately 25º angle is used, which is the same used for the ESI. In addition, the integration of a fused silica capillary allows for operation at higher currents than previous LS-APGD works.

The various discharge parameters were evaluated via a design of experiment (DoE) approach. This method models the response of various dependent variables based on changing a number of independent variables. The independent variables, in this case, were the source parameters listed in Table 3.1, and the dependent variables were the analyte signal intensity and the measured S/B ratio. The range of parameters used reflected recent MS works, allowing for comparison across platforms.[27, 34, 35, 40] A test matrix was generated using the JMP software (JMP Pro; Cary, NY) in order to probe the parametric effects as well as any inter-parametric effects that may be occurring. For each parameter, a significance level is determined, and, considering the responses for all analytes in the test mix simultaneously, the software will determine optimum conditions for each parameter.

Table 3.1: Ranges of DoE-evaluated LS-APGD operating conditions and their final optimized values.

Parameter	*Testing Range*	*Optimized Setting*
Gas Flow Rate	0.2 – 1 L min^{-1}	0.5 L min^{-1}
Liquid Flow Rate	20 – 60 µL min^{-1}	50 µL min^{-1}
Discharge Current	20 – 60 mA	50 mA
Electrode Gap	0.5 – 2 mm	1 mm
Sampling Distance	0.5 – 3.5	0.5 mm

In this evaluation, the analyte species monitored included Na, Rb, Cs, and Tl. These analytes were chosen as they covered a wide mass range and the high abundance isotopes of each element allow for simple mass calibration of the instrument using this solution. Figures 3.5a and b detail the effects of each parameter, as well as inter-parametric effects, on the a) analyte response and the b) S/B respectively. These so-called Pareto plots include a dashed vertical line at a LogWorth value of 2.0, indicative of a threshold to which the effect of the parameter is considered to be statistically significant at the 99% level. In Fig 3.5a, the only parameter that has a significant influence on the analyte response is the gas flow rate. Seen in previous work with quadrupole instruments, too high of a gas flow rate would disable instrument electronics due to raising the pressure in the vacuum chamber.[35] With this instrument, while no interlocks were activated, the internal pressure of the instrument was observed to increase at higher gas flow rates, as such collisional losses in the first stage of the vacuum system lead to reduced ion transmission and signal losses. While the other parameters do not affect the analyte signal intensity at the 99% confidence, they do still have some influence over the plasma and require consideration, as LogWorth values of >1.3 are at the 95% level. For example, increasing the electrode gap results in increasing the residence time of analyte within the plasma and thus increased responses. As a counter-effect, displacing the electrodes, however, may pull the active region (negative glow) of the plasma slightly outside of the sampling "sweet spot" of the instrument. Additionally, with the discharge current, a higher current results in a higher power density plasma providing increased responses, here higher currents were available as the current fused silica inner capillary was not prone to decomposition as in the past.[35]

Capillary heating can be offset with higher sheath gas flows, to a point as noted above. Excess heating of the capillaries can lead to the desolvation of analyte species within the inner liquid-carrying capillary, resulting poor sample introduction into the plasma. Lastly, described in previous work, an increase in the sampling distance typically results in lower signal intensities as a result of additional ion losses on the sampling cone of the instrument.[35] While there are a number of inter-parametric effects that were looked at, none proved to be statistically significant (99 %) regarding signal intensity. While a few do approach the 95% significance (LogWorth of 1.3), they all include gas flow rate, and are likely dominated by its largely significant effect.

a.

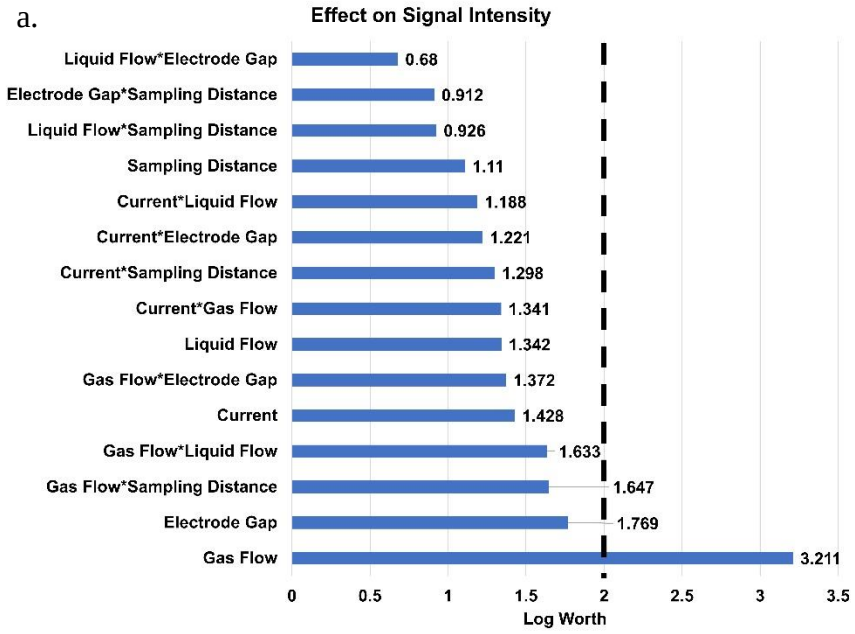

b.

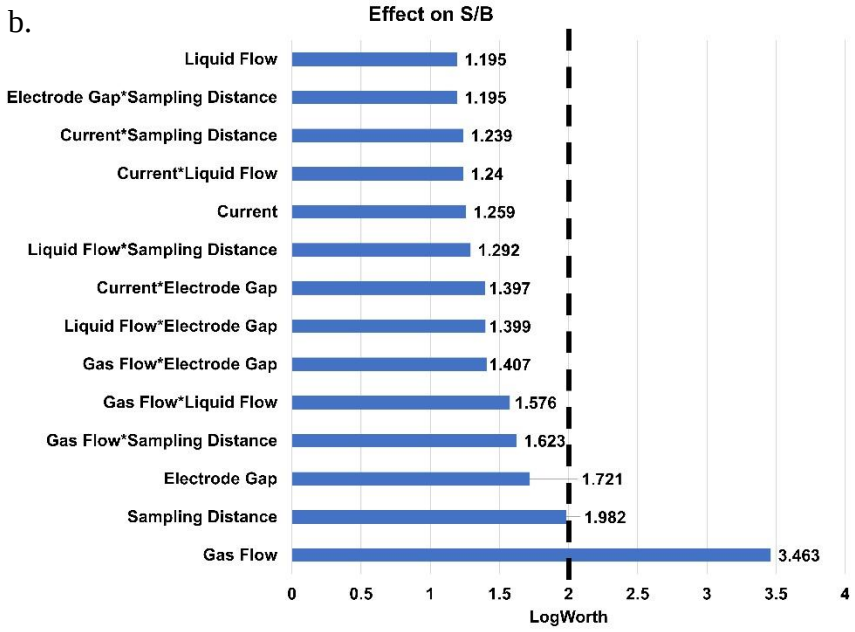

Figure 3.5: Bar graph reflecting the combined significance of each operating parameter and cross effects on the a) analyte signal intensities and b) analyte signal-to-background ratios. Analyte concentration was 10 µg mL^{-1} of each element.

Figure 3.5b depicts the effects of the plasma parameters on the S/B of the analytes. Again, this graph shows the significant effects of gas flow rate, wherein the higher gas flow rates result in a raised pressure within the mass spectrometer leading to reduced analytical performance. Similar to signal intensity, no other parameters or inter-parametric effects have a statistically significant influence although a couple do approach significance. Sampling distance for instance, has much greater significance on the S/B than on signal intensity. As described above, improved sampling has been observed as the plasma is moved closer to the entrance to the mass spectrometer, and although this will lead to increased background as well, the improvements in analyte sampling are much greater than the background. Additionally, the electrode gap, which increases residence time within the plasma with increasing electrode displacement, approaches significance for both S and S/B.

This is expected as increasing the residence time of the analyte in the plasma should improve ionization efficiency, while facilitating additional desolvation resulting in a decrease in potential molecular interferents. The majority of the inter-parametric effects and other parameters tend to follow similar trends for both signal intensity and S/B ratio, suggesting the sources of both S and B are the same. The final DoE-optimized operating conditions are presented in Table 3.1 and these conditions were used in the rest of this work. As a point of reference, Fig. 3.6 is a mass spectrum of the 10 μg mL^{-1} Na, Rb, Cs, and Tl test mixture on the CMS platform under the optimized plasma and MS sampling conditions. The spectrum is composed almost exclusively of the signals from the test elements, background solvent-related species being virtually non-existent on the scale of these analytes present on the 10 μg mL^{-1} level. That said, there is a clear bias against the Na analyte. This is likely due to the design and operation aspects of the CMS quadrupole mass analyzer, which is tailored for masses more appropriate for molecular species analysis; effectively de-tuned for Na at m/z = 23. Although the ion optics have been tuned to allow better low mass throughput, the potentials applied to the quadrupole itself are still designed towards the analysis of a large mass range, resulting in poor throughput at the low end of the range. This can be seen in Fig. 3.6 by the fronting seen on each peak, as the mass range being used represents the bottom 10% of the mass range this instrument can measure. The poor peak shape (fronting) of the Na signal, versus the other analytes, supports this hypothesis.

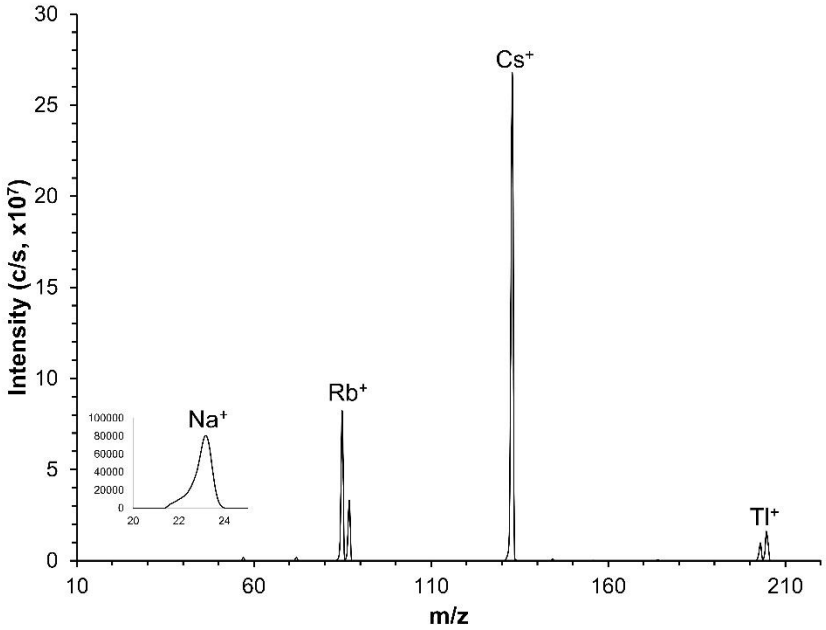

Figure 3.6: LS-APGD mass spectrum of the 10 μg mL^{-1} Na, Rb, Cs, and Tl test mixture in 2% HNO_3 on the CMS platform under the optimized plasma and MS sampling conditions. 20 μL injection volume.

3.3.3 Preliminary Figures of Merit

In an effort to assess the analytical figures of merit of this pairing, the LS-APGD/CMS was operated under optimized ion optic and source parameters and response curves (100 ng mL^{-1} – 10 μg mL^{-1}) were constructed. The analyte species (Na, Rb, Cs, and Tl) were monitored using selected ion monitoring (SIM). Table 3.2 reports the regression equations and statistics, the calculated limits of detection and the respective signal-to-noise (S/N) and precision (n=3) for triplicate injections of the analyte mixture at 500 ng mL^{-1} for each element. The limits of detection were calculated using the following equation

$$LOD = \frac{k\sigma_B}{m}$$

where σ_B is the standard deviation of the blank, m is the slope of the calibration curve and the constant (k=3) represents the 99% confidence interval. The respective sensitivities (m)

for the elements fall within a factor-of-3 except in the case of Na. The resulting LODs, in the range of low 10's of ng mL^{-1} are certainly sufficient for many applications. One could certainly argue that the LODs here are more comparable to ICP-OES, but in the context of using 20 μL sample injections and the fact that the operational overhead of even the optical version of the ICP is a burden, the present platform is still more suitable for many determinations, while retaining the key quantitative aspects of use of elemental isotopes for identification and quantification. Indeed, the mass-based LODs ranging from 0.4 – 3 ng are more in line with standard ICP-MS instruments on an absolute scale, which is critical for many cases of volume-limited sample analyses.

Table 3.2: Analytical figures of merit for target elements. Response curve concentrations ranging from 100 – 10,000 ng mL^{-1} for 20 μL, triplicate injections.

Element	*Equation*	R^2	*LOD (ng mL^{-1})*	*LOD (absolute, ng)*	*S/N @ 500 ng mL^{-1}*	*%RSD @ 500 ng mL^{-1}*
Na	y=12.053x+1694.08	0.9687	146	3	5	12.2
Rb	y=1466x+25839	0.9941	28	0.5	19	1.5
Cs	y=4285x+50175	0.9953	18	0.4	17	0.5
Tl	y=1561.8x+9940	0.9891	20	0.4	53	1.5

3.3.4 Analysis of Representative Drug Molecules

While the LS-APGD has a legacy in elemental and isotope ratio analysis, it also has the ability to obtain molecular information acting as a CAM ionization source.[27,34] This sort of capability on a reduced-format platform is as equally relevant to applications such as the chemical synthesis laboratory where there may be instances where both elemental and small molecule analyses may be required. The alternative approach would be to have

access to standard ICP and ESI/APCI instrumentation. The ability to affect both sorts of analyses on a single platform would bring a versatility to the laboratory that has not been demonstrated in the past. By simply exchanging the carrier solution from 2% HNO_3 to a 70:30 MeOH:H_2O solution, molecular sampling can be affected. As a result, psuedomolecular ions ($(M+H)^+$), similar to those seen in ESI or APCI, are formed. In previous works, the LS-APGD has been used to analyze a few different molecular species including small polar organic molecules, and proteins.[27] Figure 3.7 shows a typical mass spectrum containing five target compounds used in this work; caffeine, acetaminophen, sulfadimethoxine, terfenadine, and reserpine at 1 µg mL^{-1}. The composition of this mixture is very typical of the sorts used to benchmark performance of LC-MS systems. As can be seen, the overall spectral structure is quite clean, with each of these molecules (many of which are structurally very fragile) showing predominately psuedomolecular ions.

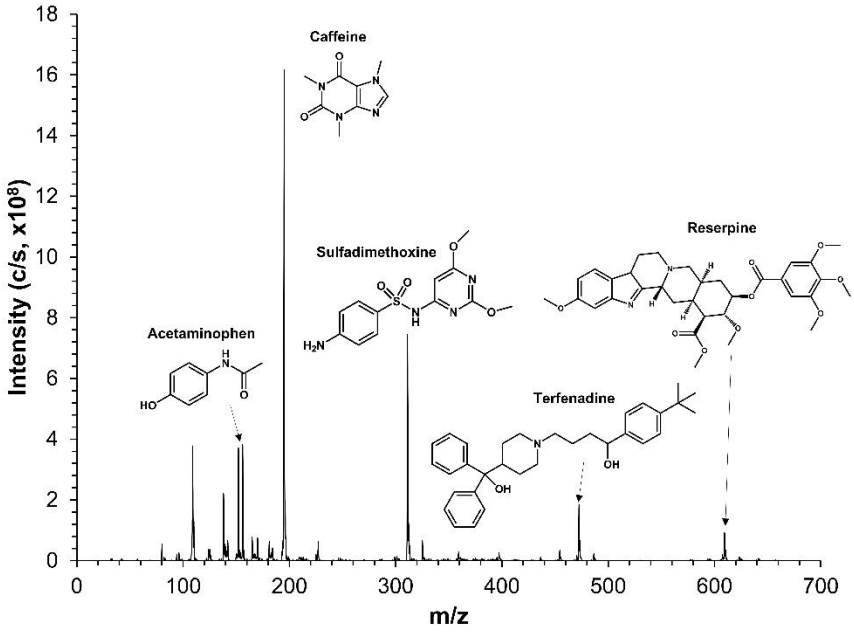

Figure 3.7: LS-APGD mass spectrum for a 1 µg mL^{-1} solution containing acetaminophen, caffeine, sulfadimethoxine, terfenadine, and reserpine in a 70:30 MeOH:H_2O carrier solution. 20 µL injection volume.

In order to effectively analyze these sorts of low molecular weight species, considerations of both the plasma operating parameters and the ion optics had to be made. First, the current of the plasma, set at 50 mA for elemental samples, was reduced to 30 mA as higher currents cause fragmentation of the analyte molecules and detracts from the response of the psuedomolecular ion.[28] While more extensive fragmentation may be of interest in further probing of structural information, the goal in this effort was to look at the preliminary sensitivity of this pairing. In addition, the source voltage offset value in the instrument, which acts as both a repulsion and fragmentation method, is returned to the value used for ESI (20 V) in order to prevent unwanted fragmentation. At this point, a more detailed DoE as related to structure of molecular species' product spectra is in order. In

addition, the ion optics will likely require further optimization due to the higher molecular weight of the analyte species.

The analytical figures of merit were determined for the 5 drug targets as well as well as Δ-9 tetrahydrocannabinol, which was added to provide another level of analyte diversity and analytical relevancy. The analyte concentrations for this characterization ranged from 1 – 10,000 ng mL^{-1}, with triplicate 20 μL injections used at each concentration. The much wider dynamic range employed here reflects the greater sensitivity of the CAM source towards these sorts of analytes. In fact, it is interesting to note that calibration quality of these molecules is better than the elemental species as well. The resultant limits of detection range between 1 – 32 nM, corresponding to mass-based values of 17-307 pg mL^{-1} and absolute mass values on the sub- and single-pg levels. These values are very much on par with those typically obtained with ESI, and in fact the concentration range used for this demonstration exceeds the dynamic range reported for this instrument with an ESI source, demonstrating not only the sensitivity, but also the versatility of this ion source.[41]

Table 3.3: Analytical figures of merit for drug targets. Response curve concentrations ranging from 1 – 10,000 ng mL^{-1} for 20 μL, triplicate injections.

Compound	*Equation*	*R^2*	*LOD (nM)*	*LOD (pg mL^{-1})*	*LOD (mass, pg)*	*S/N @ 100 ng mL^{-1}*	*%RSD @ 100 ng mL^{-1}*
Acetaminophen	y=8035.3x+3459	0.9971	12	45	0.9	13	5.8
Caffeine	y=37953x+308221	0.9975	11	36	0.7	152	9.7
Sulfadimethoxine	y=19920x+14400	0.9996	12	75	2	17	5.2
Δ9-Tetrahydrocannabinol	y=24067x+4265055	0.9996	6	196	4	32	2.4
Terfenadine	y=5493x+63860	0.9980	32	307	6	30	9.9
Reserpine	y=2371x+660	0.9999	1	17	0.3	27	8.5

3.4 Conclusions

The LS-APGD microplasma, a CAM ionization source, has been interfaced with an Advion Expression^{L} Compact Mass Spectrometer to bring its diverse sampling portfolio to a reduced-format MS platform. While atomic mass spectrometry platforms remain large, analytical laboratory-based instruments, this pairing is among the first examples of an elemental MS sampling system that would be capable of operation in the synthesis laboratory or a chemical production floor. A multi element test solution (Rb, Ag, Tl) was used to optimize the ion optics to tailor the ion transport of the instrument towards the mass range of relevance to elemental mass spectrometry. With these optimized instrument conditions, a multi-parametric evaluation was completed using an alternate multi-element solution (Na, Rb, Cs, Tl). LODs were determined for these four elements to be on the 10s of ng mL^{-1} level, but with absolute mass detection of sub- and single-ng quantities. The ability of the microplasma to deliver a more comprehensive range chemical information was demonstrated in the analysis of a variety of relevant drug targets that are commonly employed as ESI/APCI-MS benchmarks. In this case, detection limits on the low-nM level were determined, with absolute mass LODs at the 1 pg level. The mass spectra and sensitivity of the CAM source on this very simple MS platform are very much on par with those of ESI/APCI on commercial platforms. Ultimately, the LS-APGD/CMS pairing demonstrates promising capabilities as a CAM system which is readily implemented on this commercial analyzer.

Future work on this instrument will necessitate more thorough benchmarking for a greater range of elemental/molecular species, while continuing to look into further

applications and sampling modalities. Certainly, a greater range of elements and matrices must be evaluated. To reiterate, though, the goal here is not to yield sensitivities that rival commercial ICP-MS, but to develop capabilities which are relevant to practitioners for whom the reduced-format system is advantageous. In terms of molecular species sampling, a full optimization of the system and the ion source will be completed to maximize the potential in this coupling. Furthermore, additional molecular species, such as proteins, will be analyzed on this system with the ultimate goal of sampling via LC. Ultimately, the CAM ionization microplasma pairing to this reduced-format mass spectrometer will provide a system capable of analyzing diverse samples on an analytically flexible instrument platform.

3.5 Acknowledgements

Reproduced from "Coupling the liquid sampling – atmospheric pressure glow discharge, a combined atomic and molecular (CAM) ionization source, to a reduced-format mass spectrometer for the analysis of diverse species," Tyler J. Williams and R. Kenneth Marcus, 2020, with permission from the Royal Society of Chemistry. This work was supported through a collaboration with Advion Inc.

3.6 References

1. R. Thomas, *Practical Guide to ICP-MS: A Tutorial for Beginners*, CRC Press, Boca Raton, FL, 2013.
2. R. S. Houk, *Anal. Chem.*, 1986, **58**, 97A-105A.
3. R. S. Houk, V. A. Fassel, G. D. Flesch, H. J. Svec, A. L. Gray and C. E. Taylor, *Anal. Chem.*, 1980, **52**, 2283-2289.
4. E. Bolea-Fernandez, L. Balcaen, M. Resano and F. Vanhaecke, *J. Anal. At. Spectrom.*, 2017, **32**, 1660-1679.
5. S. D. Tanner, M. Paul, S. A. Beres and E. R. Denoyer, *At. Spectrosc.*, 1995, **16**, 16-18.
6. N. Jakubowski, L. Moens and F. Vanhaecke, *Spectrochim. Acta, Part B*, 1998, **53**, 1739-1763.
7. D. C. Baxter, I. Rodushkin and E. Engström, *J. Anal. At. Spectrom.*, 2012, **27**, 1355-1381.
8. D. W. Koppenaal, C. J. Barinaga and M. R. Smith, *J. Anal. At. Spectrom.*, 1994, **9**, 1053-1058.
9. N. Sugiyama and Y. Shikamori, *J. Anal. At. Spectrom.*, 2015, **30**, 2481-2487.
10. K. B. Lynch, A. Chen and S. Liu, *Talanta*, 2018, **177**, 94-103.
11. L. J. Kricka, *Clin. Chem.*, 2020, **44**, 2008-2014.
12. G. McMahon, *Analytical Instrumentation: A Guide to Laboratory, Portable and Minizaturized Instruments*, John Wiley & Sons, Ltd, 2007.
13. D. T. Snyder, C. J. Pulliam, Z. Ouyang and R. G. Cooks, *Anal. Chem.*, 2016, **88**, 2-29.
14. Z. Ouyang and R. G. Cooks, *Annu. Rev. Anal. Chem.*, 2009, **2**, 187-214.
15. A. R. Date and A. L. Gray, *Analyst*, 1981, **106**, 1255-1267.
16. A. L. Gray and A. R. Date, *Analyst*, 1983, **108**, 1033-1050.
17. P. Mezei and T. Cserfalvi, *Appl. Spectrosc. Rev.*, 2007, **42**, 573-604.
18. Q. He, Z. Zhu and S. Hu, *Appl. Spectrosc. Rev.*, 2014, **49**, 249-269.
19. P. Jamroz, K. Greda and P. Pohl, *TrAC, Trends Anal. Chem.*, 2012, **41**, 105-121.
20. T. Cserfalvi and P. Mezei, *Anal. Bioanal. Chem.*, 1996, **355**, 813-819.
21. T. Cserfalvi and P. Mezei, *J. Anal. At. Spectrom.*, 1994, **9**, 345-349.
22. T. Cserfalvi, P. Mezei and P. Apai, *J. Phys, D: Appl. Phys.*, 1993, **26**, 2184-2188.
23. M. R. Webb, G. C. Y. Chan, F. J. Andrade, G. Gamez and G. M. Hieftje, *J. Anal. At. Spectrom.*, 2006, **21**, 525-530.
24. A. J. Schwartz, K. L. Williams, G. M. Hieftje and J. T. Shelley, *Anal. Chim. Acta*, 2017, **950**, 119-128.
25. R. K. Marcus, B. T. Manard and C. D. Quarles, *J. Anal. At. Spectrom.*, 2017, **32**, 704-716.
26. R. K. Marcus, C. D. Quarles, C. J. Barinaga, A. J. Carado and D. W. Koppenaal, *Anal. Chem.*, 2011, **83**, 2425-2429.
27. L. X. Zhang, B. T. Manard, S. Konegger-Kappel and R. K. Marcus, *Anal. Bioanal. Chem.*, 2014, **406**, 7497-7509.

28. E. D. Hoegg, C. J. Barinaga, G. J. Hager, G. L. Hart, D. W. Koppenaal and R. K. Marcus, *J. Anal. At. Spectrom.*, 2016, **31**, 2355-2362.
29. E. D. Hoegg, B. T. Manard, E. M. Wylie, K. J. Mathew, C. F. Ottenfeld and R. K. Marcus, *J. Am. Soc. Mass Spectrom.*, 2019, **30**, 278-288.
30. E. D. Hoegg, S. Godin, J. Szpunar, R. Lobinski, David W. Koppenaal and R. K. Marcus, *J. Anal. At. Spectrom.*, 2019, **34**, 1387-1395.
31. L. X. Zhang, B. T. Manard, B. A. Powell and R. K. Marcus, *Anal. Chem.*, 2015, **87**, 7218-7225.
32. L. X. Zhang and R. K. Marcus, *J. Anal. At. Spectrom.*, 2016, **31**, 145-151.
33. E. D. Hoegg, S. Godin, J. Szpunar, R. Lobinski, D. W. Koppenaal and R. K. Marcus, *J. Am. Soc. Mass Spectrom.*, 2019, **30**, 1163-1168.
34. C. D. Quarles, Jr., A. J. Carado, C. J. Barinaga, D. W. Koppenaal and R. K. Marcus, *Anal. Bioanal. Chem.*, 2012, **402**, 261-268.
35. T. J. Williams and R. K. Marcus, *J. Anal. At. Spectrom.*, 2019, **34**, 1468-1477.
36. E. D. Hoegg, B. A. Patel, William N. Napoli, D. D. Richardson and R. K. Marcus, *J. Anal. At. Spectrom.*, 2018, **33**, 2015-2020.
37. *USA Pat.*, US 8,487,247 B2, 2013.
38. J. B. Anderson and J. B. Fenn, *Phys. Fluids*, 1965, **8**, 780-787.
39. J. B. Fenn, *Int. J. Mass Spectrom.*, 2000, **200**, 459-478.
40. E. D. Hoegg, C. J. Barinaga, G. J. Hager, G. L. Hart, D. W. Koppenaal and R. K. Marcus, *J. Am. Soc. Mass Spectrom.*, 2016, **27**, 1393-1403.
41. *Compact Mass Spectrometry*, Advion Inc., Ithaca, NY, 2018, https://www.advion.com/products/expression-cms/.

CHAPTER IV

DEVELOPMENT OF AN INTEGRATED SINGLE ELECTRODE LIQUID SAMPLING – ATMOSPHERIC PRESSURE GLOW DISCHARGE MICROPLASMA IONIZATION SOURCE

4.1 Introduction

In the last few decades, significant progress has been made towards the development of miniaturized instrumentation that requires less consumables, smaller sample sizes, and lower operational costs, all while providing greater automation. While the fields of separation science,[1, 2] organic mass spectrometry, [3, 4] optical spectroscopy,[5] and sensor technology[6] have all seen advances in this regard, atomic spectrometry has progressed at a far slower pace. Inductively coupled plasma (ICP)-based instruments have largely dominated the field of atomic spectrometry, and while they remain the workhorse instruments for many applications, they are large laboratory-based instruments with high operating and consumable costs.[7, 8] In particular, the high argon (Ar) gas consumption and temperatures necessitate stringent MS vacuum system requirements, with reductions in instrument size, sample volume, and consumable use remaining large challenges.[7] More recently, the emergence of atmospheric pressure glow discharge (APGD) sources for atomic mass spectrometry have shown significant promise as an alternative to ICP instruments.[9-11]

APGD sources, in general, require less consumables and are lower in capital cost than traditional plasma sources.[8, 12-14] The first iteration of solution-sampling APGD devices, termed the electrolyte as cathode discharge (ELCAD), was developed by Cserfalvi et al. in 1994 for use with optical emission spectroscopy (OES).[15, 16] Improving upon this

device, Hieftje et al. developed the solution cathode glow discharge (SCGD), which has been applied in OES and MS modalities.[11, 17-19] Another related APGD device is the liquid sampling – atmospheric pressure glow discharge (LS-APGD) microplasma developed by Marcus et al.[12, 20] The LS-APGD-MS has proven useful in a wide variety of applications ranging from elemental/isotopic analysis to combined atomic and molecular (CAM) mass spectrometry.[9, 21-29] The LS-APGD typically consists of a grounded solution electrode and a stainless-steel counter electrode, with the plasma formed between the two electrodes when a positive potential is applied to the counter electrode. Unlike the other systems mentioned previously, the LS-APGD runs in a total consumption mode, using low sample (<50 μL min^{-1}) and gas flow rates (<1 L min^{-1}), while maintaining a high-power density (5–50 W mm^{-3}) plasma. Importantly, the microplasma can be directly interfaced with any MS instrument having an atmospheric pressure interface of the sort utilized with ion sources common to organic MS.

Over the past few years, a number of studies have developed applications for the LS-APGD including U isotope ratio analysis, analysis of trace metals in high matrix samples (cell culture media), and coupling to a reduced format mass spectrometer as a CAM ionization source. [23, 29, 30] While not a pre-requisite in regards to the goals of instrument miniaturization (where compromises are anticipated), sensitivity towards elemental species still falls short in comparison to ICP-MS. Recent efforts have sought to improve the source design in order to provide more sensitive atomic MS analysis through the addition of multiple counter electrodes.[28] Hoegg et al. demonstrated operation using two, three, and four counter electrodes, noting a dramatic improvement in sensitivity (up

to 175x) with additional electrodes due to the increased power density of the plasma. In fact, the sensitivity improvements seen with the multiple electrode designs approach levels seen with ICP-MS instruments.[28] Unfortunately, this increase in performance comes at some cost of source simplicity and manufacturing/materials costs, though still far less onerous than ICP sources.

The work presented here focuses on the initial development of a new electrode geometry for the LS-APGD that aims to simplify the original, single counter electrode design while providing similar or enhanced performance. This new design simplifies the ion source by forming a glow discharge plasma between the solution electrode and the sampling orifice of a mass spectrometer, serving as the counter electrode. This new configuration, termed the integrated, single electrode design, limits the source to only a single moving part, with the coupling of the discharge directly to the MS inlet providing direct sampling of the plasma. In order to perform an initial evaluation of this LS-APGD design, the source was interfaced with a triple quadrupole mass spectrometer that employs an ion transfer capillary (ITC),[31] against which the plasma was generated. A preliminary optimization was performed involving the discharge current, liquid flow rate (electrolyte and sample), and electrode gap (sampling distance). Perhaps the most significant difference between this source and the original LS-APGD design is that the potential is applied to the solution electrode, rather than the discrete counter electrode, with the ITC held at ground potential. Post optimization, preliminary figures of merit for a multi-element solution containing Rb, Ag, Tl, and U were substantially improved relative to the conventional two-electrode source design. The implementation of this new source is expected to simplify

operation, limit the number of moveable components, and reduce materials costs, with improvements in analytical performance.

4.2 Materials and Methods

4.2.1 Sample Preparation

Two different stock solutions were used in this work, one for the optimization of the source and establishment of analytical figures of merit and another for the analysis of solvent-related species and spectral composition comparisons between source designs. The first solution was prepared by diluting Rb, Ag, and U elemental standards (High Purity Standards; Charleston, SC) and dissolving a $Tl(NO_3)$ salt (Beantown Chemical; Hudson, NH) in 2% HNO_3 (Sigma-Aldrich; St. Louis, MO) to prepare a 10 μg mL^{-1} solution. The second solution was prepared by diluting Cu, Cs, Cd, and Pb elemental standards (Cu, Cs, and Pb; CPI International; Santa Rosa, CA and Cd; High Purity Standards, Charleston, SC) to 10 μg mL^{-1} in 2% HNO_3.

4.2.1 Source Design

The integrated, single electrode design is a simple variant based on the LS-APGD presented in previous works.[10, 21, 32] Figure 4.1a depicts the original LS-APGD-MS electrode geometry, which contains a grounded solution cathode and a powered, stainless-steel counter electrode. In the integrated single electrode design, Fig 4.1b, the stainless-steel counter electrode is removed, utilizing only the solution electrode. In both cases, this consists of a fused silica capillary (280 μm i.d., 580 μm o.d., Restek Corporation, Bellefonte, PA) that introduces the electrolytic solution (sample) into the plasma (10-100 μL min^{-1}) supplied via a syringe pump (Chemyx Fusion 100, Chemyx, Stafford, TX). This

inner capillary is housed within a stainless-steel capillary (316 SS, 0.8 mm i.d., 1.6 mm o.d., IDEX Health and Science, Oak Harbor, WA), which supplies a He sheath gas (0.2 L min^{-1}). The upper volume of the sheath gas flow rate was limited by the He pumping capacity of the mass spectrometer, thus restricting full evaluation. The discharge maintenance potential was provided via a Spellman (Hauppauge, NY) SP150 power supply operated in the negative output mode (0-150 mA, 0-2 kV). In all cases, the solution electrode is placed in-line with the sampling cone of the mass spectrometer with a variable sampling distance of 0.5 – 3 mm (note that sampling distances beyond 3 mm were unable to sustain a plasma). The ion transfer capillary of the sampling cone is electrically grounded relative to the plasma sustaining electrodes.

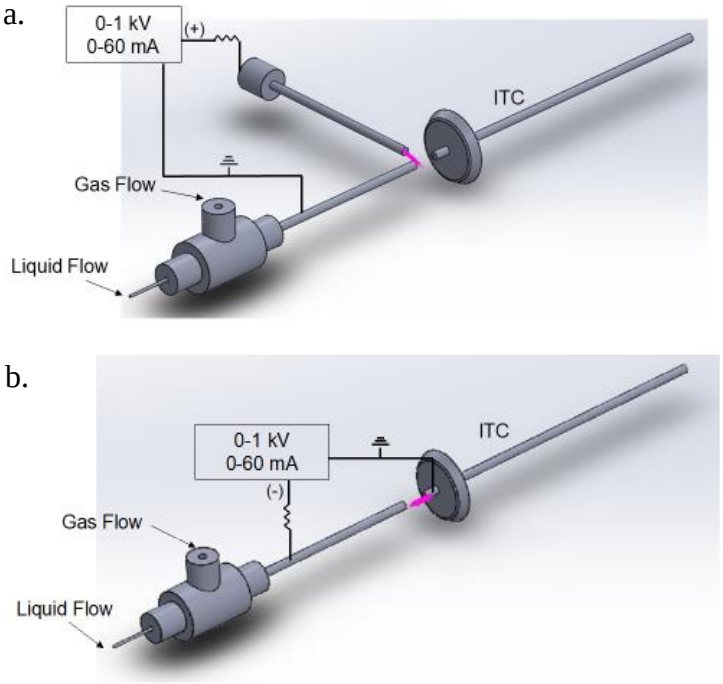

Figure 4.1: Diagram of a) the original single electrode LS-APGD source design b) the integrated single electrode LS-APGD design.

4.2.2 Mass Spectrometer System

A TSQ Quantum Access MAX (Thermo Scientific, San Jose, CA) triple quadrupole mass spectrometer was utilized in this work. Instrument parameters were controlled through the TSQ Tune software and corresponding data acquisition system. As described in previous works, no alterations were made to the instrument other than the removal of the equipped ESI source.[21, 31] Different from triple quadrupole (TQ) instruments now applied in ICP-MS, the second quadrupole in the TSQ is a bent quadrupole, which acts solely as a collision cell in lieu of the more common collision/reaction cells found in TQ-ICP instruments.[33, 34] In this work, Q1 was used as the analytical mass filter, whereas Q2 and Q3 were operated in the rf-only mode, with no collision gas (Ar) used in the second quadrupole. This is due in part to the desire to see a pure picture of the plasma-produced species, but also because the common collision induced dissociation (CID) strategies programmed into the instrument only allow operation in a comprehensive MS/MS format, not in a simple scanning-MS modality. To be sure, one would not expect this analyzer geometry to be as sensitive as those commonly applied in elemental MS. Due to a negative potential supplied to the ion transfer capillary by the integrated, single electrode design, offset (+10 V) was applied between the skimmer cone and ion transfer capillary (ITC) to facilitate the transmission of ions, alleviating (via the system software) further use of that potential to affect in-source CID. While proven valuable in previous implementations of the microplasma in conjunction with similar MS systems, this does allow for a truer picture of the plasma processes.

4.2.3 Parametric Optimization

A multi-variable design of experiment (DoE) protocol created with JMP software (SAS Institute Inc., Cary, NC) was used to optimize the integrated, single electrode design. This parameterization was done with regards to maximizing both the analyte signal and the signal-to-background (S/B) ratio for the elements in the 10 µg mL^{-1} multi-element solution described above. Table 4.1 presents the discharge parameters examined and the ranges tested where in total, 36 sets of conditions were examined, with three replicates of each condition examined. For each set of conditions, a 50 µL injection of the test solution was employed. Mass spectrometric data was acquired in the selected ion monitoring (SIM) mode, where Q1 was employed as the mass analyzer and operating Q2 and Q3 in rf-only modes. The integrated analyte signal intensities and S/B ratios for each analyte were determined. The S/B was evaluated at each analytes' most abundant isotope using the analyte peak area and an equivalent peak area determined for the time segment prior to the injection.

Table 4.1: Range of discharge parameters that were evaluated in the DoE process along with the produced optimized conditions.

Parameter	*Tested Conditions*	*Optimized Conditions*
Current (mA)	20 – 50	45
Liquid Flow (µL min^{-1})	10 – 60	60
Sampling Gap (mm)	0.5 – 3	3

4.3 Results and Discussion

4.3.1 Source Design and Operating Mode

Early studies of the LS-APGD on OES systems looked at the various powering modes of the LS-APGD, including solution grounded cathode (SGC), solution grounded anode (SGA), solution powered cathode (SPC), and solution powered anode (SPA).[35] More recently, those modalities were evaluated towards uranium isotope ratio measurements on an Orbitrap mass spectrometer.[36] Both sets of studies demonstrated that the SGC mode provided the greatest analyte responses and sensitivity, as well as the greatest stability/isotopic precision.[35, 36] While success has been realized with this ion source across a broad range of applications, efforts to further improve upon this system in terms of analytical performance and simplicity of design are investigated here.

The original LS-APGD-MS electrode design is depicted in Fig 4.1a. With this operating mode, the discharge is struck between the grounded solution electrode and a separate counter electrode to which a potential is applied. The positioning of these components has been investigated in previous works in terms of electrode gap and sampling distance from the mass spectrometer.[31, 32] The new design, Fig. 4.1b, utilizes only a solution electrode and generates the discharge versus the sampling orifice of the mass spectrometer, which is electrically grounded. This integrated, single electrode design reduces the number of moving parts to just the position of the solution electrode, where the 'electrode gap' and 'sampling distance' become identical. Clear from these two figures is the fact that species emanating from the solution electrode in the original design do so perpendicular to the direction in which the plasma is situated, whereas, in the integrated

design, they pass through the entirety of the plasma volume. Work by Perkins et al. has observed the sampling angle of the LS-APGD, noting that a "head-on" geometry gives way to the most efficient sampling brought on through the directionality of the sheath gas flow, with analyte intensities decreasing as the solution electrode/sheath gas flow is brought perpendicular to the sampling orifice.[36] Additionally, this direct coupling to the sampling orifice, or ion transfer capillary (ITC), is expected to add improved flow of the plasma species based on the directionality of the sheath gas flow, facilitating transport into the mass spectrometer.

One of the practical challenges associated with the integrated, single electrode design is that the typical powering mode of the original single electrode design, SGC, can no longer be used. As previously mentioned, the present design utilizes the mass spectrometer ITC as the counter electrode and placing a large potential on the mass spectrometer inlet is prohibitive, requiring significant modification of the mass spectrometer ion optics. This limits the powering modes to those in which the solution electrode is powered while the counter electrode, the ITC of the MS system, is electrically grounded. As a result, the two powering modes that can be utilized are the SPA and SPC modes, the difference being the polarity of the power supply, positive and negative, respectively. It should be noted that these were the two worst-performing configurations (solution powered) in the previous OES and MS studies.[35, 36] In addition, the grounded ITC does in fact float to a non-negligible potential (regardless of whether it is acting as anode or cathode), affecting the transmission of ions into the mass spectrometer. In the case of the SPA mode, a high positive potential (≈300 V) develops on the ITC, causing excessive

repulsion/scattering of ions and thus poor ion transmission through the interface. In contrast, running in SPC yields a slight negative potential (≈-300V) on the ITC, affecting the transport of ions through the MS ion optics and resulting in little or no analyte response. However, the negative potential could be overcome by utilizing the instrument's in-source CID function, which applies a positive potential to the end of the ITC. As it was only possible to sample ions in the SPC powering mode, the design in Fig. 4.1b was adopted.

4.3.2 Parametric Optimization

A multi-variable parametric optimization was undertaken to investigate the effects of the discharge operating conditions, including the discharge current, liquid flow rate, electrode/sampling gap, and any inter-parametric effects. This parameterization was conducted in a manner analogous to recent works, in which a brief screening of the discharge conditions was conducted to roughly define which matrix of parameters provided stable plasma operation.[31] The discharge conditions that were tested in the full optimization are listed in Table 4.1. The final discharge conditions were optimized based on maximizing both the analyte responses and S/B ratios.

The results of the parameterization are expressed in the form of Pareto plots,[37] Figs. 4.2a and b, illustrate the combined influence of the various parameters on the test mix (Rb, Ag, Tl, and U), with inter-parametric effects represented by the "*" between two parameters. The vertical line in each figure represents a level of statistical significance (logworth ≥ 2 for a 99% confidence interval), where parameters having values that extend beyond that line have a significant effect on that performance metric. Figure 4.2a details the effects of each parameter on the analyte signal intensities showing that only the current

and the liquid flow have a statistically significant effect on operation. In recent works by Hoegg et al. and Williams et al., higher power density plasmas, which result from increasing discharge current, elicit increased analyte response.[28, 29] Ultimately, too high of a current, especially with the limited sheath gas flow rates available on this MS coupling, leads to melting of the inner capillary, and thus a slightly lower current (45 mA) had to be utilized.[29, 31] Furthermore, the use of higher liquid flow rates provides additional analyte entering into the plasma per unit time (and potentially becoming ionized), consistent with previous works.[29] Significant at the 95% confidence interval (logworth = 1.3) is the inter-parametric interaction between liquid flow and current, as increased analyte delivery rates work in tandem with the higher currents (discharge energy), resulting in higher analyte responses.

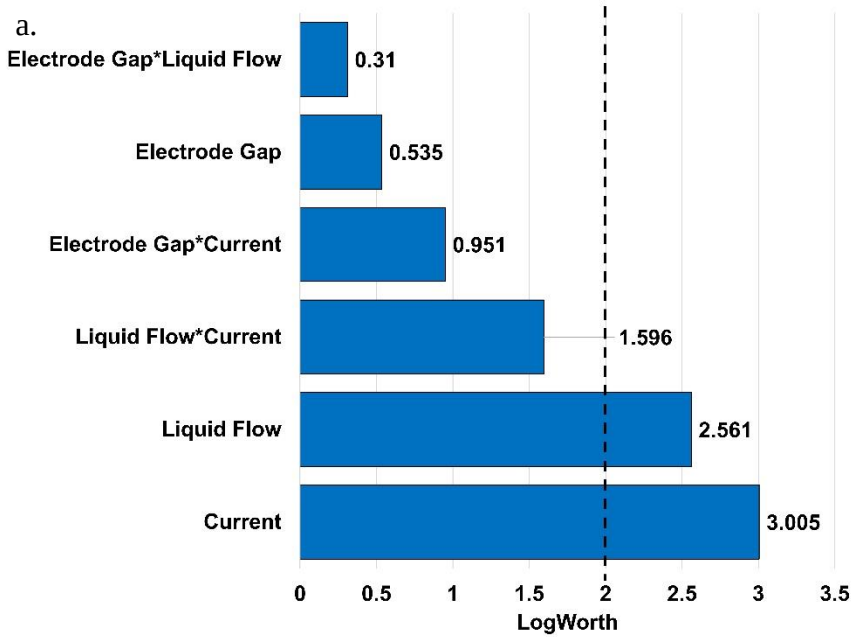

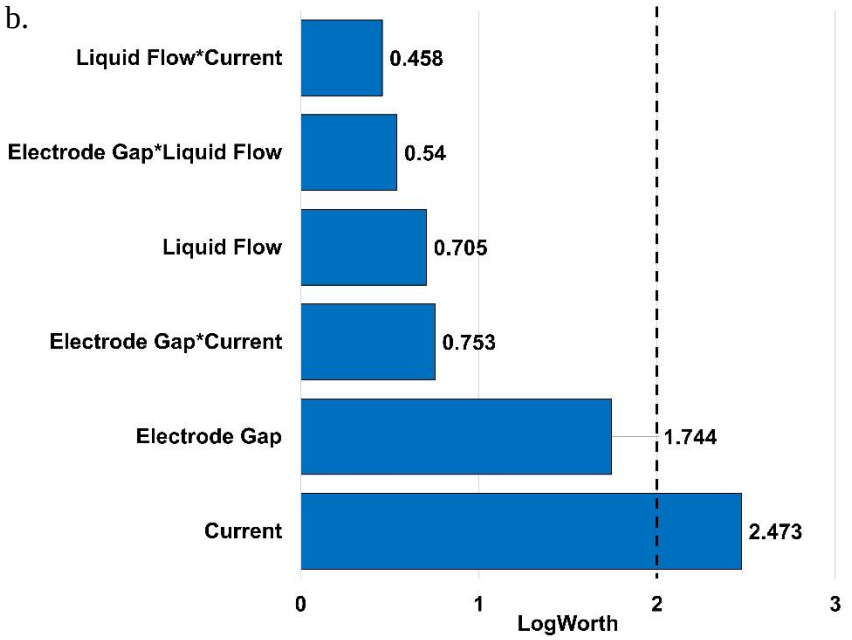

Figure 4.2: Bar graph reflecting the combined significance of each LS-APGD operating parameter as well as inter-parametric effects on the a) analyte signal intensity and b) analyte signal-to-background ratios. Concentration = 10 μg mL^{-1} for each element (Rb, Ag, Tl, U), injection volume = 50 μL, n = *3.*

Displayed in Fig. 4.2b are the effects of the discharge conditions on the S/B ratio, where again the parameters with a statistically significant effect (logworth ≥ 2 for a 99% confidence interval) extend beyond the dashed vertical line. As with the analyte response, the discharge current has a significant influence over the analyte S/B, although in this case, it is the only significant parameter. Because an increased discharge current results in increases in both analyte signal and S/B, this suggests that although the analyte signal increases, background species do not simultaneously increase or may decrease. To this end, background species formed in the LS-APGD are typically molecular solvent related clusters which may be mere effectively dissociated at the elevated discharge currents/temperatures. Significant at the 95% confidence interval was the

electrode/sampling gap, where a larger sampling gap provides increased S/B. Previous works have detailed the effect of increasing electrode gaps in providing improved ionization efficiency,[38, 39] suggesting larger effective plasma volumes, albeit not in-line with the ion sampling process. Distinct from these works, the electrode gap for the integrated design not only acts to both increase the analyte residence time in the plasma but also the sampling distance from the mass spectrometer. Williams et al. demonstrated previously that increased sampling distance results in lower analyte intensity as a result of less analyte reaching the mass spectrometer;[31] indeed, this is borne out in Fig. 4.2a. On the contrary, the increasing electrode gap in the integrated systems does influence the S/B, suggesting that the direct integration of the source with the mass spectrometer provides an increased residence time in the plasma, facilitating the reduction of background molecular species. Lastly, the liquid flow, which had a significant effect on the analyte response, shows an insignificant effect on the S/B. While more analyte reaching the plasma results in a higher analyte signal (Fig. 4.2a), the larger total volume of liquid reaching the plasma then results in a higher background, suggesting that liquid flow has comparable effects on both signal and background. Ultimately, in both signal and S/B, no inter-parametric effects are statistically significant. Using the JMP software, a set of optimum conditions to maximize analyte signal and S/B were generated (Table 4.1).

4.3.3 Comparison of Operating Modes – Elemental Responses

Due to the variety of differences between the integrated, single electrode design and the original geometry, it is reasonable to compare the sources with respect to the targeted analyte responses as well as the product mass spectral characteristics which affect

S/B and potential isobaric interferences. There are a few notable differences that would affect the elemental sensitivities. Firstly, the powering mode used in the new design is SPC as opposed to SGC, which is used in the original design. The SPC operating mode has been previously described as performing poorer than the SGC operating mode across both MS and OES platforms.[35, 36] Another difference is that in the integrated, single electrode mode, the discharge is generated directly to the entrance of the mass spectrometer. Lastly, the discharge conditions in each design are different, though both have been optimized for analytical performance in the respective operating modes. A survey test solution containing Cu, Cs, Cd, and Pb was used in this set of experiments. Based on the premise that the use of in-source CID can affect the fragmentation of molecular species down to their atomic ion forms, the intensities for each species related to each analyte were summed as being representative of the yield for each of the test metals.

In these experiments, four geometries/modes of operation were used to investigate differences affected by source design; the original design operated in SGC and SPC modes, and the integrated single electrode design operated under the pre- and post-optimization conditions and a summary of discharge conditions as summarized in Table 4.2. The pre-optimization conditions for the integrated electrode were chosen to be the same as those employed for the original design. Shown in Fig. 4.3 is the comparison between the original and integrated single electrode designs for triplicate injections of a 10 μg mL^{-1} solution of Cu, Cs, Cd, and Pb. Starting with the original geometry in the SGC and SPC powering modes, it was anticipated that there would be a great disparity between the two; this was not the case. Work by Davis and Marcus noted substantially lower emission intensity from

the LS-APGD when operating in the SPC mode with the likely explanation stemming from the solution-phase processes as well as the solution/air interface dynamics.[35] While there are no significant differences in the MS responses, it may be that some of those solution/air interface processes are acting here to promote slightly poorer measurement precision (≈2x reduction in precision). This result corresponds with work by Perkins *et al*. where the SPC powering mode resulted in poorer uranium isotope ratio measurement precision.[36] The integrated, single electrode geometry operating in the unoptimized conditions (same conditions as SGC and SPC) yields a 5-10x increase in analyte response over the original geometry, even though the discharge conditions are exactly the same. This appears to support a hypothesis that using the entrance of the mass spectrometer as the counter electrode provides a longer residence within the active plasma as well as facilitates transport into the mass spectrometer. Finally, operation under the optimized conditions for the single electrode does increase signal intensities in some cases, but not to the same degree of changing the electrode geometries. What is not clear from the responses depicted in Fig. 4.3 are the corresponding differences in the spectral characteristics as a function of the source geometry/powering conditions.

Table 4.2: Discharge conditions employed for each mode comparing the original and integrated, single electrode source designs.

	Original Geometry (SGC)	*Original Geometry (SPC)*	*Integrated, Single Electrode – Unoptimized*	*Integrated, Single Electrode – Optimized*
Current (mA)	30	30	30	45
Liquid Flow ($\mu L\ min^{-1}$)	30	30	30	60
Gas Flow ($L\ min^{-1}$)	0.2	0.2	0.2	0.2
Electrode Gap (mm)	1.5	1.5	--	--
Sampling Distance (mm)	0.5	0.5	1.5	3

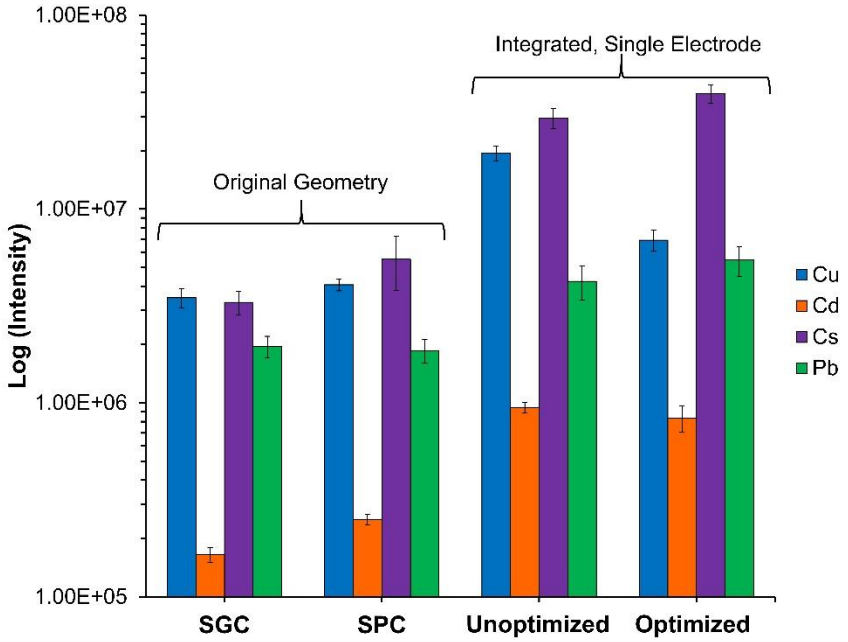

Figure 4.3: Bar graph comparing the summed intensities of the analyte response in the original single electrode design operating in the SGC and SPC modes, the integrated single electrode design prior to optimization, and in the optimized integrated single electrode mode. Error bars represent the standard deviation of the measurements. Concentration = 10 $\mu g\ mL^{-1}$ for each element (Cu, Cs, Cd, and Pb), injection volume = 20 μL, n = 3.

4.3.4 Comparison of Operating Modes – Spectral Composition

Described in past works, a variety of ions of solvent-related molecular species produced in the original LS-APGD geometry of the.[25, 32, 38] Whilst these species are readily alleviated via in-source dissociation, it is instructive to look at the native production of such species to gain operational insights. To provide a comparison between the two designs, a previously employed,[31, 32] multi-element solution containing Cu, Cs, Cd, and Pb (10 μg mL^{-1}, each) was examined. Figure 4.4a depicts the spectrum (on a relative abundance scale) for a 50 μL injection of this solution taken with the original electrode design. It can be seen that a variety of solvent-related molecular species form within the plasma. In the cases of Cu, Cd, and Pb, there is an abundance of species of the form $[M(NO_3)(H_2O)_n]^+$, which have been described in previous works.[31] Additionally, Cs and Cu form compounds with the addition of solvent molecules $(H_2O)_n$. The formation of these species is fully expected as relevant species from the 2% HNO_3 matrix. In the absence of in-source CID, the presence of these diverse species is problematic from the point of view of spectral complexity as well as diminishing "atomic" responses.

In the case of the integrated, single electrode geometry, the parametric optimization was shown to have an appreciable effect on the analyte S/B ratios (Fig. 4.2b), while the elemental responses depicted in Fig. 4.3 suggest minimal improvements. The broad band mass spectra acquired under the original-geometry conditions and those following the parametric optimization are quite telling in terms of the fundamental plasma processes. In brief, as listed in Table 4.2, the optimized conditions employ higher discharge currents and analyte solution flow rates, as well as a longer sampling distance. As presented in Fig. 4.4b,

operation of the single electrode geometry under the previous discharge conditions yields a mass spectrum of far greater complexity than seen for the original geometry presented in Fig. 4.4a. While some of the identified analyte-containing species are consistent between the two spectra, contributions from solvent-related (2% HNO_3) species produce ion signals at virtually all m/z values. In the absence of effective in-source CID, this spectrum is practically un-viable towards multi-element, trace analysis. The corresponding mass spectrum taken under the DoE-optimized conditions for the single electrode geometry is presented in Fig. 4.4c. Comparison to the spectrum of the un-optimized case (Fig. 4.4b) displays features that provide insights into the roles of the different operation conditions. As suggested previously, the increase in both analyte solution flow and discharge current under the optimized conditions should result in the greater delivery of analyte and solvent loading of the plasma while providing more energy to affect the gas phase dissociation and ionization processes. What is seen in the spectral responses, though, is the fact that the longer sampling distance (3 mm vs. 1.5 mm) yields a dramatic reduction in solvent related spectral background. The combination of longer sampling distance and higher discharge current affect a situation wherein those species have a longer residence time within the active plasma region, acting to dissociate those species to a greater extent.

a.

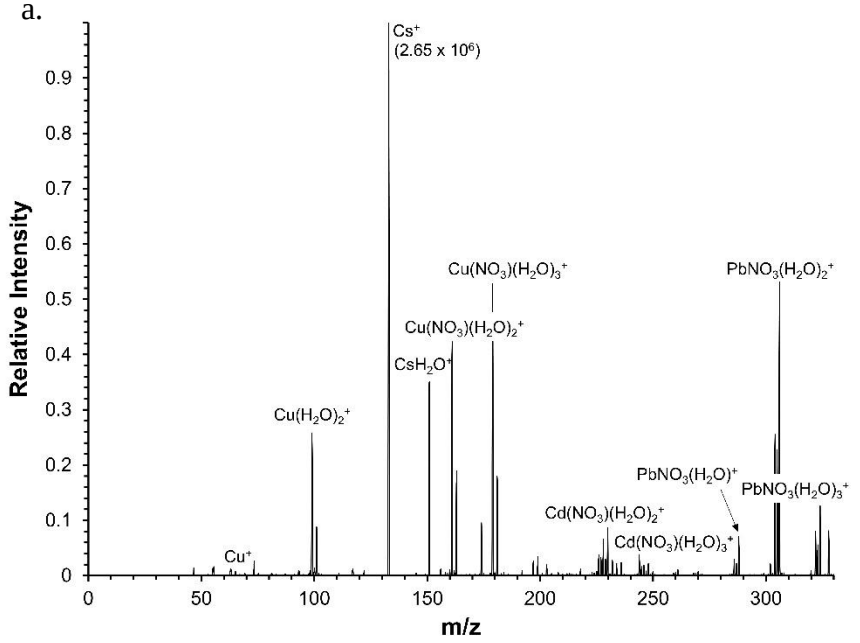
Cs+
(2.65 x 10^6)
Cu(NO3)(H2O)3+
PbNO3(H2O)2+
Cu(NO3)(H2O)2+
CsH2O+
Cu(H2O)2+
PbNO3(H2O)+
PbNO3(H2O)3+
Cd(NO3)(H2O)2+
Cd(NO3)(H2O)3+
Cu+
Relative Intensity
m/z

b.

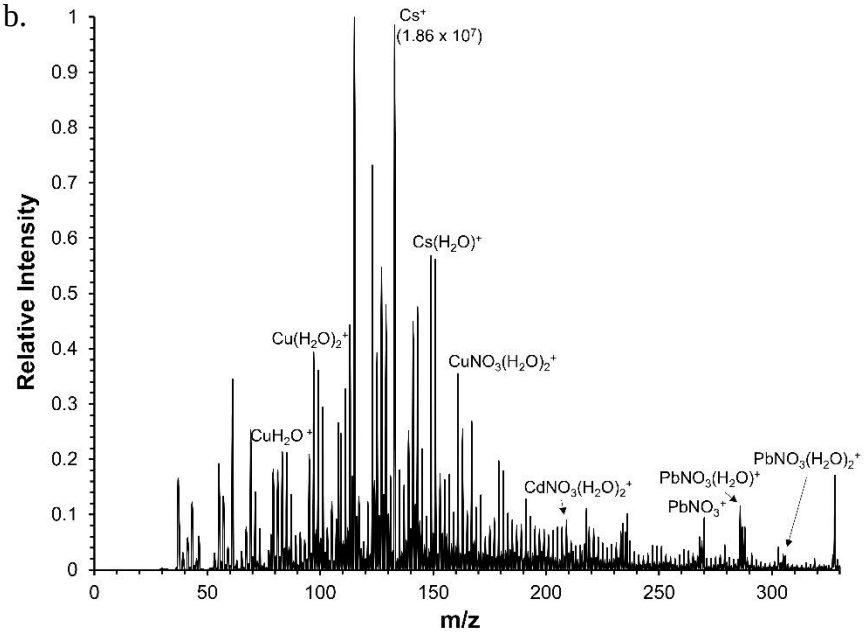
Cs+
(1.86 x 10^7)
Cs(H2O)+
Cu(H2O)2+
CuNO3(H2O)2+
CuH2O+
CdNO3(H2O)2+
PbNO3(H2O)+
PbNO3+
PbNO3(H2O)2+
Relative Intensity
m/z

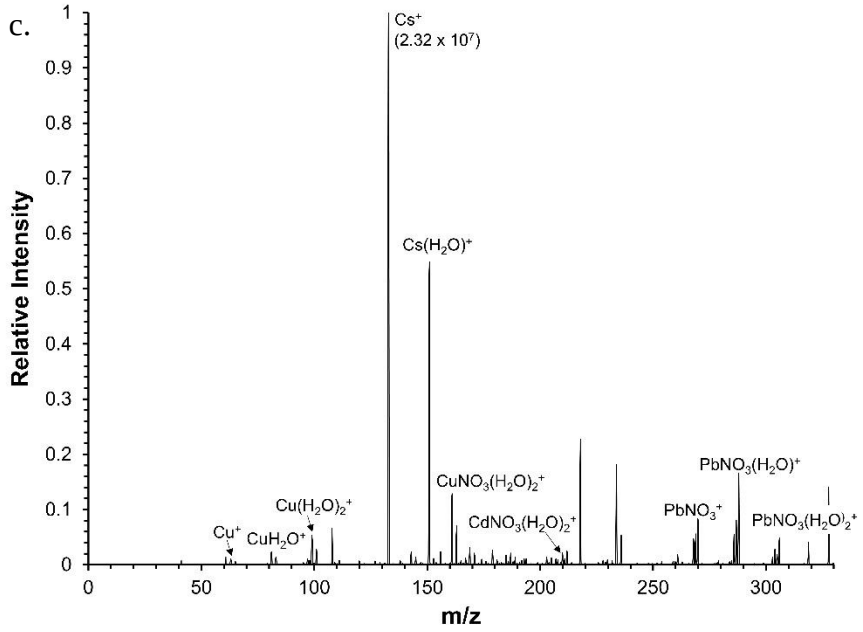

Figure 4.4: Multi-element LS-APGD-MS spectra taken with the a) original LS-APGD electrode geometry b) the integrated single electrode LS-APGD at unoptimized conditions and c) the integrated single electrode LS-APGD at optimized conditions with 10 μg mL^{-1} of each element (Cu, Cs, Cd, and Pb).

A comparison of the product mass spectrum from the optimized single electrode geometry (Fig. 4.4c) and the original design (Fig. 4.4a) is informative. Similar to the original design, there is an abundance of $[M(NO_3)(H_2O)_n]^+$ species being formed for Cu, Cd, and Pb. While many of the same species form in both operating modes, the degree of hydration (number of water molecules) tends to be greater for the original design. For example, in Fig. 4.4a, Cu is most abundant as $Cu(NO_3)(H_2O)_3^+$, while in Fig. 4.4c, few of those species are present, in favor of fewer numbers of waters. From these spectra, while many of the same species are formed in both operating modes, the lower energy of the original electrode design results in the formation of larger complexed species, or

alternatively, they are less favorable dissociated in the plasma. Based on the arguments presented above, it is believed that enhanced dissociation is realized in the current geometry. In fact, the ratio of summed molecular intensities to the atomic ion intensities decreases in the integrated, single electrode powering mode. Finally, whether a product of more effective molecular species dissociation or overall higher atomic ionization efficiencies, the integrated, single electrode geometry delivers ≈10x greater atomic ion yields for the analytes contained in this suite.

4.3.5 Limits of Detection

Limits of detection (LOD) were obtained using the multi-element solution (Rb, Ag, Tl, and U) employed in the discharge parameter optimization. This test mixture is the same as was used in previous works on this instrument with the original electrode geometry, facilitate a direct comparison of LODs on this platform [31]. For the same reason, determinations of LODs were made using a method developed by Boumans and Vrakking based on the relative standard deviation of the background (RSBD) and S/B ratio [40, 41]. This method calculates detection limits based on the concentration of a single point, essentially, the ability to distinguish the analyte signal above the background. This is calculated using the following formula:

$$LOD = \frac{(0.01)k(RSDB)m}{(S/B)}$$

where m is the concentration of the analyte in solution and k is a statistical factor corresponding to the confidence interval. In this work, a multiplier of k=3 is used, representing a 99% confidence interval.

The LODs were obtained by performing three 20 μL injections of the 100 ng mL^{-1} multi-element solution (2 ng absolute, for each element) and monitoring the analyte masses using selected ion monitoring (SIM). For each analyte, the integrated signal for a fixed time period prior to injection was employed to assess the background characteristics and the integrated response for the transient over the same time employed to assess the analytical signal. The calculated LODs for the four elements are presented in Table 4.3. Note that the values determined for the original design are based on 50 μL sample injections.[31] The determined LODs for the integrated, single electrode geometry ranged from LODs range from 0.02 to 0.17 ng mL^{-1}, marking 72 – 1900x improvements in sensitivity over the original electrode design. Importantly, these concentrations represent absolute masses of 0.4 to 3.4 pg. The final two columns of Table 4.3 provide insights into the spectral characteristics observed at a concentration of 100 ng mL^{-1} (2 ng absolute mass) as well as the obtained precision for triplicate injections at that concentration. Overall, it is believed that the coupling of the integrated, single electrode design directly to the mass spectrometer provides more facile ion transport than the original electrode geometry and increases the simplicity of the source design.

Element	*Original Geometry LOD (ng mL^{-1})* [31]	*Original Geometry LOD (pg)* [31]	*Integrated, Single Electrode LOD (ng mL^{-1})*	*Integrated, Single Electrode LOD (pg)*	*Integrated, Single Electrode S/B at 100 ng mL^{-1}*	*Integrated, Single Electrode %RSD at 100 ng mL^{-1}*
Rb	0.99	50	0.02	0.4	6.6	6.4
Ag	4.9	245	0.17	3.4	2.6	17.7
Tl	38	1900	0.05	1	5.4	6
U	3.48 (270 Da)	174	0.16 (386 Da)	3.2	2.5	7.1

Table 4.3: Computed limits of detection based on the use of the Boumans' method of determination.[40, 41] *Injection volume = 20 μL, concentration 100 ng mL^{-1}, n=3.*

4.4 Conclusions

A new integrated, single electrode design of the LS-APGD has been demonstrated and interfaced to a triple quadrupole platform. Distinct from the common LS-APGD designs, which generate a plasma between a solution electrode and a counter electrode, the single electrode design generates a plasma versus the mass spectrometer inlet, which acts as the counter electrode. In this design, species emanating from the solution electrode pass through the entire plasma volume and are more efficiently transported into the mass spectrometer. Necessitated by the differences in operation, a thorough multi-parametric optimization was performed using a simple multi-element test solution (Rb, Ag, Tl, and U). To gain insight into mass spectral characteristics, sources of differences between the designs were investigated, including the powering mode (SGC vs SPC), the direct

interfacing to the mass spectrometer, and the optimization of discharge conditions. The inability to employ in-source CID with this coupling has the consequence of allowing the assessment of the raw spectral characteristics of the respective sources in terms of product molecular species. Even in the absence of CID, the new design leads to an improvement of ≈10x in analyte response over the original design. The sensitivity of this source design was compared to the original geometry, yielding improvements in LODs of 2-3 orders of magnitude.

Future work will seek to further refine this source design and characterize operational differences from the original source geometry. A modification to the ion transfer capillary mounting to isolate voltages emanating from the ion source and the in-source CID should be employed to fully realize the utility of this pairing. Likewise, implementation of the comprehensive triple quadrupole platform capabilities will provide a rich tool for MS/MS analysis, taking advantage of the CAM aspects of the microplasma. Coupling to other platforms such as previous works with Orbitrap instruments is expected. Finally, the lower degree of operational complexity of the single electrode is expected to yield better overall system robustness and provide a more facile approach to portable MS applications.

4.5 Acknowledgements

Reproduced from "Development of an integrated, single electrode liquid sampling – atmospheric pressure glow discharge microplasma ionization source," Tyler J. Williams and R. Kenneth Marcus, 2020, with permission from Elsevier. This work was supported in part by the Defense Threat Reduction Agency, Basic Research Award #HDTRA1-14-1-

0010, to Clemson University. High Purity Standards (North Charleston, SC, USA) is gratefully acknowledged for the donation of the elemental standards.

4.6 References

1. K. B. Lynch, A. Chen and S. Liu, *Talanta*, 2018, **177**, 94-103.
2. L. J. Kricka, *Clin. Chem.*, 1998, **44**, 2008-2014.
3. Z. Ouyang and R. G. Cooks, *Anal. Bioanal. Chem.*, 2009, **2**, 187-214.
4. D. T. Snyder, C. J. Pulliam, Z. Ouyang and R. G. Cooks, *Anal. Chem.*, 2016, **88**, 2-29.
5. G. McMahon, *Analytical Instrumentation: A Guide to Laboratory, Portable and Miniaturized Instruments*, John Wiley & Sons, Ltd., 2007.
6. F. Valentini, A. Calcaterra, S. Antonaroli and M. Talamo, *Sensors*, 2018, **18**.
7. R. Thomas, *Practical Guide to ICP-MS: A Tutorial for Beginners*, CRC Press, Boca Raton, Fl, 2013, 3rd
8. V. Karanassios, *Spectrochim. Acta, Part B*, 2004, **59**, 909-928.
9. R. K. Marcus, C. D. Quarles, C. J. Barinaga, A. J. Carado and D. W. Koppenaal, *Anal. Chem.*, 2011, **83**, 2425-2429.
10. C. D. Quarles, A. J. Carado, C. J. Barinaga, D. W. Koppenaal and R. K. Marcus, *Anal. Bioanal. Chem.*, 2012, **402**, 261-268.
11. A. J. Schwartz, K. L. Williams, G. M. Hieftje and J. T. Shelley, *Anal. Chim. Acta.*, 2017, **950**, 119-128.
12. R. K. Marcus, B. T. Manard and C. D. Quarles, *J. Anal. At. Spectrom.*, 2017, **32**, 704-716.
13. M. R. Webb and G. M. Hieftje, *Anal. Chem.*, 2009, **81**, 862-867.
14. P. Mezei and T. Cserfalvi, *Appl. Spectrosc. Rev.*, 2007, **42**, 573-604.
15. T. Cserfalvi and P. Mezei, *J. Anal. At. Spectrom.*, 1994, **9**, 345-349.
16. T. Cserfalvi, P. Mezei and P. Apai, *J. Phys. D Appl. Phys.*, 1993, **26**, 2184-2188.
17. M. R. Webb, F. J. Andrade and G. M. Hieftje, *Anal. Chem.*, 2007, **79**, 7899-7905.
18. M. R. Webb, F. J. Andrade and G. M. Hieftje, *J. Anal. At. Spectrom.*, 2007, **22**, 775-782.
19. A. J. Schwartz, J. T. Shelley, C. L. Walton, K. L. Williams and G. M. Hieftje, *Chem. Sci.*, 2016, **7**, 6440-6449.
20. R. K. Marcus and W. C. Davis, *Anal. Chem.*, 2001, **73**, 2903-2910.
21. E. D. Hoegg, C. J. Barinaga, G. J. Hager, G. L. Hart, D. W. Koppenaal and R. K. Marcus, *J. Am. Soc. Mass Spectrom.*, 2016, **27**, 1393-1403.
22. E. D. Hoegg, C. J. Barinaga, G. J. Hager, G. L. Hart, D. W. Koppenaal and R. K. Marcus, *J. Anal. At. Spectrom.*, 2016, **31**, 2355-2362.
23. E. D. Hoegg, B. T. Manard, E. M. Wylie, K. J. Mathew, C. F. Ottenfeld and R. K. Marcus, *J. Am. Soc. Mass Spectrom.*, 2019, **30**, 278-288.
24. E. D. Hoegg, S. Godin, J. Szpunar, R. Lobinski, D. W. Koppenaal and R. K. Marcus, *J. Anal. At. Spectrom.*, 2019, **34**, 1387-1395.
25. L. X. Zhang, B. T. Manard, B. A. Powell and R. K. Marcus, *Anal. Chem.*, 2015, **87**, 7218-7225.
26. L. X. Zhang and R. K. Marcus, *J. Anal. At. Spectrom.*, 2016, **31**, 145-151.
27. E. D. Hoegg, S. Godin, J. Szpunar, R. Lobinski, D. W. Koppenaal and R. K. Marcus, *J. Am. Soc. Mass Spectrom.*, 2019, **30**, 1163-1168.

28. E. D. Hoegg, T. J. Williams, J. R. Bills, R. K. Marcus and D. W. Koppenaal, *J. Anal. At. Spectrom.*, 2020, **in press**.
29. T. J. Williams and R. K. Marcus, *J. Anal. At. Spectrom.*, 2020, **in press**.
30. E. D. Hoegg, B. A. Patel, William N. Napoli, D. D. Richardson and R. K. Marcus, *J. Anal. At. Spectrom.*, 2018, **33**, 2015-2020.
31. T. J. Williams and R. K. Marcus, *J. Anal. At. Spectrom.*, 2019, **34**, 1468-1477.
32. L. X. Zhang, B. T. Manard, S. Konegger-Kappel and R. K. Marcus, *Anal. Bioanal. Chem.*, 2014, **406**, 7741-7741.
33. E. Bolea-Fernandez, L. Balcaen, M. Resano and F. Vanhaecke, *J. Anal. At. Spectrom.*, 2017, **32**, 1660-1679.
34. N. Sugiyama and Y. Shikamori, *J. Anal. At. Spectrom.*, 2015, **30**, 2481-2487.
35. W. C. Davis and R. K. Marcus, *Spectrochim. Acta, Part B*, 2002, **57**, 1473-1486.
36. A. A. Perkins, E. D. Hoegg and R. K. Marcus, *Spectrochim. Acta, Part B*, 2021, **176**, 106044.
37. A. Bevilacqua, M. Corbo and M. Sinigaglia, *Current research, technology and education topics in applied microbiology microbial biotechnology*, Formatex Research Center, 2010.
38. M. S. Davis, W. C. Davis, W. Y. Ensign, K. W. Hinchcliff, T. C. Holbrook and K. K. Williamson, *J. Am. Vet. Med. A*, 2008, **232**, 873-878.
39. S. Konegger-Kappel, B. T. Manard, L. X. Zhang, T. Konegger and R. K. Marcus, *J. Anal. At. Spectrom.*, 2015, **30**, 285-295.
40. P. W. J. M. Boumans and J. J. A. M. Vrakking, *Spectrochim. Acta, Part B*, 1987, **42**, 819-840.
41. P. W. J. M. Boumans, *Spectrochim. Acta, Part B*, 1991, **46**, 917-939.

CHAPTER V

MASS SPECTROMETRIC CHARACTERISTICS AND PRELIMARY FIGURES OF MERIT FOR POLYAROMATIC HYDROCARBONS VIA THE LIQUID SAMPLING – ATMOSPHERIC PRESSURE GLOW DISCHARGE MICROPLASMA

5.1 Introduction

The characterization of xenobiotic species in the environment is of great importance for the evaluation of exposure limits and health effects.[1-4] Polyaromatic hydrocarbons (PAHs) formed from the thermal decomposition of organic matter are produced through both natural (i.e., forest fires) and unnatural means (oil spills, engines, etc.). The introduction of these compounds into the environment, either as airborne species or in the condensed phase (foliage/soil/water), is of both human and ecological concern.[1-5] Many PAHs have been identified as carcinogens, mutagens, and teratogens, meaning that the ability to detect and characterize these compounds is a necessity.[1-4]

Although these species can be challenging to identify, a variety of mass spectrometric (MS) techniques exist which enable their measurement, including; atmospheric pressure chemical ionization (APCI), AP photoionization (APPI), electron ionization (EI), electrospray ionization (ESI). Realizing the complexity of such samples, liquid and gas chromatography (LC and GC) separation are commonly employed prior to EI, APCI, and APPI, providing direct coupling and high throughput.[2, 5-8] APCI and APPI rely on ion/molecule interactions between the solvent and analyte to initiate a charge-transfer, forming radical cations of PAHs. Typically, N_2 gas is ionized at the corona discharge (APCI) or through interaction with light (APPI). The ionized N_2 proceeds to ionize solvent molecules through ion/molecule interactions and the now-ionized solvent

molecules undergo an e^- charge transfer exchange resulting in the PAH radical cations.[2, 6, 9]

There is a push for ionization sources having diverse sampling/analysis capabilities, eliminating the necessity for multiple ion sources/instruments.[10] The liquid sampling – atmospheric pressure glow discharge (LS-APGD) microplasma has been developed as a versatile ionization source for mass spectrometry.[11] Developed with a focus on elemental analysis as an alternative to the inductively coupled plasma (ICP), the LS-APGD is a low power, low sample consumption ionization source.[12, 13] Uniquely, it has the ability to perform as a combined atomic and molecular (CAM) ionization source, demonstrating abilities to analyze not only atomic species, but small molecules and proteins by a simple change of the mobile phase.[14-16] A MeOH:H_2O solvent, as opposed to 2% HNO_3, yields high densities of $MeOH_2^+/H_3O^+$ (Brønsted acids) as the primary means of charge balance with electrons in the plasma. While the LS-APGD has demonstrated a diverse sampling portfolio, to this point, low polarity molecules have yet to be investigated.

Presented here is the first demonstration of the analysis of low polarity, aromatic species using the LS-APGD microplasma. As expected, based on electron densities on the order of 10^{15} cm^{-3} and inherent Penning ionization processes,[11] radical cations of these species were formed, though interestingly, protonated $(M+H)^+$ species were also observed in near-equal abundance. Thus, gas-phase $MeOH_2^+/H_3O^+$ provides a means of proton donation. A range of PAHs and the use of various solvents are investigated to gain insights into the role of solvent-originating proton donors on the balance of the ionization mechanisms. Preliminary figures of merit set the stage for potential analytical applications.

It is believed that the ability to couple both LC and GC separations with the LS-APGD microplasma offers unique attributes for applications in PAH analyses, complementing the CAM-MS aspects of the device.

5.2 Experimental

Samples were prepared as 10 µg mL^{-1} solutions of selected PAHs in a 70:30 MeOH:H_2O solution. The compounds selected represent various low-polarity PAHs, with a range of proton affinities (PA) (Table 5.1).[17] Naphthalene was purchased from JT Baker (Phillipsburg, NJ); acenaphthene, pyrene, and chrysene were purchased from Aldrich chemical company (Milwaukee, WI); and perylene was purchased from Sigma Aldrich (St. Louis, MO). Methanol (HPLC grade) was purchased from VWR (Radnor, PA) and mixed with deionized water prepared by an Elga PURELAB flex water purification system (18.2 MΩ cm^{-1}) (Veolia Water Technologies, High Wycombe, England). Toluene was purchased from Acros Organics (Bridgewater, NJ), chloroform was purchased from Millipore (Burlington, MA), and dichloromethane was purchased from VWR. Calibration solutions were prepared through serial dilutions of the stock 10 µg mL^{-1} solutions in 70:30 MeOH:H_2O.

The LS-APGD/Orbitrap coupling has been detailed in previous works.[12, 13] The LS-APGD is comprised of a solution cathode and a stainless-steel anode between which the plasma is generated.[13] The electrolytic carrier solution is introduced through the inner capillary at a rate of 30 µL min^{-1} via a syringe pump (Chemyx Inc., Stafford, TX). Power is supplied to the counter electrode (SS weldable feedthrough, Insulator Seal Inc., Sarasota, FL) by a Spellman SL60 (Hauppauge, NY) direct current power supply at 30 mA. In all

cases, 20 µL samples were introduced via a manual six-port injector, with analyses performed in triplicate.

Table 5.1: Ratio of protonated species to radical cation for each analyte in 70:30 MeOH:H_2O and the proton affinities for the respective analytes and solvents.

	$(M+H)^+/M^{+\cdot}$	*Proton Affinity (kJ/mol)*
Naphthalene[17]	0.26	802.1
Chrysene[17]	0.30	840.9
Acenaphthene[17]	0.40	851.7
Pyrene[17]	9.15	869.2
Perylene[17]	8.66	888.6
Water[18]	--	697
Methanol[18]	--	761
Toluene[18]	--	784
Chloroform[19]	--	647
Dichloromethane[19]	--	628

The LS-APGD was interfaced with a ThermoScientific Q Exactive Focus mass spectrometer (Waltham, MA). No modifications were necessary to the instrument other than removing the standard ESI.[13] The mass spectrometer was controlled using the Thermo Tune operating system and data acquisition software and was operated in the positive ion mode. The system was operated at a resolution of $m/\Delta m \approx 70{,}000$ (m/z=200). Each scan was comprised of 10 microscans, an ion injection time of 100 ms, and an automatic gain

control (AGC) target of 1 million charges. In these experiments, 15 eV in-source collision-induced-dissociation (CID) was applied to reduce background solvent species.

5.3 Results and Discussion

Past works have demonstrated the ability of the LS-APGD to affect the ionization of molecular samples simply by altering the identity of the carrier solution. To this point, the compounds analyzed with the LS-APGD consisted exclusively of polar "small" molecules and biomacromolecules, which are commonly analyzed through ESI or APCI. There remains a large group of unexplored compounds, having no polar sites for protonation, which are analyzed typically by APCI or APPI.[1, 6, 8, 9, 20, 21] The LS-APGD, being a glow discharge, operates through a combination of electron and Penning ionization mechanisms. On this basis, it was expected that a radical cation could be generated, either through a low energy EI, Penning ionization, or charge transfer initiated through ion-molecule interactions. Previous molecular-MS studies demonstrated operation in a realm between APCI and ESI, protonating in the gas phase like APCI, but also forming multiple charged states akin to ESI.[14] As shown in Figs. 5.1a) naphthalene and b) pyrene, both radical cations and protonated molecular ions were formed, suggesting concurrent EI/Penning ionization and protonation.

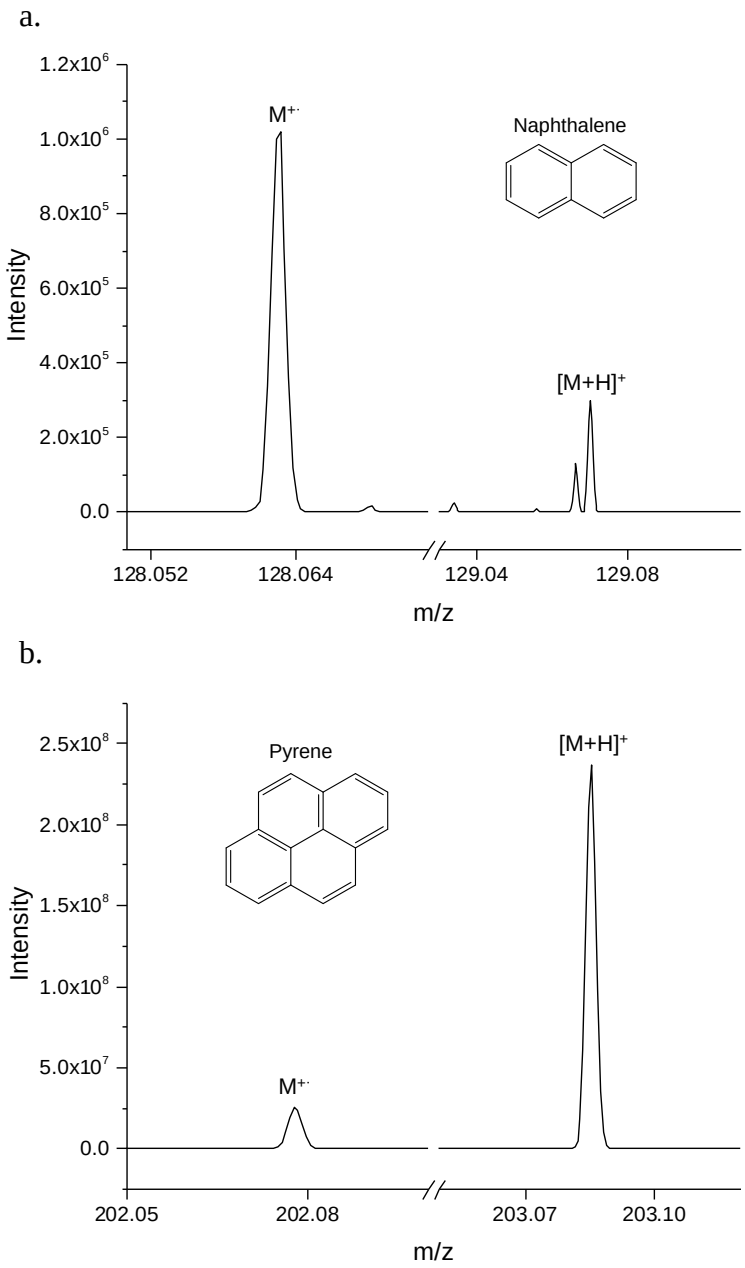

Figure 5.1: Mass spectra showing the formation of both the radical cation and protonated ions of a) naphthalene and b) pyrene, representing the upper and lower ends of the PA range used in these studies. Experimental aspects appear in text.

The formation of protonated molecular PAHs has been demonstrated across a wide variety of ionization sources, and while their observation is not novel, their formation may

provide insights into the LS-APGD's operating mechanism. For example, as the LS-APGD yields mass spectra for polar compounds most similarly to an ESI or APCI ionization source, protonated PAHs are not commonly observed in those sources, though interestingly, they are seen in the desorption versions of those sources.[1, 5, 7] Protonated species are common in APPI and low-pressure PI ionization sources where photo-generated proton donors are the active agents.[6, 8, 21] Thus, is seems clear that protonation in the microplasma is through a gas-phase reaction, rather than in the solvent phase as ESI.

Protonation of molecular species in the microplasma is through gas phase interactions, where $MeOH_2^+$ or H_3O^+ would act as the proton donors in this mixed-solvent system.[14] Table 5.1 lists the $(M+H)^+/M^{+\cdot}$ values for the measured analytes in MeOH:H_2O as well as the PAs of the analytes and the solvent systems used. Clearly the PAs of the analytes impact the protonation of PAHs, in agreement with work by Syage on LPPI,[6] based on the relative PAs of the solvent and analyte molecules. Thus, it would be expected that the solvent system will play a role into the relative extents of the proton transfer and cationization processes. Figure 5.2 presents the analyte responses for the radical cation and the protonated molecular ion forms of pyrene for methanol, toluene, chloroform, and DCM carrier solvents. The solvents here represent polar protic, "borderline" polar aprotic, and non-polar solvents. As expected, the polar protic solvent, methanol, has the highest yield for the protonated molecular ion, while the non-polar solvent, toluene, retards protonated molecular ion formation, with somewhat suppressed radical formation. Perhaps most interesting, is the lack of influence of chloroform and DCM solvent systems, representing non-polar and borderline aprotic solvents respectively. These were expected to, like

toluene, result in minimal formation of the protonated molecular ion, though interestingly, they both have relatively similar response where there is a slightly greater formation of the protonated ion *vs.* the radical cation. Figure 5.2 suggests that the total ion yields across these solvents is fairly uniform (a positive attribute when considering future LC-MS applications), with the radical cation responses being less dependent on solvent identity than the pseudo-molecular ion. This is not surprising as the electron/Penning ionization processes are fundamental to having a functional plasma, regardless of the solvent. For those non-polar systems, ambient humidity is likely the source of protonation, though protonation may occur through dopant effects arising from other aromatic species, including toluene or other PAHs.[6, 21] Various additional factors may influence the overall ionization efficiency between these solvents including the boiling point and dielectric constant. For example, toluene does see a significant drop in the total ion yield likely stemming from inefficient solute transport into the gas phase due to its elevated boiling point relative to the other solvent systems. Furthermore, a conductive solution is necessary to enable stable plasma operation, which would be hindered due to the significantly lower dielectric constants seen in the solvents other than methanol, which may result in suppressed yields.

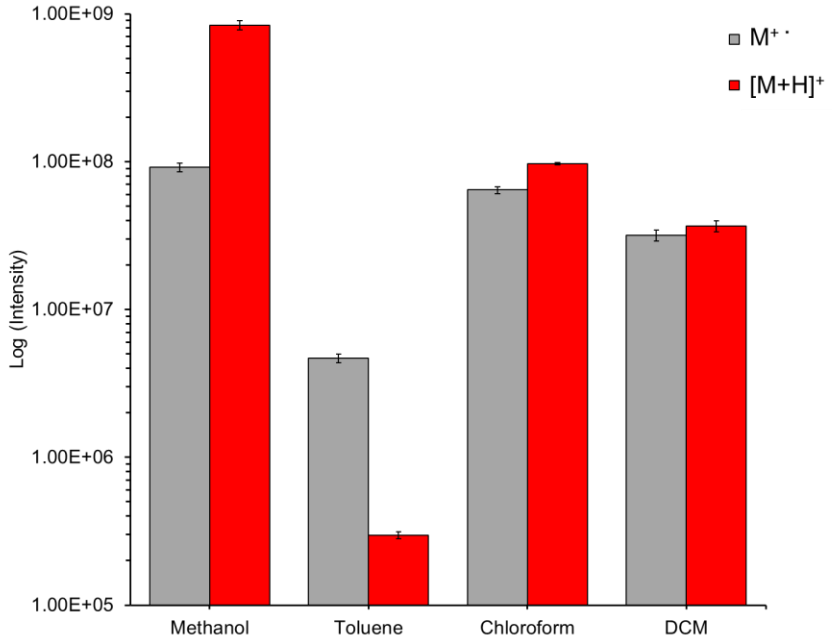

Figure 5.2: Influence of electrolytic carrier solution identity on the distribution of pyrene responses for the respective $(M+H)^+$ and $M^{+\cdot}$ forms. Experimental aspects appear in text.

In an effort to obtain preliminary information as to the analytical utility of the microplasma source with regards to PAH analysis, response curves were constructed for naphthalene and pyrene in 70:30 MeOH:H_2O, where the signals from both the protonated molecular ion and radical cation species was summed for each (Table 5.2). In both instances, linear response curves covering >2.5 orders of magnitude were realized, with R^2-values of >0.99. One clear difference between the two analytes, which is revealed in the spectral intensity responses in Fig. 5.1, is the far greater (>50X) sensitivity of pyrene over naphthalene. This is similar to work by Cha *et al.* which suggests that sensitivity of PAHs is a function of increasing molecular weights and PA, and additionally tracks with results from the EPA method 610.[22, 23] Based on the background thresholding process in the system processing, the standard deviation of the intensities for triplicate injections of

the lowest concentration measured was used to compute the limits of detection (LOD=$3\sigma_{low}$/m). For naphthalene, a detection limit of 28 ng mL^{-1} was obtained, while for pyrene, the detection limit was 270 pg mL^{-1}. For comparison, the EPA method for detection of PAHs, deems detection limits of 1.8 ng mL^{-1} for naphthalene and 270 pg mL^{-1} for pyrene as acceptable.[22] Given the fact that no parametric optimization has been performed to enhance the species' responses, it would be expected that those targets could be realized for both of the species and likely translated to other PAHs.

Table 5.2: Analytical figures of merit for natpthalene and pyrene as determined in 70:30 MeOH:H_2O. Injection volume = 20 µL, n=3, LOD = $3\sigma_{low}/m$.

Analyte	*Response function*	R^2	*LOD (ng mL^{-1})*	*LOD (pg)*	*%RSD @ 2X LOD*
Naphthalene	y = 627x + 34683	0.9906	28	560	4.6
Pyrene	y = 375045x + 373923	0.999	0.27	5.4	5.8

5.4 Conclusions

The already-versatile sampling repertoire of the LS-APGD microplasma has been expanded, adding low polarity PAHs. Interestingly, not only was an EI/Penning-produced radical cation formed, but protonated ions, $(M+H)^+$, were also observed for a variety of lower-molecular weight PAHs. Naturally, the PA of both the solvent and the analyte play a role in the degree to which protonation occurs. The overall responsivity for pyrene was found to be fairly insensitive to the solvent system. Preliminary response functions and LODs suggest promise relative to EPA method 610 guidelines for analytical methods. Future work in this application will expand on the capabilities of sampling low polarity species and probing the mechanisms of the ionization process through the use of deuterated

solvent systems. Based on the preliminary figures of merit, there may be excellent analytical opportunities in the determinations of PAHs separated by either GC or LC with LS-APGD microplasma ionization source.

5.5 Acknowledgements

Reproduced from "Mass spectrometric characteristics and preliminary figures of merit for polyaromatic hydrocarbons *via* the liquid sampling-atmospheric pressure glow discharge microplasma," Tyler J. Williams, Jacob R. Bills, and R. Kenneth Marcus, 2020 with permission from the Royal Society of Chemistry.

5.6 References

1. X. Zheng, K. T. Dupuis, N. A. Aly, Y. Zhou, F. B. Smith, K. Tang, R. D. Smith and E. S. Baker, *Anal. Chim. Acta*, 2018, **1037**, 265-273.
2. D. W. Potter and J. Pawliszyn, *Environ. Sci. Technol.*, 1994, **28**, 298-305.
3. C. E. Bostrom, P. Gerde, A. Hanberg, B. Jernstrom, C. Johansson, T. Kyrklund, A. Rannug, M. Tornqvist, K. Victorin and R. Westerholm, *Environ. Health Perspect.*, 2002, **110 (3)**, 451-488.
4. K. Ravindra, R. Sokhi and R. Van Grieken, *Atmos. Environ.*, 2008, **42**, 2895-2921.
5. L. Molnárné Guricza and W. Schrader, *J. Mass Spectrom.*, 2015, **50**, 549-557.
6. J. A. Syage, *J. Am. Soc. Mass Spectrom.*, 2004, **15**, 1521-1533.
7. H. Moriwaki, *J. Mass Spectrom.*, 2016, **51**, 1096-1102.
8. J. M. Purcell, C. L. Hendrickson, R. P. Rodgers and A. G. Marshall, *J. Am. Soc. Mass Spectrom.*, 2007, **18**, 1682-1689.
9. A. Ahmed, C. H. Choi, M. C. Choi and S. Kim, *Anal. Chem.*, 2012, **84**, 1146-1151.
10. T. R. Covey, B. A. Thomson and B. B. Schneider, *Mass Spectrom.Rev.*, 2009, **28**, 870-897.
11. R. K. Marcus, B. T. Manard and C. D. Quarles, *J. Anal. At. Spectrom.*, 2017, **32**, 704-716.
12. R. K. Marcus, C. D. Quarles, Jr., C. J. Barinaga, A. J. Carado and D. W. Koppenaal, *Anal. Chem.*, 2011, **83**, 2425-2429.
13. E. D. Hoegg, C. J. Barinaga, G. J. Hager, G. L. Hart, D. W. Koppenaal and R. K. Marcus, *J. Am. Soc. Mass Spectrom.*, 2016, **27**, 1393-1403.
14. L. X. Zhang and R. K. Marcus, *J. Anal. At. Spectrom.*, 2016, **31**, 145-151.
15. E. D. Hoegg, S. Godin, J. Szpunar, R. Lobinski, D. W. Koppenaal and R. K. Marcus, *J. Am. Soc. Mass Spectrom.*, 2019, **30**, 1163-1168.
16. T. J. Williams and R. K. Marcus, *J. Anal. At. Spectrom.*, 2020, **35**, 1910-1921.
17. D. H. Aue, M. Guidoni and L. D. Betowski, *Int. J. Mass Spectrom.*, 2000, **201**, 283-295.
18. E. P. L. Hunter and S. G. Lias, *J. Phys. Chem. Ref. Data*, 1998, **27**, 413-656.
19. I. K. C. Silwal, J. C. Rasaiah, J. E. Szulejko and T. Solouki, *Int. J. Mass Spectrom.*, 2010, **293**, 1-11.
20. M. Farenc, Y. E. Corilo, P. M. Lalli, E. Riches, R. P. Rodgers, C. Afonso and P. Giusti, *Energy Fuels*, 2016, **30**, 8896-8903.
21. T. J. Kauppila, T. Kuuranne, E. C. Meurer, M. N. Eberlin, T. Kotiaho and R. Kostiainen, *Anal. Chem.*, 2002, **74**, 5470-5479.
22. *Method 610: Polynuclear Aromatic Hydrocarbons*, United States Environmental Protection Agency, 1984.
23. E. Cha, E. S. Jeong, S. B. Han, S. Cha, J. Son, S. Kim, H. B. Oh and J. Lee, *Anal. Chem.*, 2018, **90**, 4203-4211.

CHAPTER VI

ROLES OF COLLISIONAL DISSOCIATION MODALITIES ON SPECTRAL COMPOSITION AND ISOTOPE RATIO MEASUREMENT PERFORMANCE OF THE LIQUID SAMPLING – ATMOSPHERIC PRESSURE GLOW DISCHARGE / ORBITRAP MASS SPECTROMETER COUPLING

6.1 Introduction

While numerous scientific disciplines utilize isotope ratio (IR) analysis as a primary methodology, nonproliferation and nuclear research communities have been primary drivers for new techniques and instrumentation.[1-3] IR analysis typically relies upon mass spectrometry (MS), which is considered the benchmark, and has benefitted from advances in measurement accuracy, precision, and detection limits. The most common methods for isotope ratio analysis, and elemental analysis in general, are inductively coupled plasma (ICP) - MS and thermal ionization mass spectrometry (TIMS).[1, 2] While the benefits of these methods are immense, they suffer from drawbacks including high upfront costs, complicated sample preparation, and high consumable usage. In the case of ICP-MS, high liquid flow rates (>0.4 mL min^{-1}) necessitate large sample volumes and subsequent waste management.[4-6] Atomic isobaric interferences, such as $^{40}Ar^{+}$ on ^{40}K or ^{40}Ca, and those due to molecular species have been among the most notable drawbacks, leading to the development of various methodologies including triple quadrupole collision/reaction systems, cool plasma conditions, and of course the use of high resolution sector field ICP-MS instruments.[4, 6-8] ICP-MS systems typically employed for isotope ratio analysis employ sector-field mass analyzers (SF-ICP-MS), which while attaining high resolution ($m/\Delta m$ of up to ~10,000), are insufficient to overcome many potential isobaric interferences.[4] TIMS

instruments, while considered the gold standard for isotope ratio measurements, are large, complex, and very expensive, with extensive sample analysis times.[2, 9] In addition, the sample preparation methods required for TIMS involve the complete isolation of the target analyte from all other matrix components.[10] These practicalities have driven the investigation of alternative ionization sources to deliver high precision and high accuracy isotope ratio measurements on ultra-high-resolution ($m/\Delta m >> 10{,}000$) instrumentation, while utilizing considerably reduced operational overhead.[11] Ultra-high resolution orbitrap mass analyzers hold the promise of providing mass resolution far superior to sector-field platforms, while being appreciably less onerous in terms of operational complexity, footprint, and, indeed, cost.

Efforts in this and collaborator laboratories have focused on the development of the liquid sampling – atmospheric pressure glow discharge (LS-APGD), first as an elemental/isotopic ionization source,[11, 12] and more recently as a combined atomic and molecular (CAM) ionization source.[13-18] Relative to more common spectrochemical devices, the LS-APGD is particularly attractive due to its simplicity, versatility, small format, and low consumable use. The LS-APGD is operated in a total consumption mode, using liquid (sample) flow rates of <100 µL min^{-1} and He gas flow rates of <1 L min^{-1}, all while maintaining a ~50 W mm^{-3} power density.[19] A unique component of this device is its ability to operate as a CAM ionization source, initially demonstrated by Zhang *et al.*,[14, 16] and more recently in a number of reports.[13, 15, 20] Importantly, this source has the ability to interface with any mass spectrometer having standard atmospheric pressure ionization (API) interfaces and has been integrated with quadrupole, triple-quadrupole, 3D Paul trap,

and Orbitrap mass spectrometers.[12, 13, 17, 21-23] Furthermore, sampling with the LS-APGD-MS, while typically performed via liquid introduction, has also been conducted through methods including ambient desorption,[24] laser ablation of particles into the plasma,[25, 26] or solvent extraction off of cotton swipes.[27] Perhaps the most promising demonstration of the LS-APGD microplasma is through the measurement of U isotope ratios, as UO_2, using Orbitrap mass spectrometers.[9, 11, 23, 28, 29] The primary advantages of Orbitrap Fourier transform mass spectrometry towards IR analysis are the incredibly high mass resolving powers (which should minimize sample preparation requirements) and the simultaneous detection of all relevant isotopes (which should result in improved precision).

Initial works with the LS-APGD/Orbitrap system utilized a ThermoScientific Exactive Orbitrap mass spectrometer. While initial measurement precisions (%RSD) of ~0.5% for the $^{235}U/^{238}U$ isotope ratio were obtained,[11] improvements in sampling methodologies including the use of collisional dissociation and filtering of concomitant ions, have since been utilized to affect improved precision and accuracy. The presence of background and concomitant ions (water clusters, matrix components, other analytes) limits the fraction of analyte collected in the orbitrap cell, leading to potential space charge effects which influence the measurement. While initial pairings utilized in-source collisional dissociation, a variety of species, both analyte- and solvent-related, are still permitted to enter the orbitrap analyzer. Overcoming this, Hoegg *et al*. coupled the LS-APGD to a Q Exactive Plus Orbitrap mass spectrometer,[28] which contains a quadrupole bandpass filter allowing for the attenuation of ions outside a selected analytical mass window prior to entering the orbitrap analyzer. This study demonstrated that by selectively

rejecting concomitant ions using the quadrupole filter, improvements in analyte signal sensitivity, isotope ratio accuracy, and measurement precision were realized. With these sampling methodologies, the LS-APGD/Q Exactive Plus achieved the International Atomic Energy Agencies (IAEA) International Target Values (ITV) for measurement uncertainty, reaching a $^{235}U/^{238}U$ precision of 0.086% RSD for natural U.[28] Further investigation of these acquisition parameters may allow additional understanding of how this pairing functions and lead to continued improvements in measurement performance.

Eiler and colleagues have recently described use of Orbitrap MS platforms to perform difficult stable isotope analyses of organic molecules and rare gases, including $^{13}C/^{12}C$ and $^{126}Xe/^{128}Xe$.[30-32] Using GC Orbitrap and Q Exactive HF models, measurement precisions of ~0.001% RSD were obtained. Furthermore, they presented a detailed discussion of figures of merit and limitations due to isotope discrimination arising from sample delivery, ionization and transfer, mass filtering, and detection.[30] Isotopic discrimination has been also noted in works by Hoegg *et al.*, largely attributed to the automatic noise deletion step employed in Orbitrap mass spectrometers.[11, 28] Recently, work by Bills *et al*. has utilized an advanced data acquisition system which alleviated the noise deletion step and collection of longer transient lengths.[33] This combination demonstrated that higher accuracy uranium IR measurements could be performed, while also providing mass resolution far surpassing the standard capabilities of the Q Exactive Focus; $m/\Delta m$ >1 M vs 70 k.[33]

In this work, the LS-APGD is interfaced with a Q Exactive Focus Orbitrap mass spectrometer which, like previous works, contains a quadrupole bandpass filter for mass

range pre-selection while also providing robust collisional dissociation methods. As a solution-based, atmospheric pressure plasma, the LS-APGD produces a variety of solvent-related analyte and background species which may lead to issues regarding dynamic range, mass resolution, and isotopic discrimination; all issues inherent to orbitrap mass analyzers. To this end, in-source collision induced dissociation (CID) and higher-energy collisional dissociation (HCD) are evaluated for their abilities to breakdown solvent- and atmosphere-related analyte species taking the form of oxides, hydroxides, and dioxides. Additionally, the roles these parameters take in IR measurements are investigated relative to accuracy and precision. Furthermore, the transmission characteristics of the quadrupole bandpass filter are evaluated and used to arrive at optimal conditions for IR measurements. Updated isotope ratio measurement characteristics for various elements are presented and compared with those from earlier works. The results of these experiments are expected to bring insight into improving sampling/operating conditions with the LS-APGD/Orbitrap coupling, with the lessons learned perhaps having application to other MS instrument platforms.

6.2 Materials and Methods

6.*2.1 Source Design*

The practical aspects of the LS-APGD/Orbitrap pairing have been detailed in previous works.[11, 29, 34] The LS-APGD consists of a grounded solution electrode and a counter electrode, with a high voltage potential applied to it, between which a discharge is struck. The solution electrode is comprised of a fused silica inner capillary (250 μm I.D., 360 μm O.D.; Molex, Lisle, IL) and a stainless-steel outer capillary (0.4 in I.D., 1/16 in

O.D.; McMaster Carr, Elmhurst, IL). An electrolytic solution is delivered via the inner capillary at a rate of 30 μL min^{-1} from a Chemyx 100 syringe pump (Stafford, TX). Through the outer capillary, a cooling helium sheath gas is introduced by an Alicat (Tucson, AZ) mass flow controller at a rate of 500 mL min^{-1}. The counter electrode (anode) is a solid stainless-steel weldable feedthrough (MDC Vacuum Products, LLC; Hayward, CA) to which a constant current of 30 mA is delivered via a Spellman (Happauge, NY) SP60 high voltage power supply.

6.2.2 Mass Spectrometer System

The LS-APGD is interfaced to a ThermoScientific (San Jose, CA) Q-Exactive Focus by simply replacing the standard electrospray ionization source, requiring no modifications to the base instrument. The experimental components of note are highlighted in Fig. 6.1. Unless stated otherwise, data was taken in a method analogous to previous works by Hoegg *et al*., where each data point represents a series of three, averaged acquisitions.[11] Acquisitions are made up of 100 scans, where each scan consists of 10 microscans. A microscan is the discrete injection of an ion packet from the C-trap into the orbitrap (note, when referring to the analyzer cell, there is no capitalization of the word), from which a transient signal is recorded. Once the 10 microscans are collected, the transients are averaged together and a Fourier transform is applied (converting from the time to frequency domain), and subsequently converted to a mass spectrum/scan. Based on previous works,[11] the automatic gain control, which controls the number of charges that

are allowed into the C-trap, is set to 1 x 10^6 charges with a maximum injection time of 100 ms. Peak area data was extracted via the Thermo Xcalibur Qual Browser software.

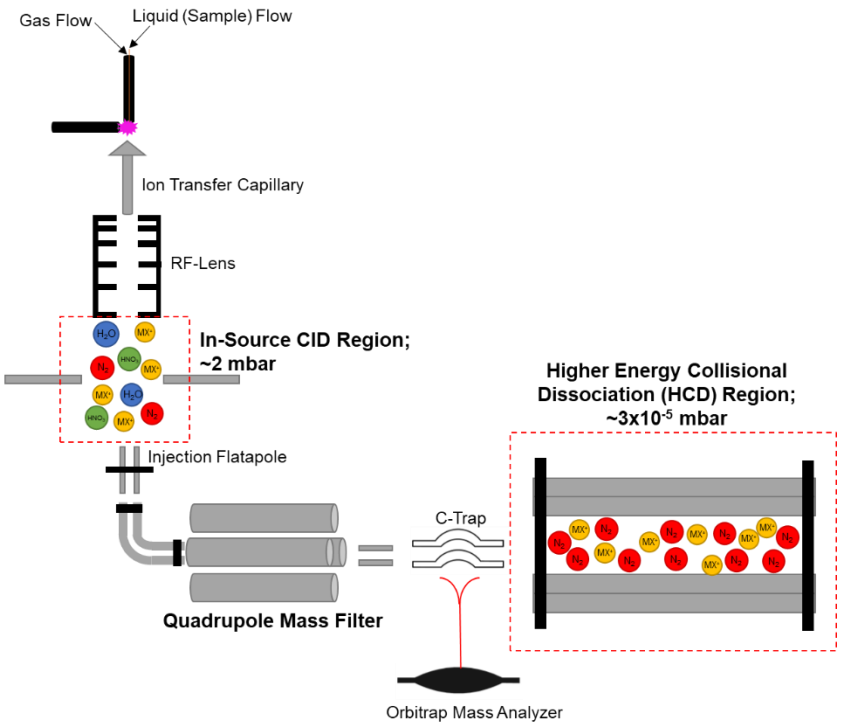

Figure 6.1: Diagrammatic representation of the LS-APGD interfaced with a Q Exactive Focus mass spectrometer, highlighting the components of relevance in these studies.

6.2.3 Sample Preparation

For the experiments presented in this work, all samples were prepared in a 2% HNO_3 solution. Elemental standard solutions (Pb, Ba, La, Ce, Nd, Rb, Ag, Sm, and Tl) were obtained from High Purity Standards (Charleston, SC) and individually diluted to a final concentration of 5 µg mL^{-1}. Xenon was obtained as a mixture of 1000 ppm-by-volume Xe in He from Airgas (Cinnaminson, NJ) and was introduced with the sheath gas flow. U was obtained as a certified standard, CRM-129a (New Brunswick Lab, Lemont, IL) with a certified value of $^{235}U/^{238}U$ = 0.007289 and prepared at 500 ng mL^{-1}. As described in

previous work, all U analyses were performed by monitoring the dioxide cation of uranium (UO_2^+), which is the dominant form of U species in acidic solutions as in the product LS-APGD mass spectra.[11]

6.3 Results and Discussion

6.3.1 Methods of Collisional Dissociation - Effects on Spectral Composition

Collisional dissociation methods are most common to "organic" MS and are typically utilized towards the reduction of molecular (solvent) background species or for fragmentation of analyte ions towards identification and structural elucidation.[35, 36] Solvent-related analyte clusters as well as background species are formed in the LS-APGD, complicating spectra and hindering some measurements. Past works in this group briefly explored collisional dissociation as a method of reducing these species, suggesting its importance towards isotope ratio measurements.[28] Early work towards the measurement of U isotopes with the LS-APGD utilized an Exactive Orbitrap containing no quadrupole band pass filter, so any ions generated by the microplasma source and sampled into the spectrometer vacuum system were transmitted via the C-trap to the orbitrap. Because trapping MS performance is limited by the fraction of the analyte ion density that is collected in the analyzer, removing molecular species before entry to the C-trap increases the fraction of analyte ions entering the analyzer, improving sensitivity.[37] Additionally, by reducing the number/type of concomitant species collected, their contribution to the measurement noise is minimized, improving analyte signal-to-noise characteristics.

The present Q Exactive Focus platform provides two means to affect the dissociation of molecular species, as highlighted graphically in Fig. 6.1. First, in-source

CID is affected by the application of a DC offset potential between the exit of the RF-lens and the injection flatapole. In this way, charged species are accelerated through a relatively-high pressure region (~2 mbar) where collisions with background gases affect dissociation. Past experience in this laboratory suggests that this modality of CID is most impactful in the depletion of background solvent species (e.g., water clusters) and the dissociation of waters of hydration of analyte species (e.g., $M+(H_2O)_x$). The second modality, higher energy collisional dissociation (HCD), relies on a pressurized (~$3x10^{-5}$ mbar) octapole assembly to affect CID using N_2 as the target gas. Here, the greatest benefit is realized in the dissociation of the molecular forms of analyte species such as oxides, hydroxides, and salts.

When discussing the effectiveness of these collisional modalities, it is useful to consider the energy that is available for collisional dissociation, the center-of-mass energy (E_{cm}) which is defined as

$$E_{cm} = E_{lab}\left(\frac{m_c}{(m_i + m_c)}\right)$$

where E_{lab} is the applied potential in either the in-source CID or HCD regions, m_c is the mass of the collisional gas, and m_i is the mass of the specific molecular ion being dissociated.[35,36] (Note, through the remainder of this work, the E_{lab} potential is referred to as either the in-source CID potential or the HCD potential). For dissociation to occur under single-collision conditions, the applied potential must be sufficient to ensure E_{cm} reaches the bond dissociation energy (D_0) of the target ion. Of course, as has been detailed in previous studies on collisional dissociation, E_{cm} represents the kinetic energy that is *available* to be converted into internal energy upon a collision event. The actual energy

that is internalized by the target ion may influenced by additional factors including the realization of multiple collisions, extended activation times, etc. In the present work, the instrument platform does not afford the ability to alter the target gas identity or pressure, only the dc offset potentials are controllable variables.

As a demonstration of the effectiveness of these two methods, Figs. 6.2a - c present the product mass spectra for Pb species as a function of the in-source CID and HCD energies. In the first case, ions pass from the C-trap to the orbitrap analyzer, without transiting to the HCD cell; i.e. only in-source CID is implemented. As shown in Fig. 6.2a, $Pb(NO_3)^+$ and $Pb(NO_3)(H_2O)^+$, arising from analyte-solvent interactions with the 2% HNO_3 solvent system, are prominent in the lower-energy CID spectra (upper portion of figure). As expected, a large number of background, solvent-related species are also present across the spectral region, which would be problematic in analyses performed on lesser-resolution mass analyzers. (The mass spectrum corresponding to the case of no-CID is affected is far more complex, with 2X greater intensities.) While these background species have not been fully characterized, preliminary investigations performed on a triple quadrupole platform indicate that the vast majority of background species are solvent related, with water/acid adducts being the most prevalent.[21] The specific region in the vicinity of the target atomic Pb ions shows appreciable amounts of background species. As the in-source CID potential is increased in intervals of 10 V, the noted species are readily dissociated down to unobservable levels relative to Pb^+ and $PbOH^+$ species. While the relative Pb^+ appear to be poor, for reasons described below, the atomic Pb^+ response actually increases by ~5x, across this range of CID potentials. This increase, versus the loss of the solvent-related

species, arises from a combination of those species dissociating down to the Pb^+ and $PbOH^+$ as well as the reduction of background species.

a.

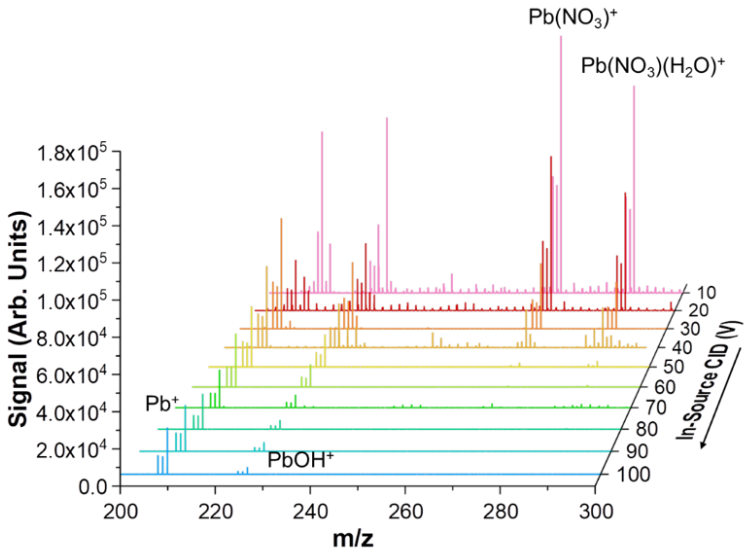

b.

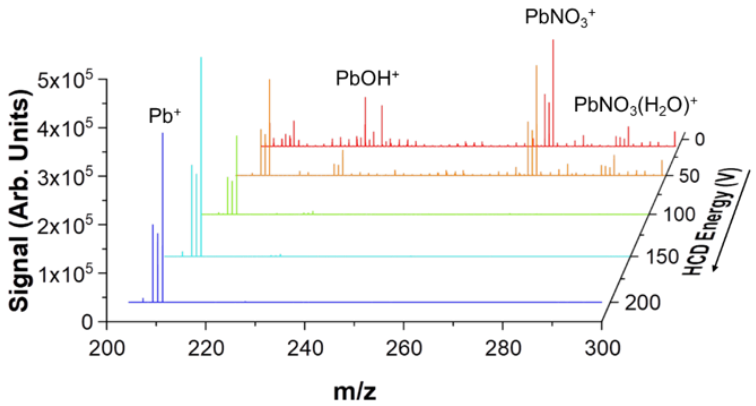

c.

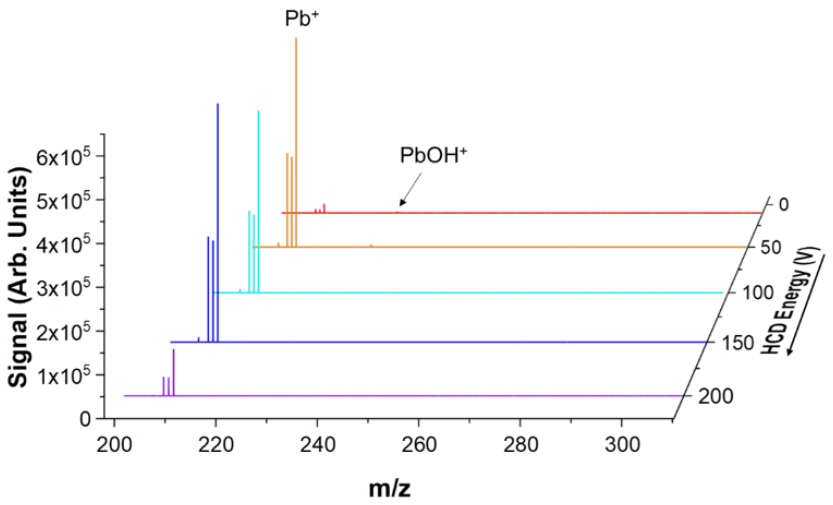

Figure 6.2: Breakdown of Pb species at 5 µg mL^{-1} as a function of increasing a) in-source CID energy (V) and no HCD is employed, b) HCD energy (V) when the in-source CID energy is set to 0 V, and c) HCD energy (V) when in-source CID energy is set to its maximum (100 V).

While not quantified, previous studies indicated that there was also benefit in the use of the HCD process to reduce the contributions of molecular ions in the LS-APGD mass spectra.[28] Figure 6.2b demonstrates the effects of HCD energy when no in-source CID is applied. In this case, ions pass from the C-trap to the HCD cell, where they undergo collisional dissociation before being returned to the C-trap and are then sent to the orbitrap analyzer. As shown in the figure, the levels of observed dissociation at the 50 V potential roughly reflect what is shown in Fig. 6.2a for 40 V in-source CID, noting the further dissociation of NO_3-related species down to unobservable levels at 100 V. In this case however, the applied energy can be increased up to 200 V, at which point the remaining $PbOH^+$ species are near-completely dissociated. Interestingly, at 50 V of applied potential,

the equivalent E_{cm} for $PbOH^+$ is ~530 kJ mol^{-1} which exceeds D_0 (350 kJ mol^{-1}). This lack of complete dissociation provides insight into the efficiency of the HCD modality. Non-quantitative dissociation may occur for a number of reasons such as multiple collisions relaxing internal energy distributions (i.e., collisional cooling), insufficient activation times, insufficient target gas pressure, etc.[38] Increasing the HCD potential (E_{cm}) substantially improves the efficiencies. It should be noted, that increasing the HCD beyond 150 V to its maximum value results in a decrease in the atomic Pb^+ signal, stemming from collisional scattering losses from the cell.

When comparing Figs. 6.2a and b there a few operational differences that must be taken into account. Particularly, in Fig. 6.2a the dissociation from $Pb(NO_3)^+$ and $Pb(NO_3)(H_2O)^+$ to Pb^+ and $PbOH^+$ appears to only have ~10% recovery, in comparison to Fig 6.2b, where the conversion to Pb^+ appears to be closer to 100% efficient using HCD. In this Orbitrap platform, the HCD is enabled in the MS/MS scanning modality, where the quadrupole operates as a mass/bandpass filter. When the HCD is disabled, the full scan modality, the quadrupole acts in an rf-only mode to facilitate the transport of all ions to the C-trap. This is the case in Fig. 6.2a, where only the in-source CID is enabled. As a result, all ions remaining from the in-source CID process (inclusive of dissociation fragment ions) are counted towards the 1×10^6 AGC target, serving to limit the number of Pb ions detected. On the other hand, when implementing HCD the full range of the ACD is focused on the target ions passed through the quadrupole. In this case, it is clear that the overall conversion efficiency is very high based on the ion signal recoveries.

As a means to fully dissociate molecular analyte species without throughput losses, in-source CID and HCD energies can be employed in tandem. In Fig. 6.2c, the effects of the HCD energy are demonstrated for the case of maximum in-source CID energy (100 V), beginning at the lowest value HCD potential of 10 V (a 0 V value is not an option). While small amounts (~20%, relative) of the $PbOH^+$ are visible on the plotted scale at the lowest HCD energy, only the Pb^+ atomic ions are detected at HCD settings of 100 V and greater. As noted above, the E_{cm} exceeds D_0 for $PbOH^+$ by ~1.5x at 50 V, however, at 100 V where E_{cm} ~ 3x D_0, and complete dissociation is realized, Of course, the full dissociation of $PbOH^+$ may occur at a value between those 50 V and 100 V.

A more mechanistically subtle, yet practically pronounced, benefit of the breakdown of the various background/molecular species involves the vastly improved sensitivity towards the desired Pb^+ ions under conditions of consistent AGC/injection time settings. With only in-source CID energy employed, the maximum signal for $^{208}Pb^+$ is ~$2x10^4$, once the full complement of in-source and HCD processes are applied, the atomic ion signal increases by over an order of magnitude. Looking at the species that exist post in-source CID, the conversion of molecular species into atomic form fails to fully explain the increase in signal intensity. Rather, this increase stems from the ion population entering the orbitrap for detection being made-up solely of Pb^+ as opposed to molecular analyte species and background solvent related species. With continual increase in the HCD energy to its maximum value, collisional scattering losses become so prominent that the lowest-abundance ^{204}Pb isotope is not visible on this scale, as such 150 V dissociation is preferred. In agreement with previous works, the collisional dissociation methods employed on this

platform not only simplify the spectral composition, but also improve the sensitivity of the measurement of target species.[28] To be clear, this latter effect is of far greater importance on the Orbitrap MS platform as each of the atomic Pb^+ species are easily identified based on the operating resolution of the instrument, even without the use of any collisional dissociation.

6.3.2 Methods of Collisional Dissociation - Effects on Isotope Ratio Precision

While reducing concomitant species is important for improving sensitivity and overall quantification, of equal interest is how collisional dissociation affects IR measurement performance. The fact that molecular background species might have different temporal/noise characteristics makes their potential influences on measurement precision a concern. Looking at the inter-scan isotope ratio precision can reflect what effect the dissociation conditions (and the product spectral characteristics) have on IR measurements. In Fig. 6.3a, the Pb isotope ratios ($^{204}Pb/^{208}Pb$, $^{206}Pb/^{208}Pb$, and $^{207}Pb/^{208}Pb$) are plotted together, where each data point represents the isotope ratio measurements obtained from one scan. For each in-source CID condition, the results of 25 scans (taken over ~0.5 s) are plotted for the CID energies of 10, 30, 50, 70, and 100 V. These IR measurements are taken analogous to previous studies, where the reduced quadrupole filter and Orbitrap digitization range are employed to minimize concomitant ion effects and flicker noise respectively. In the ideal case of no mass bias and no temporal drift, a single point would exist at the centroid of the 3D plot. The data clearly demonstrate that when little collisional dissociation is applied, the scan-to-scan IR variation is considerable (~20% RSD for 10 V). Importantly, the observed microplasma discharge voltage stability (±2%)

and the total ion current (~7% RSD) under these conditions suggests that the source of the variability (i.e., flicker noise) exists outside of the discharge region/processes, perhaps from the interaction of Pb with solvent-related species in the gas-phase sampling process. As the CID energy is increased, the case where the majority of molecular related species are dissociated in the expansion region, the data points begin to cluster, reaching a value of ~2.2% RSD at the 100 V setting. Based on the random distribution of values across the three axes, there is no particular bias in the actual IR values across the three isotopic pairs. In most observed cases of isotopic discrimination in trapping-type analyzers, there is a bias towards a certain ion, typically the heavier ion,[39] whereas here the variability appears random. Likewise, bias stemming from kinetic isotope fractionation, where the gas phase recombination of Pb^+ and solvent ions would experience slightly different reaction rates, would be expected to be present in the data, if it existed.[40] What is seen in the data plotted in Fig. 6.3a is a situation where increases in the in-source CID energies provide greater temporal stability of the ion beam captured in the C-trap and introduced to the orbitrap analyzer. This would suggest the effects of two different phenomena as sources of IR imprecision. The first would be related to the formation of those species in the expansion region between the ITC and the skimmer, where longer transient times at low voltages create greater variability. Alternatively, the higher energy collisions at elevated potentials may homogenize/randomize the temporal behavior of the ions introduced to the C-trap.

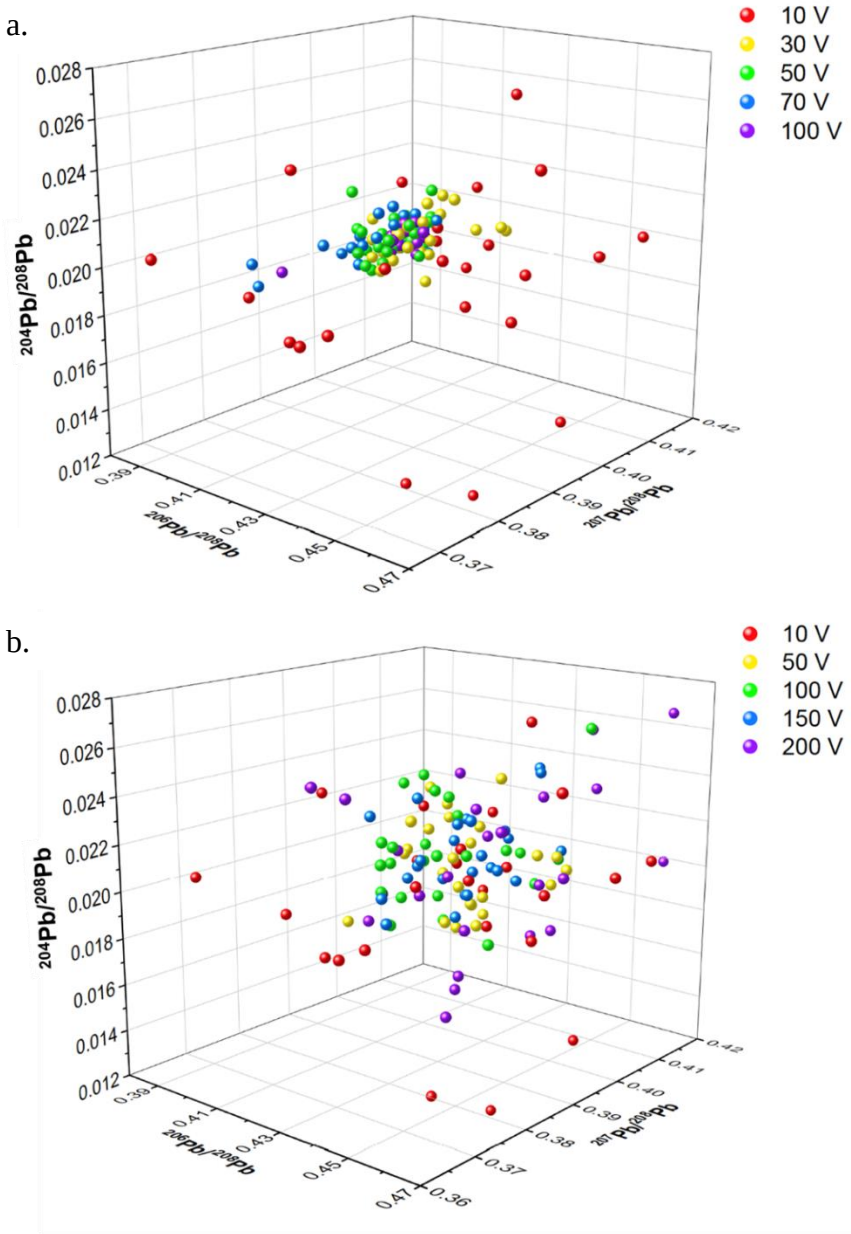

Figure 6.3: 25 scans of $^{204}Pb/^{208}Pb$, $^{206}Pb/^{208}Pb$, and $^{207}Pb/^{208}Pb$ at 5 µg mL^{-1} plotted against each other with increasing a) in-source CID and b) HCD

Affecting the collisional dissociation of molecular ions via the HCD cell provides insights into the observations regarding in-source CID. In this case, use of increasing HCD energies from 10 to 200 V, *in the absence of in-source dissociation* yields no improvements

in either IR precision or accuracy as reflected in the distribution of data points in Fig. 6.3b. While HCD was shown in Fig. 6.2b to substantially reduce the preponderance of Pb oxide/hydroxide species while improving the overall Pb isotopic sensitivity, there was virtually no difference in the scatter in the responses with increasing HCD energy versus what was seen for the lowest-energy in-source dissociation step alone (Fig. 6.3a). As the AGC settings, which set the number of ions transmitted to the HCD cell, were the same as for the in-source dissociation experiments, potential concerns about the absolute numbers of ions impacting precision are alleviated. Indeed, the improvements in the accuracy of the Pb IR values are minimal as the energy is increased. Thus, the processes occurring in the HCD cell have no effect on the temporal variability of the analyte signals, while those in the ITC region serve to suppress temporal variations in the ion populations extracted from the plasma and sampled into the mass spectrometer. Simply put, the in-source CID provides an additional means for homogenizing and collisionally cooling the incoming ion beam to reduce flicker noise, whereas the HCD processes haven no impact on this noise component. That said, it is clear that when acting in tandem with in-source CID, the HCD energy becomes a powerful approach to dissociation of molecular species and in boosting sensitivity. In the remainder of this work, in-source CID is set to its maximum value of 100 V, and the HCD energy is operated at 150 V to breakdown molecular-form analyte species without the detrimental effects of collisional scattering.

6.3.3 Effectiveness of HCD Processing for Dissociation of Metal Oxides/Hydroxides

In addition to adduct species which may be formed, such as NO_3 and H_2O clusters, there is a diversity of analyte-containing molecules such as oxides, dioxides, and

hydroxides which reflect solution phase chemistry (either in the bulk or droplets).[22] Not surprisingly, the presence of these species in the LS-APGD mass spectra (as molecular ions) tends to increase for the higher-mass (d- and f-electron) metals and small highly charged metals (Mg or Ca), although the specifics of formation have not been thoroughly examined. As demonstrated, in-source CID is more effective in removing/alleviating solvent-related ions, while the conditions under which the HCD operates are necessary to break down metal oxides, etc (e.g., $PbOH^+ \rightarrow Pb^+$). These species have higher bond dissociation energies and require the higher E_{lab} values and thus E_{cm} available from HCD to potentially reduce them to bare atomic ions.[41-45]

The efficiency of the HCD process in dissociating oxide/hydroxide species produced in the microplasma source was evaluated for the metals Ba, La, Ce, Nd, and U. (These same species have long been documented to be systemic in ICP-MS.[46]) The bond dissociation energies for their corresponding oxides/hydroxides are presented in Table 6.1. While the mass resolution here is sufficient to alleviate virtually any isobars, their remediation has positive consequences in terms of analytical sensitivity, and perhaps IR performance. As demonstrated in Fig. 6.2b, although $PbOH^+$ survives in-source CID and enters into the HCD cell, the E_{cm} values achieved in the HCD cell exceed D_0 for $PbOH^+$ by nearly 6x at the highest HCD potentials.[45] Barium represents another example of a metal that presents itself predominately in the hydroxide form in the native LS-APGD mass spectra, having a slightly higher bond dissociation energy than the Pb species (D_0 = 477 vs 350 kJ mol^{-1}).[42] Figure 6.4a represents the breakdown of $BaOH^+$ into atomic Ba^+ as a function of HCD energy, where the vertical black line represents the potential required for

E_{cm} to match D_0 for $BaOH^+$. At 50 V, fragmentation of $BaOH^+$ is observed, although a significant quantity of $BaOH^+$ remains. As shown in this figure, $BaOH^+$ requires high HCD potentials, and thus high E_{cm} values, to achieve high degrees of dissociation. At that potential, the observed hydroxide ion population has been reduced by approximately one order of magnitude, while the corresponding metal ion response increased by about 3 orders of magnitude, reflective of its very low initial abundance. At the highest HCD potential, E_{cm} exceeds D_0 by ~6x, though complete dissociation is not achieved, and increased scattering reduces the intensity of both species. Figs. 6.4b and 6.44c represent spectra obtained at the minimum HCD energy (10 V) and the optimum (150 V) settings, where it can clearly be seen that the HCD energetics dissociate the $BaOH^+$ (and other concomitant molecular species) in large part. In the lower-energy case, a large number of background species are present, which are also readily alleviated at the higher energy. Based on the total recoveries of the $^{138}BaOH^+$ and $^{138}Ba^+$ signals (shown as the green trace in Fig. 6.4a), the efficiency of this process is ~90%, in terms of the molecular ion being converted to the bare metal ion. Importantly, the average error of the IRs for the Ba isotopes having relative abundances of >0.03 relative to the ^{138}Ba isotope are less than 3% relative, for what are basically "survey scan" conditions.

a.

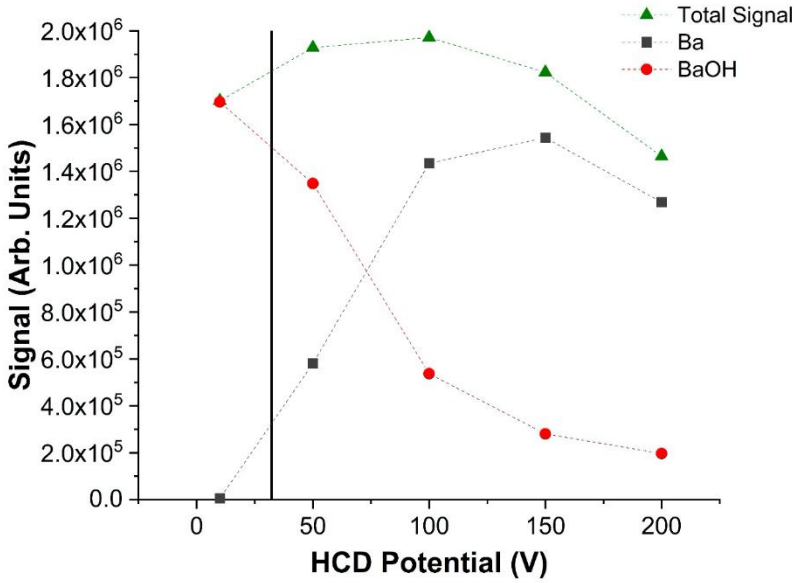
Total Signal
Ba
BaOH
Signal (Arb. Units)
2.0x10^6
1.8x10^6
1.6x10^6
1.4x10^6
1.2x10^6
1.0x10^6
8.0x10^5
6.0x10^5
4.0x10^5
2.0x10^5
0.0
0
50
100
150
200
HCD Potential (V)

b.

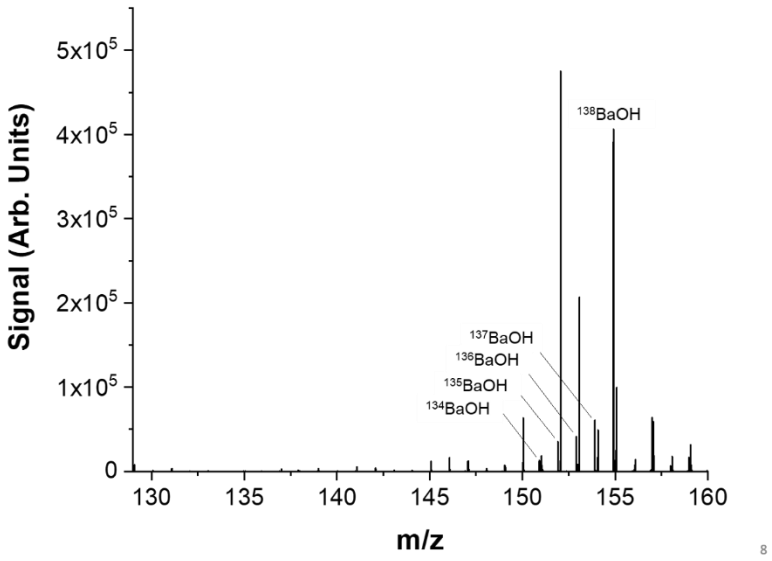
Signal (Arb. Units)
5x10^5
4x10^5
3x10^5
2x10^5
1x10^5
0
138BaOH
137BaOH
136BaOH
135BaOH
134BaOH
130
135
140
145
150
155
160
m/z

8

c.

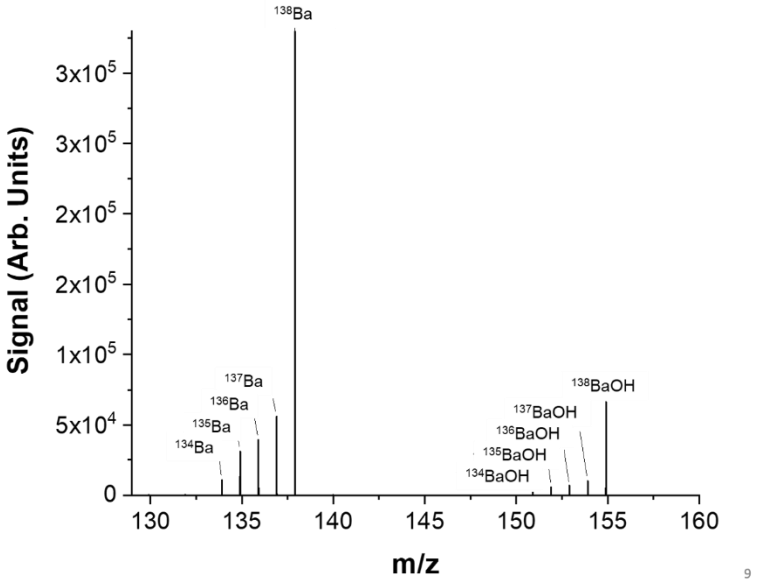

Figure 6.4: a) $^{138}Ba^+$, $^{138}BaOH^+$, and the summed total signal at 5 µg mL^{-1} as a function of increasing HCD energy. In-source CID is set to a maximum of 100 V, where the vertical black line represents the potential required for E_{cm} to equal D_0 for $BaOH^+$. b) Spectrum with no in-source CID or HCD energy applied and c) spectrum with 100 V in-source CID and 150 V HCD.

The fact that $PbOH^+$ fully dissociates while $BaOH^+$ does not is reflective of the higher M-O^+ bond dissociation energy of the latter, as listed in Table 6.1. Reported as well are the determined M^+/MX^+ values (where X is the associated oxide/hydroxide) for a number of other species as a function of the applied HCD potential, demonstrating the improved efficiencies realized. Clearly seen as well is the fact that there are fundamental limits to the amount of energy that can be coupled to affect dissociation. Figure 6.5 depicts the determined M^+/MX^+ values obtained at the maximum HCD setting as a function of the MX^+ bond dissociation energies. Due to the large differences in ratios, this data is plotted with the y-axis on a log scale, and both La^+/LaO^+ and U^+/UO_2^+ omitted because their free metal (M^+) responses could not be measured (The value for UO^+/UO_2^+, representing the

loss of one oxygen atom, is included as a point of comparison.). At this HCD potential, E_{cm} exceeds D_0 for all analytes listed in Table 6.1, and as has been discussed, the results reflect the inefficiency of HCD processes (limited by the very low target gas pressure) resulting in diminished levels of dissociation for analyte-oxide species having higher D_0 values.

Table 6.1: Ratio of M^+-to-MX^+ for a variety of samples which form atmosphere related species. Analytes are listed by increasing bond dissociation energy and M^+/MX^+ is given for increasing HCD energies. ND = non-determinable due to low M^+ intensities.

Element	Species Dissociated	*Species Formed*	*M-X Bond Dissociation Energy (kJ mol^{-1})*	*Ratio of M/MX^+ at Different HCD Potentials (V)*				
				10	50	100	150	200
Pb	PbOH	Pb	350	6.3	93.2	456	756	1191
Ba	BaOH	Ba	477	0.003	0.43	2.67	5.50	6.50
U	UO_2	UO	618	0.0018	0.0019	0.0018	0.0018	0.0014
Nd	NdO	Nd	749	0.00052	0.00053	0.00056	0.00051	0.0005
Ce	CeO	Ce	849	0.00013	0.00021	0.00022	0.00015	0.00014
La	LaO	La	875	ND	ND	ND	ND	ND
U	UO_2	UO	1334	ND	ND	ND	ND	ND

Analogous dissociation studies have been performed on quadrupole ion trap (QIT) instruments, using electron ionization to produce polyatomic ions as well as glow discharge sources which produced diatomic metal oxide species.[41, 47, 48] A main focus of those metal oxide studies, was the dissociation of the strongly bound diatomic ion TaO^+ (D_0 = 790 kJ mol^{-1}), of which dissociation yields approaching 100% were obtained through tuning of the resonance excitation frequency and amplitude, as well as the bath gas composition and pressure.[49] On the other hand, work by King and Harrison demonstrated the dissociation of TaO^+ (D_0 = 10.3 eV) using the collision cell of a triple-quadrupole mass spectrometer, achieving ~25% dissociation using an Ar bath gas and E_{cm} of ~16 eV.[48] The HCD cell on

the Orbitrap instrument operates most similarly to a triple-quadrupole collision cell, though by use of an offset potential (0-200 V) and an N_2 collision gas. Metal oxide species having similar dissociation energies to TaO^+ (NdO^+ and CeO^+) analyzed in the present work, were only dissociated to the atomic ion to the fraction-of-a-percent level in the HCD cell. Indeed, the name HCD is misleading based on the process, relying on relatively low energy collisions. The 'higher' in higher energy collisional dissociation refers to the higher radiofrequency voltage applied to retain fragment ions with higher efficiency rather than the energy of the collisions.[50-52] Although there is a limitation to which metal oxide/hydroxide species can be fully dissociated, the work on U isotope ratio analysis by Hoegg *et al.* has always utilized UO_2^+ for measurements, obtaining precision values of <0.086% RSD,[15, 28] demonstrating the practical utility of using molecular species in IR determinations. Indeed, as the resolution of the Orbitrap allows for unambiguous species assignment, it is inconsequential whether the analyte exists in either atomic or molecular (oxide/hydroxide) forms, it is just preferred that the analyte be exclusively in that state. Furthermore, the sensitivity of these measurements is still extremely high, utilizing analyte concentrations of only 100 ng mL^{-1}, representing isotopic measurements at the pg level. Ultimately, the efficacy of the HCD process is to reduce all of the species of a given analyte into a single form, whether it be atomic, monoxide, or dioxides.

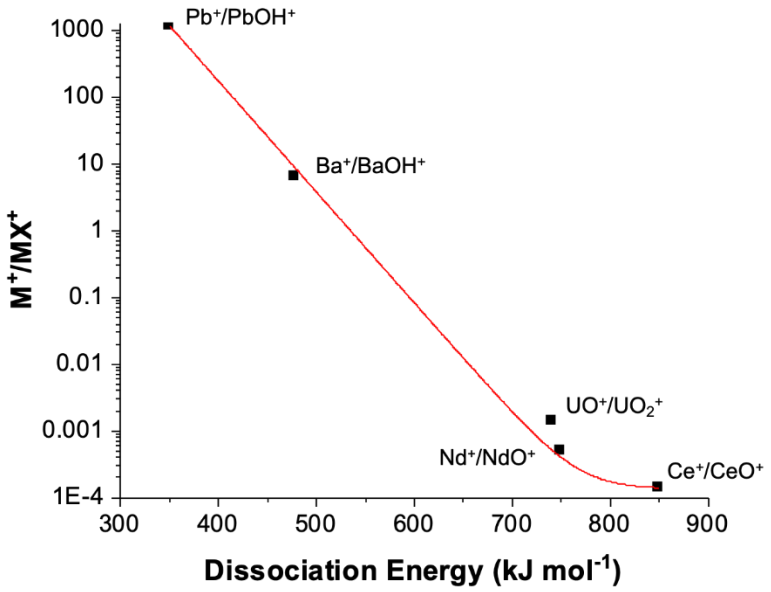

Figure 6.5: Measured M^+/MX^+ ratio (X = O, -OH, or O_2) vs. bond dissociation energy determined at the most energetic dissociation conditions, CID = 100 V and HCD = 200 V.

6.3.4 Effects on Signal Digitization and Quadrupole Window Breadths

Work by Hoegg *et al*. studied the effect of the Orbitrap signal digitization window (i.e., the mass range to which the Fourier transform is applied) on the accuracy and precision of the $^{235}U/^{238}U$ measurement.[11] Smaller digitization windows were ultimately found to provide the best accuracy. Variations in measured ratios across different windows were attributed to either space charge effects or the distribution of noise across the spectrum stemming from the FT processes. Additional work by Hoegg *et al*. briefly demonstrated the effects of changing the quadrupole band pass on isotope ratio precision and accuracy using Q Exactive Orbitraps.[28] That work demonstrated the measurement of $^{235}U/^{238}U$ in a solution containing Rb, Ag, Ba, Pb, and U, and how reducing the bandpass window to

allow only U species to pass on to the C-trap, yielded higher precision and accuracy IR measurements. By limiting the quadrupole bandpass window, only the analytically-relevant portion of ion population reaches the orbitrap analyzer.

Another important factor that should be considered when setting the quadrupole mass range however, is the effect the set range may have on analyte transmission. In a typical scanning quadrupole mass analyzer, the transmission of an ion depends largely on the resolution utilized and the number of RF cycles experienced by the ion in the quadrupole field (fringe fields). Additionally, the scan cycle speed creates tradeoffs between sensitivity and resolution with high scan speeds leading to unfavorable ion counting statistics.[53-55] In RF-only quadrupole assemblies, mass discrimination can also arise across smaller mass ranges due to spatial focusing effects.[54] Drift in the transmission of analyte ions may also impact measurements, however on this platform, extended IR measurements show that it is not influential towards transmission.[9] Lastly, quadrupole filters can demonstrate reduced ion transmission at masses approaching the edges of a set range as a result of the transition between the pass-and-stop bands of operation.[56] These may have detrimental effects on measurements where high levels of precision are required. The roles of these parameters are evaluated here with respect to uranium IR performance.

Different from previous efforts that did not provide for HCD processing, the quadrupole filter passes ions to the C-trap, and on to the HCD cell for further dissociation, prior to reinjecting them into the C-trap and on to the orbitrap. As such, the passage of higher mass species, which are subsequently dissociated down to the target analyte forms can be employed advantageously (e.g., Fig. 6.2). Figure 6.6 depicts the effects of both the

quadrupole bandpass and signal digitization ranges on the $^{235}U/^{238}U$ measurement accuracy and precision, with the respective ranges centered between the dioxide ions of the two isotopes (268.5 Da). The two variables were assessed independently, holding the other value constant at the 50 Da mass range of 243.5 – 293.5 Da. Looking first at the role of the digitization range, decreasing the window has a small but positive effect on the IR accuracy but demonstrating a significant improvement in the measurement precision, being reduced from 0.41 to 0.11 %RSD. The improvement in precision is entirely related to how signal is processed in Fourier transform (FT) instruments. The transient signal that is collected is based on the ions that are allowed into the orbitrap cell, with the digitization window defining which ions' contributions are subjected to FT. In multiplex systems such as the Orbitrap, the total noise is affected by the sum of the signals from all spectral channels, meaning that noise in the frequency-domain (flicker noise) is distributed across the entire spectrum. In general, this can lead to enhancements in the signal-to-noise ratio (SNR) for abundant species, while simultaneously decreasing the SNR for small peaks, a multiplex disadvantage.[57] As such, while the accuracy of the measurement does not change appreciably as a function of the digitization window width, the precision of the measurement improves as the window is narrowed and less "irrelevant" noise is propagated across the spectrum and particularly to the minor (^{235}U) isotope. Although a mass window of 5 Da achieves the best measurement precision in what was employed here, this range would not be suitable for ratio measurements of analytes with more isotopes (i.e. Ba, Nd, etc.). Ultimately, it would be standard procedure to optimize the digitization window for each application at hand.

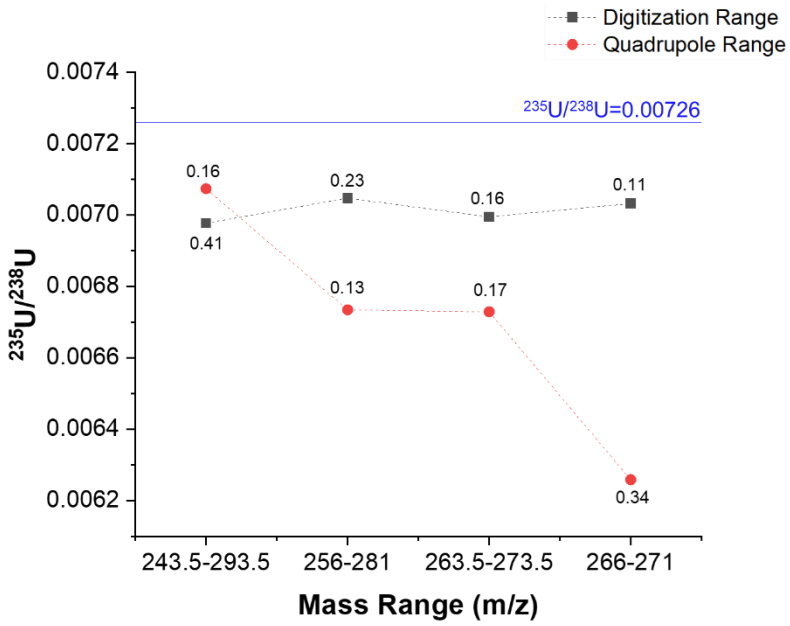

Figure 6.6: $^{235}UO_2/^{238}UO_2$ as a function of digitization and quadrupole transmission range where CRM 129-a ($^{235}U/^{238}U$ = 0.00726) is used at a concentration of 500 ng mL^{-1}.

The effects of the quadrupole bandpass window depicted in Fig. 6.6 present an opposing case to the digitization window. While previous work looked at using the quadrupole window to remove concomitant ions which were 10s of Daltons removed (Rb, Ag, Ba, and Pb), it did not look at how that window breadth affects ion transmission and its potential influence on IR bias.[28] As is shown in Fig. 6.6, narrowing the quadrupole window begins to degrade not only the accuracy of the measurement, but the precision as well. The loss in accuracy here is largely biased against the minor isotope, as the value for the $^{235}U/^{238}U$ ratio decreases. A primary aspect here is that the quadrupole mass filter is placed prior to introduction to the C-trap, where limiting the mass window limits the higher mass ions entering the HCD cell; ions which might be further dissociated to the species of analytical interest (UO_2^+). The loss of these U species (in even the second quadrupole

setting of 256-281 Da) reduces the total signal attributed to UO_2 in the final spectrum. In fact, a plot of the $^{235}UO_2^+$ and $^{238}UO_2^+$ signals as function of the mass window shows an initial drop of ~50%, and eventually ~75% as the window breadth is further decreased. As suggested by the determined IR values in Fig. 6.6, the $^{235}UO_2^+$ signal is more suppressed in this process. As noted in previous efforts,[9, 11] the automatic noise deletion step utilized by this platform effects the lower-abundance species far more so than the major isotope which is present at an excess of 100x. Likewise, the reduced isotopic responses also serve to degrade the measurement precision. Ultimately, the quadrupole transmission window must be balanced in terms of filtering out concomitant species which decrease sensitivity and precision, while also allowing for the HCD dissociative production of contributors to the desired signals. For the case of uranium isotopic analysis, a quadrupole band pass of 50 Da and a digitization window of 10 Da were chosen for optimum IR measurements, yielding a relative error of 3.7% and a precision of 0.16% RSD, an improvement of 1.5x and 8.5x respectively over previous Q Exactive performance.[34] This mass error is realized without the use of any external standards. It should be noted, that while these precision results easily meet the IAEA ITV's, they are not the best results obtained on an LS-APGD/Orbitrap platform. Indeed, previous works by Hoegg *et al.* have demonstrated measurement precisions as low as 0.075% RSD.[15, 28] The important distinction between these works is that the more precise measurements are obtained on an Orbitrap Fusion Lumos Tribrid platform collecting higher resolution ($m/\Delta m$ = ~120,000 obtained by virtue of longer signal transients) and greater numbers of measurements, resulting in improved measurement precision.[23] The platform employed here, the Q Exactive Focus, is in fact the

"entry level" Orbitrap system and can still perform these isotope ratio measurements with a high degree of precision.

Beyond the role of limiting which ion populations are passed to the C-trap, the HCD, and eventually to the orbitrap analyzer, one must also be concerned with the uniformity to which the desired ions are transmitted through the quadrupole assembly. It is important to note that the quadrupole mass filter used in the Q Exactive Series Orbitrap platforms is not a scanning quadrupole as typically used in quadrupole mass spectrometers, but rather it is used solely as a band-pass filter.[58] The respective poles of the quadrupole correspond with high and low pass filters, attenuating any incoming ions that do not sit inside the set range. The decrease in transmission of ions which sit at the edge of the "pass" range is a common characteristic of band-pass filters,[53, 54] including electronic and digital signal processing.[56, 59] Filters are comprised of stop bands, where no ions are passed, a pass band, where ions of the selected masses are passed, and transition bands between the two regions allowing a transition between the stop and pass bands.[53, 54] Simply, there is no 1-or-0 situation for ion transmission, unfortunately leading to reduced (and irregular) transmission at the edges of the set mass window.

The effects of slewing the center of the quadrupole window are demonstrated in Fig. 6.7, where the digitization range is held constant (10 Da) and the center point of the quadrupole range is stepped across the three response regions for the $^{235}UO_2$ and $^{238}UO_2$ ions. The quadrupole transmission band characteristics are illustrated for the case of a 50 Da band pass in Fig. 6.7a, with the center of the window stepping across the relevant mass range. Moving from lower to higher masses, the response of the $^{235}UO_2$ (m/z=267)

increases dramatically as the center point passes 242 Da (red line) with the $^{238}UO_2$ exhibiting a step-function increase as the center point crosses 245 Da (blue line). The respective signals show corresponding drops in intensity as the center points extend 25 Da beyond the isotopic masses. Importantly, the response profile of each isotope tends to show a maximum appearing roughly at the point the isotope is centered within the field. This suggests that the band-pass filter never yields a truly "flat-top" transmission characteristic, but indeed shows somewhat better transmission at center of the pass band.

a.

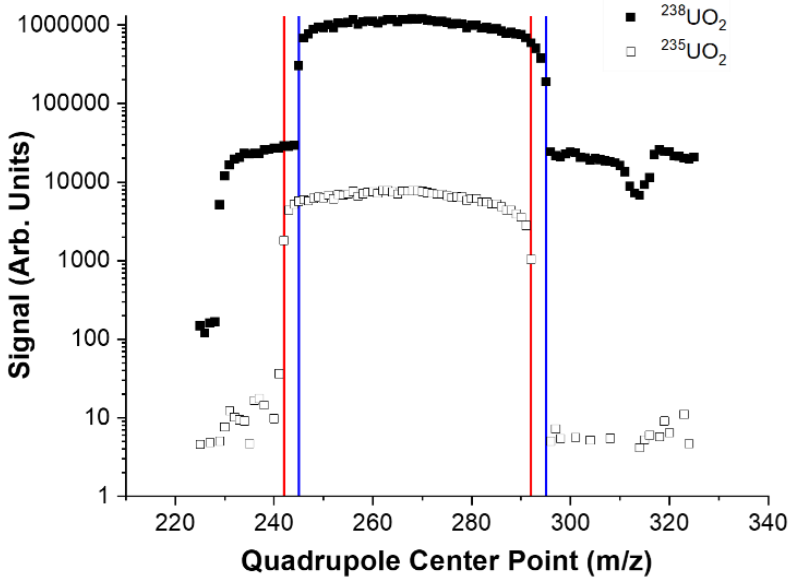

b.

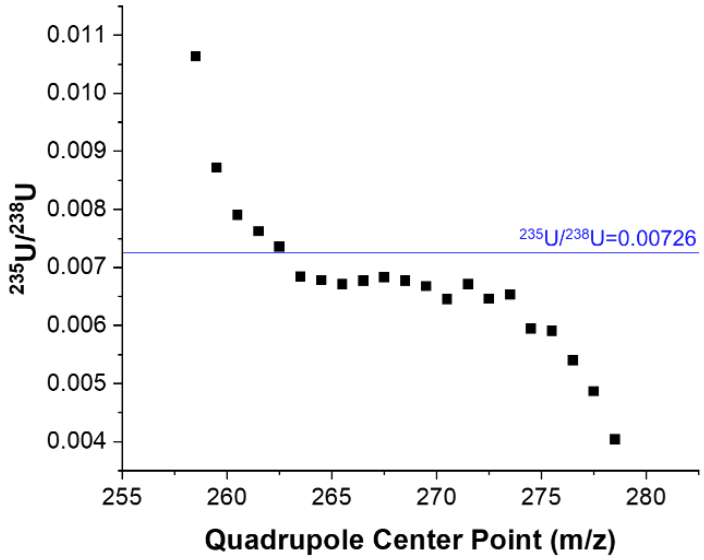

c.

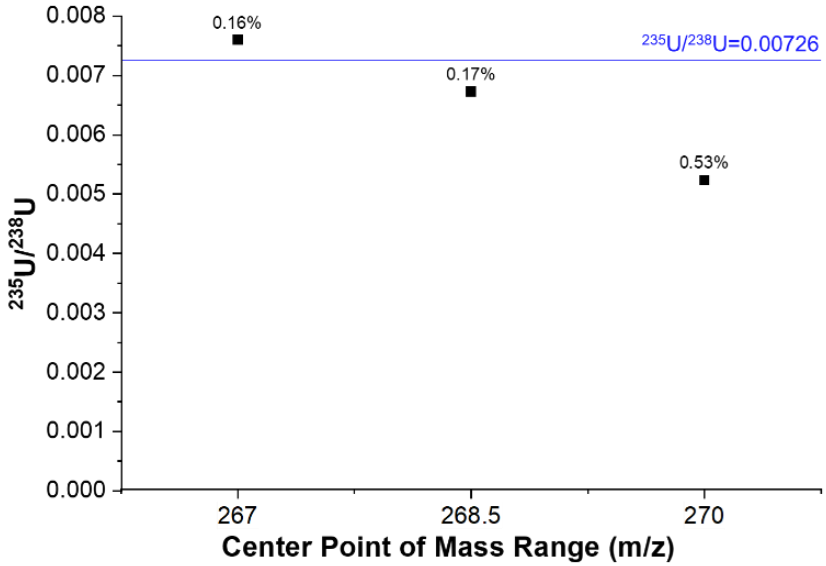

Figure 6.7: a) $^{235}UO_2$ and $^{238}UO_2$ signals as a function of slewing the center of the quadrupole range of 50 Da where the red lines represent the range in which $^{235}UO_2$ is transmitted and the blue lines represent the range in which $^{238}UO_2$ is transmitted, b) $^{235}UO_2/^{238}UO_2$ as a function of the center point with a 25 Da transmission window, and c) $^{235}UO_2/^{238}UO_2$ as a function of the quadrupole center point where 267 represents the $^{235}UO_2$ peak, 270 represents the $^{238}UO_2$ peak, and 268.5 represents the center point between the two isotopes.

As suggested previously, it is advantageous in the case of the Orbitrap system to limit the ions introduced into the C-trap to those of true analytical relevance. Thus there are advantages to using smaller-width quadrupole band passes. Figure 6.7b depicts then changes in the $^{235}U/^{238}U$ ratio as a function of the center point mass of the quadrupole transmission for the case of a 25 Da-wide window. Shown on the left-hand side of the figure, where $^{238}UO_2$ is beyond the uppermost edge of the transmission window, the $^{235}U/^{238}U$ ratio is highly biased towards the minor isotope. Conversely, when the minor isotope is at the lowermost edge of the bandpass (right-hand side of the figure), the ratio is biased in favor of the heavier isotope. Indeed, the transition regions of the band pass are easily recognized in the determined $^{235}U/^{238}U$ values. Indeed the determined values, even where both isotopes are nominally in the center of the mass window are not uniform, with the nominally-flat region being far more reduced than in the case depicted in Fig. 6.7a for the 50 Da band pass. As the pass band becomes smaller, the transition band makes up a more significant portion of the mass window, reducing transmission more severely and having a more pronounced effect on the ratio.

While 50 Da has been determined to be the optimum range for the quadrupole mass window, 10 Da is used here to emphasize potential issues stemming particularly from the quadrupole transmission characteristics. As shown in Fig. 6.7c, the $^{235}U/^{238}U$ measurement is biased towards the isotope most closely related to the center point of the quadrupole mass range. When the quadrupole range is centered on the $^{235}UO_2$ (267 Da) peak, the measurement is biased towards that isotope with a ratio of $^{235}U/^{238}U = 0.0075$. The same holds true for $^{238}UO_2$ (270 Da) where the bias is towards the higher-mass isotope resulting

in a measurement of $^{235}U/^{238}U$ = 0.005. As has already been established, Orbitrap instruments consistently report a measurement that is biased towards the $^{238}UO_2$ isotope due to the automatic (unavoidable) noise deletion step in the instrument software. The poor signal recovery for the minor isotope also manifests itself in much poorer precision due to the lower S/N characteristics. The point centered on 268.5, the halfway point between two isotopes, represents a compromise where neither isotope is apparently favored. Expected isotopic discrimination issues in quadrupole instruments are typically biased towards a particular isotope, usually the high mass one, due to issues such as a zero effect, fringe fields, or space charge effects.[53] In this case, however, the bias effects both species based on where the quadrupole band pass is centered. Clearly in this case, the highest point of transmission through this quadrupole mass filter is the mass in which it is centered. This suggests that the quadrupole field that is generated is non-uniform across the entire breadth, decreasing the efficiency of transmission at the edges of the set mass range.

6.*3.5 General Isotope Ratio Characteristics*

While isotope ratio measurements traditionally rely on ICP or TIMS based magnetic sector instruments, microplasma systems are gaining more relevance. As such, the current consideration of the much higher resolution Orbitrap is gaining in significance. Hoegg *et al*. compared the LS-APGD/Orbitrap pairing with ICP-quadrupole, ICP-scanning magnetic sector, and TIMS instruments for $^{235}U/^{238}U$ measurements, finding that the LS-APGD/Orbitrap performs much better than the quadrupole instrument, and similarly to the ICP scanning magnetic sector and TIMS instruments.[9] To that point, the quadrupole transmission characteristics depicted in Fig. 6.7 are not unrelated to the reasons that

quadrupole-based MS is seldom used in applications requiring high quality isotope ratio performance. The considerations presented in this work represent an improvement in isotope ratio measurement conditions on this Q Exactive Focus system but may also be relevant in the use of other FT or quadrupole instruments for various measurements.

To demonstrate how these considerations have improved the capabilities of this platform's isotope ratio capabilities, Table 6.2 lists isotope ratio measurements that have been previously reported by this group, and their improvements with these new capabilities and considerations, with the addition of a second lanthanide element, Sm, and the rare gas Xe.[11] The isotope ratio measurements reported previously by this group were performed on an Exactive Orbitrap instrument which, while having many of the same functions as the instrument used in the present work, lacked a quadrupole mass filter. Although both in-source CID and HCD utilities were used, the lack of quadrupole leads to concomitant ion effects, suppressing analyte signal and reducing the efficacy of the collision dissociation methods. Since the first reporting of isotope ratio measurements on the Exactive platform, optimizations including the number of scans per acquisition, the number of acquisitions per measurement, and concentration effects on low abundance isotopes have been detailed and employed. Particularly, the number of scans per acquisition has been changed from 50 scans to 100 scans per acquisitions, and only 3 acquisitions are required to make a high precision measurement.[28, 34]

Table 6.2: Comparison of isotope ratios measured in previous work, with isotope ratios measured with the considerations discussed throughout this work.

Element	*Isotope Ratio Measured*	*Expected Value*	*Previously Measured Value*	*Previous %RSD*	*New Measured Value*	*New %RSD*
Rb	$^{85}Rb/^{87}Rb$	0.413	0.4206	0.52	0.409	0.25
Pb	$^{204}Pb/^{208}Pb$	0.027	0.0236	3.31	0.026	0.26
Pb	$^{206}Pb/^{208}Pb$	0.46	0.4752	0.21	0.478	0.24
Pb	$^{207}Pb/^{208}Pb$	0.422	0.3971	0.16	0.420	0.10
Ba	$^{130}Ba/^{138}Ba$	0.001	0.0009	1.98	0.0013	0.71
Ba	$^{132}Ba/^{138}Ba$	0.001	0.0009	2.41	0.0013	0.67
Ba	$^{134}Ba/^{138}Ba$	0.034	0.0286	0.78	0.033	0.26
Ba	$^{135}Ba/^{138}Ba$	0.092	0.0855	0.559	0.091	0.18
Ba	$^{136}Ba/^{138}Ba$	0.109	0.1035	0.44	0.108	0.21
Ba	$^{137}Ba/^{138}Ba$	0.158	0.1504	0.23	0.153	0.07
UO_2	$^{235}UO_2/^{238}UO_2$	0.00726	0.00687	1.37	0.00699	0.16
SmO	$^{144}SmO/^{152}SmO$	0.115	--	--	0.098	0.13
SmO	$^{147}SmO/^{152}SmO$	0.560	--	--	0.504	0.25
SmO	$^{148}SmO/^{152}SmO$	0.420	--	--	0.388	0.25
SmO	$^{149}SmO/^{152}SmO$	0.517	--	--	0.483	0.36
SmO	$^{150}SmO/^{152}SmO$	0.276	--	--	0.261	0.08
SmO	$^{154}SmO/^{152}SmO$	0.850	--	--	0.883	0.34
Xe	$^{128}Xe/^{132}Xe$	0.071	--	--	0.049	0.37
Xe	$^{129}Xe/^{132}Xe$	0.983	--	--	0.850	0.08
Xe	$^{130}Xe/^{132}Xe$	0.152	--	--	0.129	0.20
Xe	$^{131}Xe/^{132}Xe$	0.788	--	--	0.735	0.06
Xe	$^{134}Xe/^{132}Xe$	0.388	--	--	0.443	0.39
Xe	$^{136}Xe/^{132}Xe$	0.330	--	--	0.408	0.18

From the data presented in Table 6.2, it is clear that measurement precision has significantly improved, reducing measurement uncertainties (%RSD) from as high as 3.31% in previous work, to only as high as 0.71% in every case presented. These represent improvements of as much as 13x, and most notably, this improvement is seen across fewer

measurements. The significance of this is largely relevant when considering analysis time, where 3 acquisitions as opposed to 10 results in a dramatically-reduced measurement time and consequently less sample utilized. Additionally, an improvement in accuracy also seen across each isotopic pair, representing reduction in the relative errors of up to 12x; without the use of external standards. While in all IR measurements, correction factors are applied to overcome effects from isotope discrimination and mass bias, as well as any matrix effects, the reduction in error is beneficial towards the analysis of unknown samples where greater accuracy is important. Uranium measurements in particular, have improved 1.5x in terms of accuracy, and 8.5x in terms of precision. Most importantly, these measurements consistently exceed the standards set in the IAEA ITVs for uranium measurement uncertainty. Certainly, the accuracy of this measurement, and others, are still limited by the noise deletion step employed by the instrument as discussed earlier in this work.

The two additional analytes measured in this work, Sm and Xe perform comparably to more common methods of determination. Work by Chang *et al.* measured the IR of Sm using multi-collector TIMS for atomic weight determination and found an average of 0.11 %RSD between measurements and a percent difference of 1.42% on average.[60] Compared with the LS-APGD which, on average, measured a 0.24% RSD and a percent difference for the accepted IR values of 8%, on average. The LS-APGD is comparable in measurement precision, with the %RSD of the two methods differing by only 2x. The IR accuracy is considerably poorer, largely driven by error in minor isotope measurements affected by the noise deletion step. This is consistent with comparisons of U IR measurements between these two platforms by Hoegg *et al.* for uranium determinations.[9]

Given the wider mass range of the Xe isotopes, external standardization would also be expected to improve the accuracy.

The other new analyte measured in this work, Xe, presents a particularly interesting case. In this work Xe is introduced along with the sheath gas of the LS-APGD as a gaseous analyte, deviating from the typical liquid sample. Noble gas measurements typically require specialized instrumentation, and to our knowledge, this is the first example of an atmospheric sampling ion source performing noble gas measurements. Xe IR measurements are of particular interest for applications including determining fission-product Xe isotopes in the air, or for extraterrestrial atmosphere characterization. Work by Avice *et al.* demonstrated the capabilities of a quadrupole ion trap mass spectrometer for high-precision isotope ratio measurements of Xe.[61] This instrument demonstrated an average %RSD and percent difference of 1.22% and 3.06% respectively. The LS-APGD/Orbitrap pairing, on the other hand was able to obtain a precision of 0.21% RSD, with an average error of 17.4% respectively. In this case, the measurement precision of the LS-APGD/Orbitrap pairing is considerably better (~6x), though, as seen across other analytes, the accuracy of the measurement deviates from the true value to a greater extent (~6x).[61] In general, absolute IR errors (commonly referred to as mass biases) can be remedied by use of external standards. At this point, those studies have not been performed, but the precision data suggest that any such biases are themselves stable. Again, the noise deletion step of the Q Exactive software contributes to this error, but additionally the Xe used in this work does not have certified IRs. Thus, in the absence of standards, the actual values may deviate from what would be expected. Undoubtedly, the versatility and

simplicity of the LS-APGD/Orbitrap pairing make it of interest for further investigation in noble gas analysis.

6.4 Conclusions

The work presented here demonstrates further understanding of practical considerations that must be made for isotope ratio measurements using the LS-APGD/Orbitrap system. Because the LS-APGD is prone to a variety of solvent related analyte and background species, collisional dissociation is frequently used, though its full effect on both analyte response, isotope ratio scan-to-scan precision, and atmospheric species breakdown had not been thoroughly investigated. As demonstrated, the use of collisional dissociation methods employed in this pairing can effectively break down molecular species, resulting in improved scan-to-scan isotope ratio precision. Furthermore, there are limitations to which species may be broken down into their atomic constituents based on the M-X bond dissociation energy, to which a relative cutoff for dissociation can be determined. A deep dive into the effects of the quadrupole and digitization range gives a clearer picture on how these systems interact and effect isotope ratio measurement precision. Simply slewing the center of the quadrupole range is found to bias measurements to whichever isotope is more centered in the range. Isotopes at the fringe of the mass range undergo reduced, irregular transmission, biasing the measurement. Through careful study, the quality of measurements on this system have improved in both accuracy and precision. It is believed that the process described here provides a rational approach to optimization which can implemented across diverse ion source/mass analyzer combinations. To that end, implementation of an enhanced, external data acquisition system, providing extended

transient monitoring times, ~10x greater mass resolution, absorption mode FT processing, and greater overall data processing flexibility has recently been described.[33] Ultimately, the utility of this microplasma/Orbitrap coupling continues to show promise relative multi-element, isotope ratio mass spectrometry.

6.5 Acknowledgements

Reproduced from "Roles of Collisional Dissociation Modalities on Spectral Composition and Isotope Ratio Measurement Performance of the Liquid Sampling – Atmospheric Pressure Glow Discharge / Orbitrap Mass Spectrometer Coupling," Tyler J. Williams, Edward D. Hoegg, Jacob R. Bills, and R. Kenneth Marcus, 2021, with permission from Elsevier. High Purity Standards (North Charleston, SC, USA) is gratefully acknowledged for donation of the elemental standards. This research did not receive any specific grant from funding agencies in the public, commercial, or not-for-profit sectors.

6.6 References

1. L. Yang, *Mass Spectrom. Rev.*, 2009, **28**, 990-1011.
2. S. K. Aggarwal, *Anal. Meth.*, 2016, **8**, 942-957.
3. O. T. Butler, R. Clough, J. M. Cook, E. H. Evans, A. S. Fisher, S. J. Hill, A. Taylor and M. West, *J. Anal. At. Spectrom.*, 2016, **31**, 32-34.
4. N. Jakubowski, L. Moens and F. Vanhaecke, *Spectrochim. Acta, Part B*, 1998, **53**, 1739-1763.
5. D. C. Baxter, I. Rodushkin and E. Engström, *J. Anal. At. Spectrom.*, 2012, **27**, 1355-1381.
6. S. D. Tanner, M. Paul, S. A. Beres and E. R. Denoyer, *Atom. Spectrom.*, 1995, **16**, 16-18.
7. E. Bolea-Fernandez, L. Balcaen, M. Resano and F. Vanhaecke, *J. Anal. At. Spectrom.*, 2017, **32**, 1660-1679.
8. N. Sugiyama and Y. Shikamori, *J. Anal. At. Spectrom.*, 2015, **30**, 2481-2487.
9. E. D. Hoegg, B. T. Manard, E. M. Wylie, K. J. Mathew, C. F. Ottenfeld and R. K. Marcus, *J. Am. Soc. Mass Spectr.*, 2019, **30**, 278-288.
10. A. Makishima, *Thermal Ionization Mass Spectrometry (TIMS): Silicate Digestion, Separation, and Measurement*, Wiley-VCH, 2015.
11. E. D. Hoegg, C. J. Barinaga, G. J. Hager, G. L. Hart, D. W. Koppenaal and R. K. Marcus, *J. Anal. At. Spectrom.*, 2016, **31**, 2355-2362.
12. R. K. Marcus, C. D. Quarles, C. J. Barinaga, A. J. Carado and D. W. Koppenaal, *Anal. Chem.*, 2011, **83**, 2425-2429.
13. T. J. Williams and R. K. Marcus, *J. Anal. At. Spectrom.*, 2020, **35**, 1910-1921.
14. L. X. Zhang and R. K. Marcus, *J. Anal. At. Spectrom.*, 2016, **31**, 145-151.
15. E. D. Hoegg, S. Godin, J. Szpunar, R. Lobinski, D. W. Koppenaal and R. K. Marcus, *J. Am. Soc. Mass Spectr.*, 2019, **30**, 1163-1168.
16. L. X. Zhang, B. T. Manard, B. A. Powell and R. K. Marcus, *Anal. Chem.*, 2015, **87**, 7218-7225.
17. E. D. Hoegg, B. A. Patel, William N. Napoli, D. D. Richardson and R. K. Marcus, *J. Anal. At. Spectrom.*, 2018, **33**, 2015-2020.
18. T. J. Williams, J. R. Bills and R. K. Marcus, *J. Anal. At. Spectrom.*, 2020, **35**, 2475-2478.
19. R. K. Marcus, B. T. Manard and C. D. Quarles, *J. Anal. At. Spectrom.*, 2017, **32**, 704-716.
20. E. D. Hoegg, T. J. Williams, J. R. Bills, R. K. Marcus and D. W. Koppenaal, *J. Anal. At. Spectrom.*, 2020, **35**, 1969-1978.
21. T. J. Williams and R. K. Marcus, *J. Anal. At. Spectrom.*, 2019, **34**, 1468-1477.
22. L. X. Zhang, B. T. Manard, S. K. Kappel and R. K. Marcus, *Anal. Bioanal. Chem.*, 2014, **406**, 7497-7509.
23. E. D. Hoegg, S. Godin, J. Szpunar, R. Lobinski, David W. Koppenaal and R. K. Marcus, *J. Anal. At. Spectrom.*, 2019, **34**, 1387-1395.
24. R. K. Marcus, C. Q. Burdette, B. T. Manard and L. X. Zhang, *Anal. Bioanal. Chem.*, 2013, **405**, 8171-8184.

25. A. J. Carado, C. D. Quarles, A. M. Duffin, C. J. Barinaga, R. E. Russo, R. K. Marcus, G. C. Eiden and D. W. Koppenaal, *J. Anal. At. Spectrom.*, 2012, **27**, 385-389.
26. H. W. Paing, T. J. Bryant, C. D. Quarles and R. K. Marcus, *Anal. Chem.*, 2020, **92**, 12622-12629.
27. H. W. Paing, B. T. Manard, B. W. Ticknor, J. R. Bills, K. A. Hall, D. A. Bostick, P. Cable-Dunlap and R. K. Marcus, *Anal. Chem.*, 2020, **92**, 8591-8598.
28. E. D. Hoegg, R. K. Marcus, G. J. Hager, G. L. Hart and D. W. Koppenaal, *J. Anal. At. Spectrom.*, 2018, **33**, 251-259.
29. E. D. Hoegg, R. K. Marcus, D. W. Koppenaal, J. Irvahn, G. J. Hager and G. L. Hart, *Rapid Commun. Mass Sp.*, 2017, **31**, 1534-1540.
30. J. Eiler, J. Cesar, L. Chimiak, B. Dallas, K. Grice, J. Griep-Raming, D. Juchelka, N. Kitchen, M. Lloyd, A. Makarov, R. Robins and J. Schwieters, *Int. J. Mass Spectrom.*, 2017, **422**, 126-142.
31. J. M. Eiler, B. Bergquist, I. Bourg, P. Cartigny, J. Farquhar, A. Gagnon, W. Guo, I. Halevy, A. Hofmann, T. E. Larson, N. Levin, E. A. Schauble and D. Stolper, *Chem. Geol.*, 2014, **372**, 119-143.
32. C. Neubauer, A. Crémière, X. T. Wang, N. Thiagarajan, A. L. Sessions, J. F. Adkins, N. F. Dalleska, A. V. Turchyn, J. A. Clegg, A. Moradian, M. J. Sweredoski, S. D. Garbis and J. M. Eiler, *Anal. Chem.*, 2020, **92**, 3077-3085.
33. J. R. Bills, K. O. Nagornov, A. N. Kozhinov, T. J. Williams, Y. O. Tsybin and R. K. Marcus, *J. Am. Soc. Mass Spectr.*, 2020, **Submitted for Publication**.
34. E. D. Hoegg, C. J. Barinaga, G. J. Hager, G. L. Hart, D. W. Koppenaal and R. K. Marcus, *J. Am. Soc. Mass Spectr.*, 2016, **27**, 1393-1403.
35. K. L. Busch, G. L. Glish and S. A. McLuckey, *Mass Spectrometry/Mass Spectrometry: Techniques and Applications of Tandem Mass Spectrometry*, VCH, New York, 1988.
36. S. A. McLuckey, *J. Am. Soc. Mass Spectr.*, 1992, **3**, 599-614.
37. R. E. March and J. F. J. Todd, *Practical Aspects of Ion Trap Mass Spectrometry*, CRC Press, New York, 1995.
38. D. J. Douglas, *J. Phys. Chem.*, 1982, **86**, 185-191.
39. L. Yang, S. Tong, L. Zhou, Z. Hu, Z. Mester and J. Meija, *J. Anal. At. Spectrom.*, 2018, **33**, 1849-1861.
40. E. D. Young, A. Galy and H. Nagahara, *Geochim. Cosmochim. Acta*, 2002, **66**, 1095-1104.
41. G. P. Jackson, F. L. King, D. E. Goeringer and D. C. Duckworth, *Int. J. Mass Spectrom.*, 2002, **216**, 85-93.
42. L. V. Gurvich and V. G. Ryabova, *Opt. Spektrosk+*. 1965, **18**, 143-145.
43. P. B. Armentrout and J. L. Beauchamp, *Chem. Phys.*, 1980, **50**, 21-25.
44. D. Majumdar, K. Balasubramanian and H. Nitsche, *Chem. Phys. Lett.*, 2002, **361**, 143-151.
45. A. T. Benjelloun, A. Daoudi and H. Chermette, *J. Chem. Phys.*, 2004, **121**, 7207-7221.
46. R. S. Houk, *Anal. Chem.*, 1986, **58**, 97A-105A.

47. K. J. Hart and S. A. McLuckey, *J. Am. Soc. Mass Spectr.*, 1994, **5**, 250-259.
48. F. L. King and W. W. Harrison, *Int. J. Mass Spectrom.*, 1989, **89**, 171-185.
49. D. C. Duckworth, D. E. Goeringer and S. A. McLuckey, *J. Am. Soc. Mass Spectr.*, 2000, **11**, 1072-1078.
50. J. V. Olsen, B. Macek, O. Lange, A. Makarov, S. Horning and M. Mann, *Nat. Methods*, 2007, **4**, 709-712.
51. N. C. Blias and D. G. Truhlar, *Astrophys. J.*, 1982, **258**, 79-81.
52. D. L. Bricker, T. A. Adams and D. H. Russell, *Anal. Chem.*, 1983, **55**, 2417-2418.
53. P. H. Dawson, *Quadrupole Mass Spectrometry and its Applications*, Elsevier Scientific Publishing Company, New York, 1976.
54. P. E. Miller and M. B. Denton, *J. Chem. Educ.*, 1986, **63**, 617.
55. J.-F. Hennequin and R.-L. Englebert, *Rev. Phys. Appl.*, 1979, **14**, 275.
56. S. Niewiadomski, *Filter Handbook: A Practical Design Guide*, Heinemann Professional Publishing Ltd, Jordan Hill, Oxford, 1989.
57. A. G. Marshall and F. R. Verdun, *Fourier Transforms in NMR, Optical, and Mass Spectrometry: A User's Handbook*, Elsevier Science Publishing Company, New York, 1990.
58. A. Kaufmann and M. Bromirski, *ThermoScientific White Paper*, 2018, **65147**.
59. C. E. Duchon, *J. Appl. Meteorol.*, 1979, **18**, 1016-1022.
60. T.-L. Chang, M.-T. Zhao, W.-J. Li, J. Wang and Q.-Y. Qian, *Int. J. Mass Spectrom.*, 2002, **218**, 167-172.
61. G. Avice, A. Belousov, K. A. Farley, S. M. Madzunkov, J. Simcic, D. Nikolić, M. R. Darrach and C. Sotin, *J. Anal. At. Spectrom.*, 2019, **34**, 104-117.

CHAPTER VII

SUMMARY AND FUTURE OUTLOOK

Presented here are studies across various instrument platforms expanding upon the analytical relevance of the liquid sampling – atmospheric pressure glow discharge (LS-APGD) ionization source. While mass spectrometry has typically separated itself into atomic and molecular subdivisions, use of the LS-APGD has acted to bridge the gap between the two. As discussed in Chapter I, there has been a great deal of effort towards advances in molecular mass spectrometry, manifesting in developments such as ultra-high resolution and miniaturized instrumentation. The LS-APGD offers the opportunity to exploit the advantages of molecular mass spectrometry instruments for atomic analyses, while operating with greater simplicity and reduced operating costs.

Initial efforts in Chapter II interfaced the LS-APGD with a commercial triple quadrupole platform for elemental analysis. While triple quadrupole instruments are not uncommon to inductively coupled plasma – mass spectrometry (ICP-MS) platforms, the application of specific features, namely collisional dissociation, is less common. Optimizations of the source parameters and instrument operating conditions found sensitivity on par with previous instrument couplings. Ultimately, limitations on this instrument designate its use primarily as a qualitative instrument, capable of providing information on plasma operation, or for use in tandem mass spectrometry experiments. Here it was demonstrated that, as expected, the LS-APGD creates a large number of species related to the solvent system, however, they can be effectively removed by the utilization of the collisional dissociation methods. Chapter III further utilized this platform to

investigate a single-electrode geometry of the LS-APGD, finding improved performance over the traditional design. Investigations revealed that a combination of the direct instrument coupling, as well as the alternative powering mode, had significant influence over the analytical performance. Unfortunately, the coupling to the instrument has the tendency to interfere with internal ion optics, rendering the adoption of this configuration challenging.

Chapter IV saw the LS-APGD interfaced with a reduced-format mass spectrometer, demonstrating the capabilities of combined atomic and molecular (CAM) ionization. Differences in operation between the standard ESI source and the LS-APGD necessitated optimization of the ion optics to maximize ion transmission through the instrument. This platform is not necessarily expected to have similar performance to larger, more complex instrumentation, however, the sensitivity for elemental samples is on par with previous works. Interestingly, for molecular samples investigated in this work, the LS-APGD shows sensitivity that matches or even exceeds that of the standard electrospray ionization (ESI) source. This bodes well for the LS-APGD, as it not only appears to retain benefits from the ESI source, but also gains an additional area of application in elemental analysis. The success seen in this pairing has since been carried on to applications where a transportable CAM platform is desirable, such as at-reactor process monitoring.

The operation of the LS-APGD as a molecular source was further expanded on in Chapter V with the analysis of polyaromatic hydrocarbons. These samples represented the first introduction of non-polar samples into the LS-APGD and, interestingly, both protonated molecular ions and radical cations were observed. In atmospheric pressure

chemical ionization (APCI) sources, these compounds do not protonate due to the lack of available polar sites, but rather form only radical cations. The formation of both species has been previously observed in atmospheric pressure photoionization (APPI) or other sources which operate by bombarding the sample with an ionizing material. While some preliminary investigations into the ionization mechanism of these species have been performed, more investigation is still required.

Continuing with the success of the LS-APGD for U isotope ratio (IR) measurements, Chapter VI explores the modes of collisional dissociation on the spectral composition and IR measurement. While most of these components have previously shown to improve the precision and/or accuracy of IR measurements, their particular influence or the characterization of their influence had not been thoroughly investigated. The collisional modalities are shown to fully breakdown molecular species, however polyatomic species are less efficiently dissociated. Both high bond dissociation energies and inefficient collisional processes leave a clear distinction in the limitations to species that can be dissociated. Additionally, the transmission of the quadrupole bandpass filter was investigated and was shown to have a major influence over the IR measurement. Simply based on the set mass range, some isotopes are less effectively transmitted, resulting in biases in the isotope ratio. Ultimately the considerations here have led to improvements in IR precision and accuracy compared with previous works.

As a CAM ionization source, the LS-APGD presents unique opportunities for diverse chemical analysis. The work presented here has seen new instrument couplings, electrode configurations, and applications. On each of these instrument pairings, there is

still room to improve sensitivity and investigate plasma processes, in particular additional electrode configurations have since been developed and should be implemented to these platforms. Although great strides have been made in expanding the application space of the LS-APGD and the breadth of instrument pairings, further investigations into complex samples and operating mechanisms could prove beneficial in further developing this ionization source.

APPENDICES

Appendix A

Supplementary Material for Chapter II

Optimization of In-Source CID Energy and Q2 Gas Pressure

To optimize these aspects, 50 µL injections of the 10 µg mL^{-1} multi-element solution were performed, with the resulting S/B ratio for each analyte computed and used as the test metric. Triplicate injections were performed while varying the in-source CID 0 – 200 V in 25 V increments (with no CID occurring in Q2). After optimization, the same was done for the Q2 gas, varying the pressure from 0 – 5 mTorr at 0.5 mTorr increments.

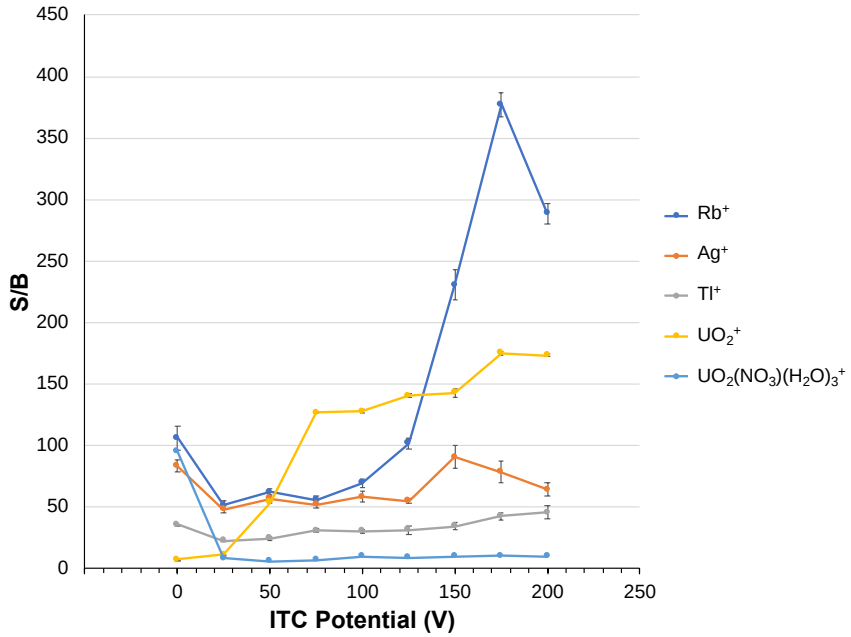

Figure A.1: Effect of ion transfer capillary potential on the S/B of the multi-element solution. Each point represents the average S/B of triplicate injections. Discharge conditions were those presented in Table 2.1. Analyte concentrations = 10 µg mL^{-1} (each), target analyte isotopes: ^{85}Rb, ^{107}Ag, ^{205}Tl, and $^{238}U^{16}O_2$.

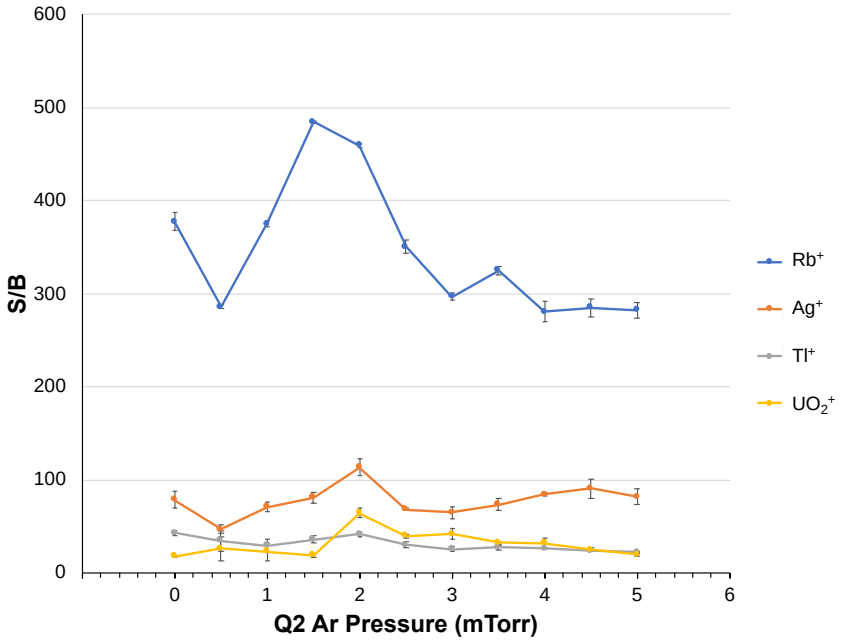

Figure A.2: Effect of the argon pressure in Q2 on the S/B ratios of the multi-element solution. Each point represents the average S/B of triplicate injections. Discharge conditions were those presented in Table 2.1. Analyte concentrations = 10 µg mL^{-1} (each), target analyte isotopes: ^{85}Rb, ^{107}Ag, ^{205}Tl, and $^{238}U^{16}O_2$.

Optimization of MS/MS Conditions

The maximum values in the chromatograms are expected to be the point in which optimum fragmentation occurs to yield the analyte species. Seen in Fig. A.3a, a maximum yield with respect to the collision energy is found at 25 V for each of the analyte species. The response reflects greater levels of efficiency with increasing voltage, followed by ion losses (scattering) due to excess kinetic energies. In Fig. A.3b, there is no clear, universal optimum in the Q2 gas pressure. Detailed interrogation across the individual spectra suggested that the greatest spectral clarity relative to the background water-related ions was obtained at a Q2 cell pressure of 1.5 mTorr Ar. Thus, a Q2 bias of 25 V and pressure of 1.5 mTorr Ar was used through the remainder of the present studies.

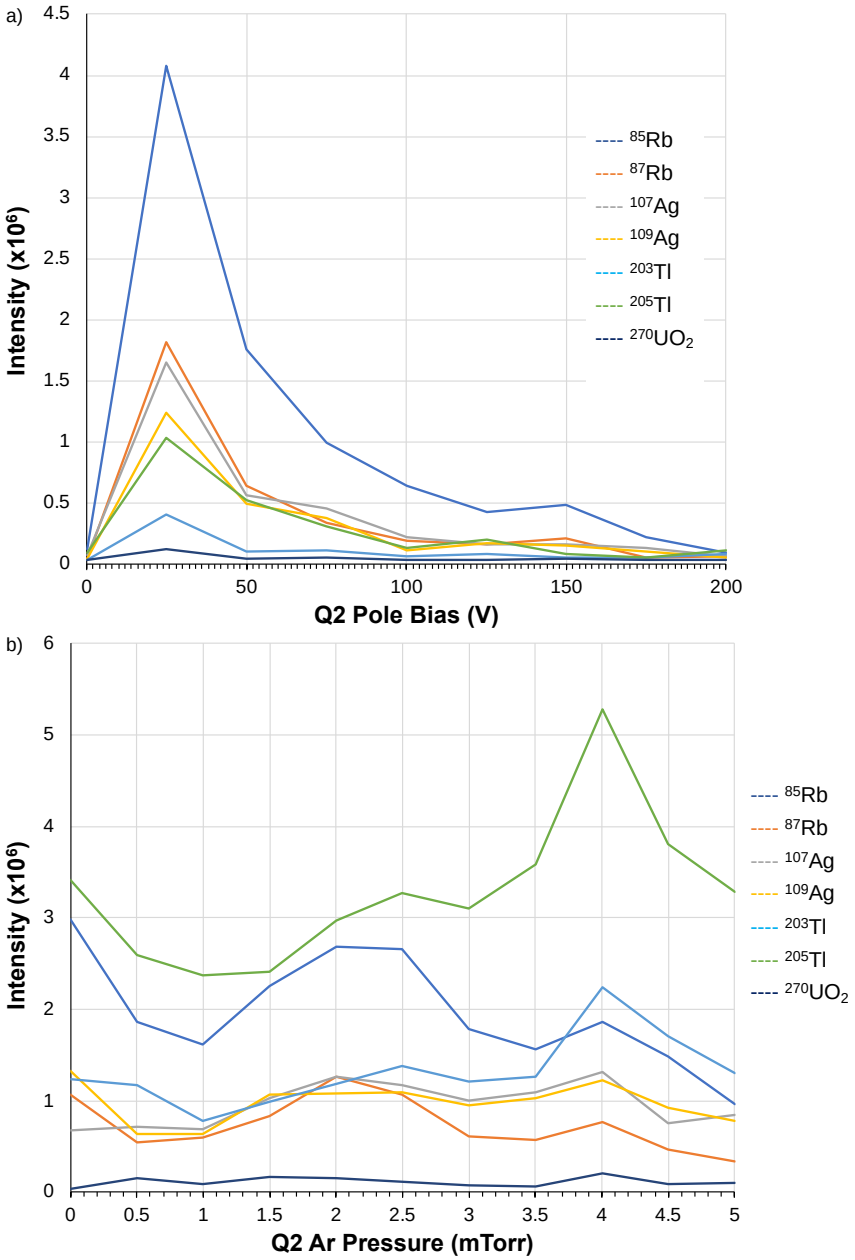

Figure A.3: Effects of the a) Q2 pole bias and b) Q2 Ar pressure on the extracted ion chromatogram of each analyte isotope for a 25 µg mL^{-1} solution containing Rb, Ag, Tl, and U. Discharge conditions were those presented in Table 2.1.

To optimize the neutral loss information content, the collisional energy was increased in 25 V increments and the total ion chromatogram (TIC) was monitored to find the point where the ion response was the most intense. The same was done for the

Q2 gas pressure, increasing in 0.5 mTorr increments, and finding the maximum in the TIC. Points past the maximum may undergo increased degrees of fragmentation resulting in species losses of greater mass (e.g., a second H_2O molecule) than the defined mass. The results of these studies are seen in Figs. A.4 and A.5, showing maximum responses at 25 V pole bias and 0.5 mTorr Ar.

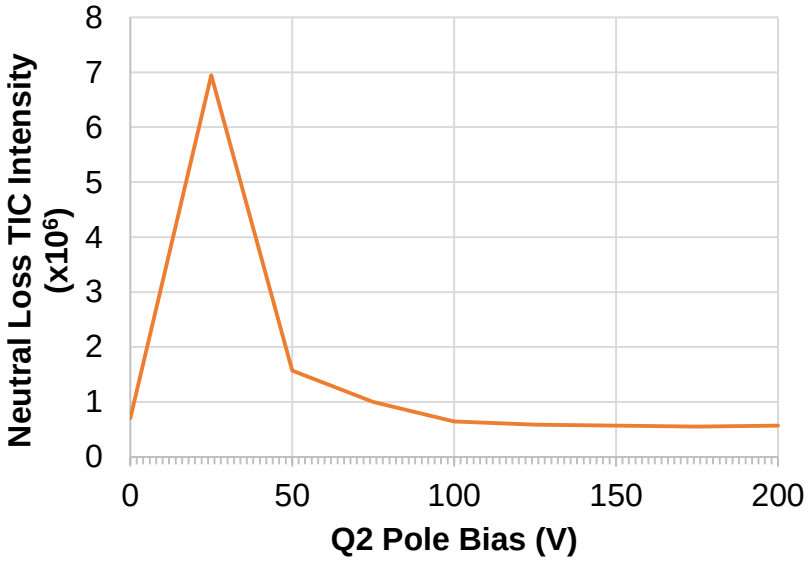

Figure A.4: Effect of Q2 collisional energy on the intensity of the total ion chromatogram for a neutral loss scan of a 25 µg mL^{-1} solution containing Rb, Ag, Tl, and U.

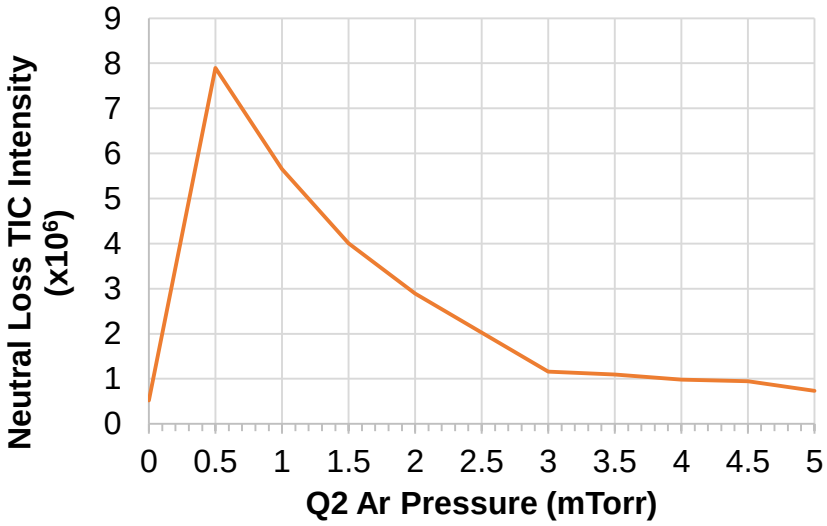

Figure A.5: Effect of Q2 gas pressure on the intensity of the total ion chromatogram for a neutral loss scan of a 25 µg mL^{-1} solution containing Rb, Ag, Tl, and U.

Appendix B

Supplementary Material for Chapter III

a.

b.

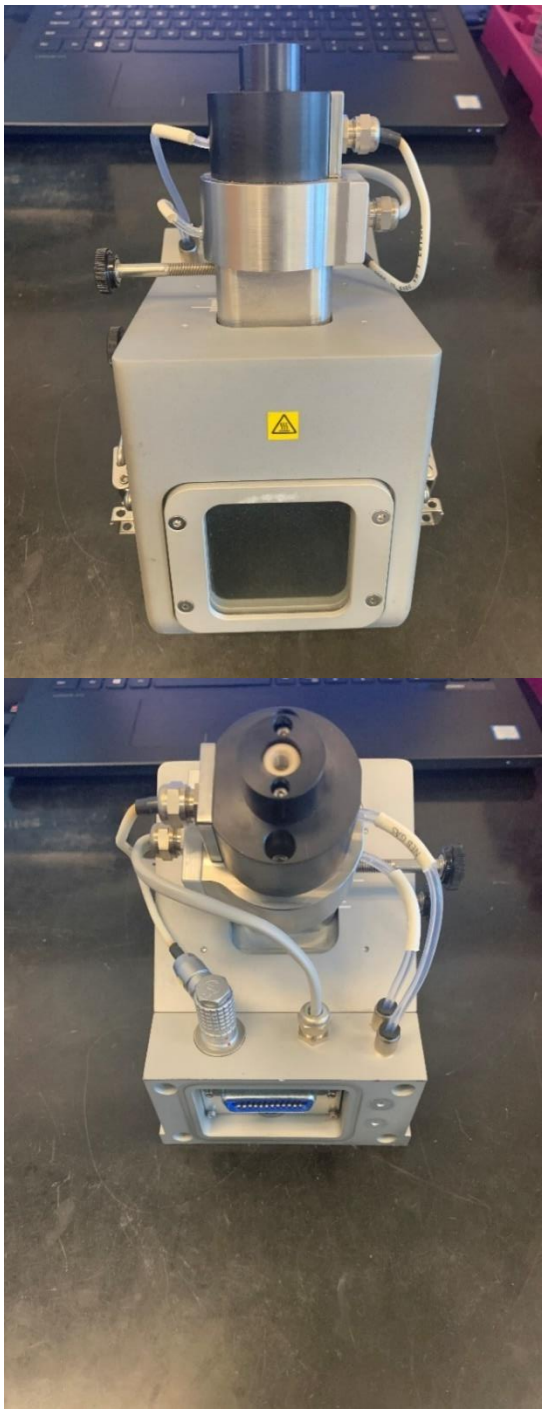

Figure B.1: a) front view and b) back view of the standard Advion ESI source

a.

b.

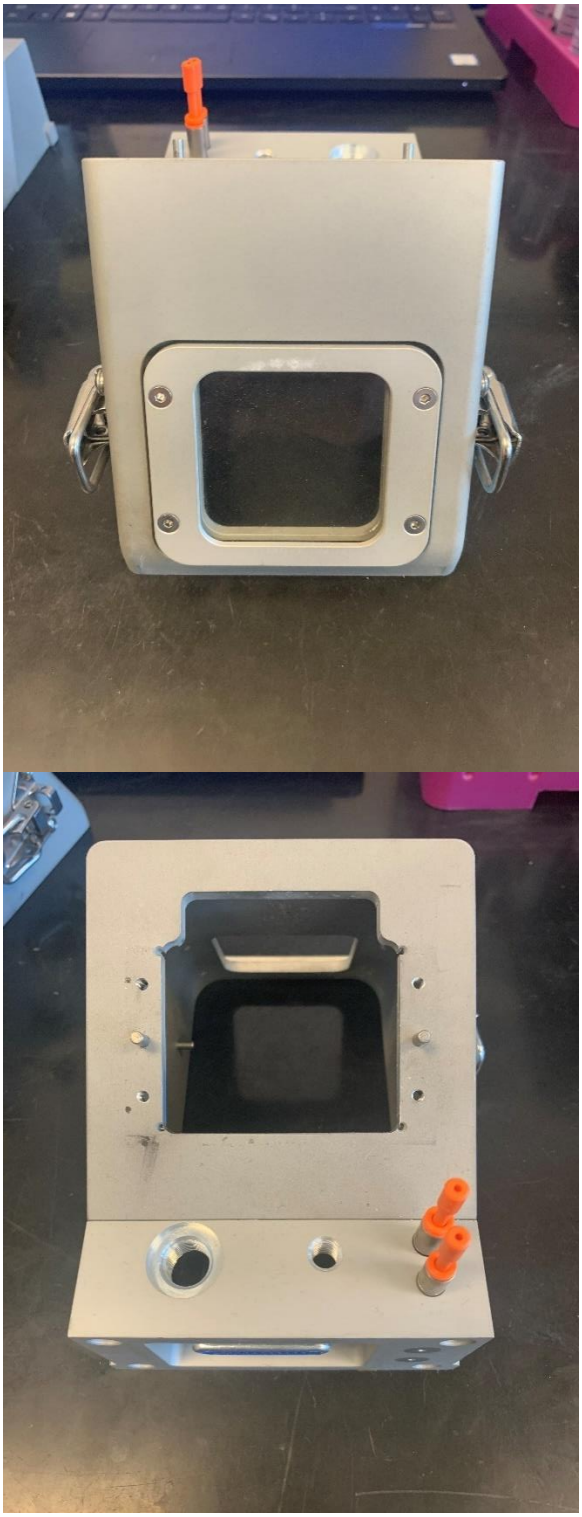

Figure B.2: a) front view and b) back view of the standard Advion ESI source with modifications made to house the LS-APGD. Simply, the hole that the ESI probe sits in has been widened.

a.

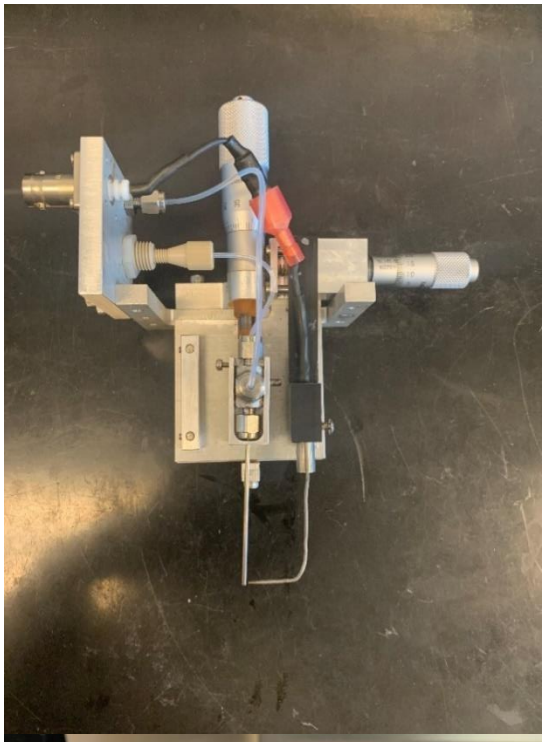

b.

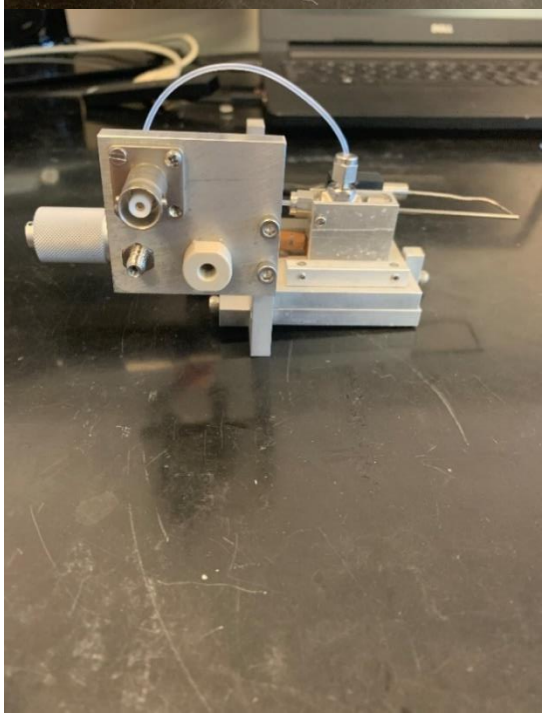

Figure B.3: a) Top down view of the LS-APGD chip designed to fit into the modified Advion ESI housing. The electrodes were placed on a moving stage with a micrometer (Thorlabs, Newton, NJ) to adjust the distance from the sampling cone. The counter electrode has an additonal micrometer to control the interelectrode displacement. b) side view of the LS-APGD chip sowing the connection for power, liquid, and gas from the control box

a.

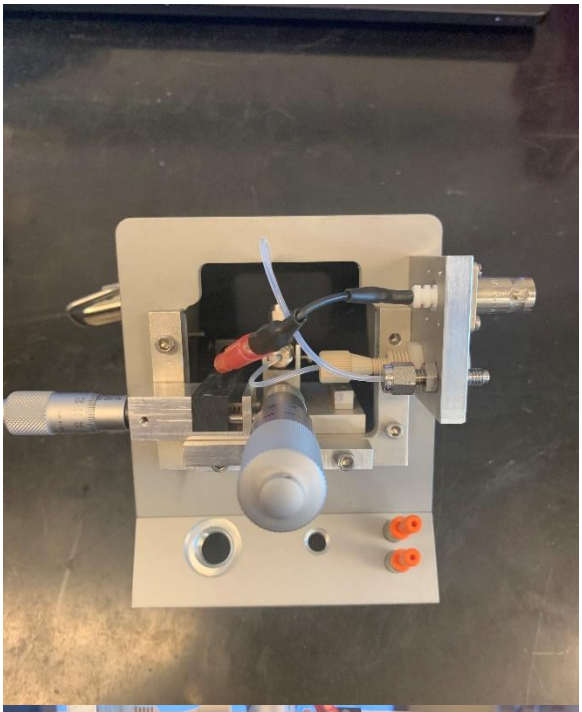

b.

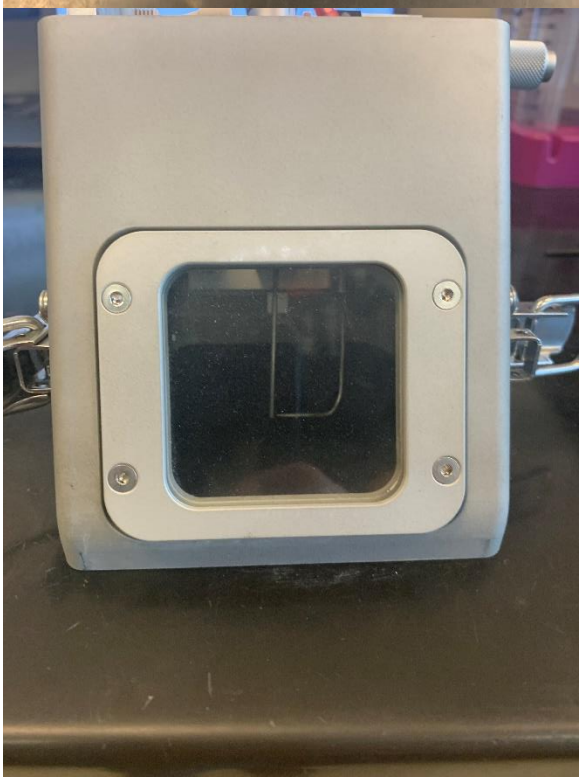

Figure B.4: a) top view of the LS-APGD fit into the modified Advion ESI housing. The chip simply slides into the housing and is held into place with a screw on either side. B) front view through the window of the source housing showing the electrodes seated in the housing

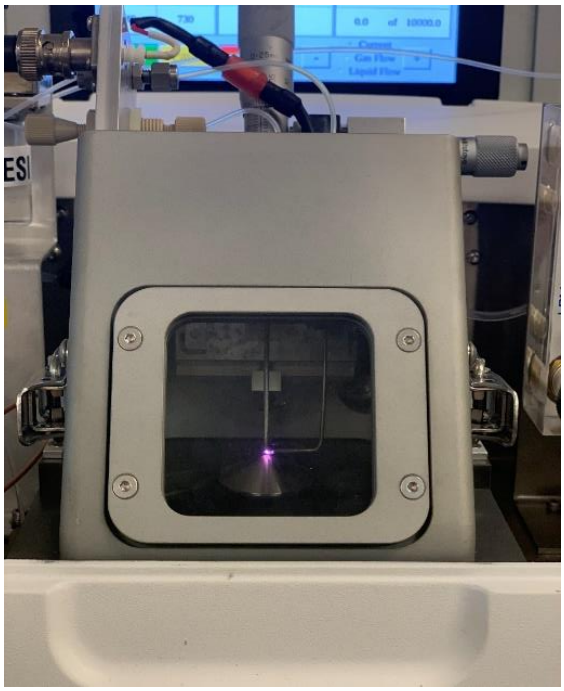

Figure B.5: Picture of the LS-APGD fit into the modified ESI housing and interfaced with then interfaced with the CMS.

Figure B.6: Control box utilized by the LS-APGD. This box controls the discharge current, gas flow, liquid flow, and the auto ignition system. All parameters are controlled through a touch screen interface.